UNIVERSITÀ DEGLI STUDI DI MILANO

DIPARTIMENTO DI FISICA

PhD SCHOOL, IN PHYSICS ASTROPHYSICS AND APPLIED PHYSICS

CYCLE XXXII

Understanding the electronic properties of quantum materials by means of photoemission with angular and spin resolution

Disciplinary Scientific Sector Fis/03

PhD Thesis of:

Chiara Bigi

Supervisor of the Thesis: Prof. Giorgio ROSSI

Co-Supervisor of the Thesis: Dr. Ivana VOBORNIK

Director of the School: Prof. Matteo PARIS

A. Y. 2019-2020

Commission of the final examination:

External Referees:
Prof. A. Damascelli, Prof. K. Sakamoto & Prof. A. Santander-Syro

External Committee Members:
Prof. G. Ghiringhelli & Prof. R. Bertacco

Internal Committee Member:
Prof. G. Rossi

Final examination:

19 December 2019

Università degli Studi di Milano, Dipartimento di Fisica, Milano, Italy

"Would you tell me, please, which way I ought
to go out from here?"
"That depends a good deal on where you want to get to."
said the Cat.
"I don't much care where-" said Alice.
"Then it doesn't much matter which way you go." said the Cat.
"-So long as I get somewhere." Alice added as an explanation.
"Oh, you're sure to do that," said the Cat
"if only you walk long enough."

Lewis Carrol - Alice in Wonderland

Cover illustration:

C. Bigi

Internal illustrations:

C. Bigi

Design:

A.D. Copia, Copiae

MIUR subjects:

FIS/03

PACS:

73.20.At, 75.25.+z, 75.70.Ak

Contents

Abstract

This thesis contains a selection of the results on the shallow electron states of quantum materials that I obtained as doctoral student of the Scuola di Dottorato in Fisica, Astrofisica e Fisica Applicata at the Università degli Studi di Milano. I carried out my doctoral research activity mostly at the TASC-IOM CNR laboratory, in the framework of the NFFA and APE-beamline facilities (Elettra Sincrotrone Trieste), as well in dedicated sessions at the I09 beamline of the Diamond light source, Harwell Campus, UK. To access the electronic properties of materials I specialised myself in photoemission spectroscopy techniques. High quality samples are a prerequisite for any attempt to study quantum materials so that a major effort in my PhD project has been to master the growth of novel quantum materials by means of Pulsed Laser Deposition (PLD). Given that the PLD is integrated in the suite of UHV facilities attached in-situ to the APE beamline, I directly characterised the electronic properties of the PLD grown samples exploiting both the spectroscopic techniques available at the beamline (ARPES, X-ray photoemission and absorption spectroscopies: XPS and XAS), either ex-situ structural characterisation tools (X-ray diffraction –XRD– and X-ray reflectivity, XRR).

Photoemission spectroscopy is a powerful and versatile experimental tool for understanding the electronic properties of materials, providing deep insight into various physical and chemical phenomena, ranging from

electronic correlations to surface reactions. Angle-resolved photoemission spectroscopy (ARPES) provides direct insight in the dispersion of extended valence electronic states. Its combination with spin selective detection (spin-ARPES) gives access to the spin polarisation of the photoelectrons at specific points in the Brillouin zone, i.e. to the spin texture of the corresponding band structure. The photoemission intensity is modulated by the "matrix element effects", which express the probability of photoelectron transition from the initial to the final state and link the specific experimental geometry to the symmetry properties of the electron states. This implies that a change in the light polarisation or incident/emission angle induce variations in the spectral intensity and can be misleading in the interpretation of ARPES and spin-ARPES results. In this scenario, a fruitful approach is the simultaneous detection of all quantum numbers of the final state photoelectrons together with the exploitation of light polarisation and photoionisation cross-section tuning. I directly addressed the matrix-element effects performing measurements on the spin polarised states of $NbSe_2$ single crystals while varying the photon energy and polarisation at the highly efficient apparatus for vectorial spin-polarization analysis available at APE-LE beamline.

The second part of my thesis work was dedicated to the investigation of the electronic properties of two oxide systems $SrNbO_3$ and anatase TiO_2, whose peculiar properties are exploited in catalysis. While TiO_2 is a very well-known catalytic material, SrNbO3 has only recently been proposed for applications due to visible- light photo-catalytic properties driven by plasmonic resonances. Up to now, systematic experimental investigation of such a system with X-ray/UV electron spectroscopies was missing. X-ray absorption and photoemission spectroscopies were used to probe the chemical states of the samples and the changes induced by different oxygen pressure during the growth. I further performed detailed ARPES investigation of the electronic band structure of $SrNbO_3$. I found that the Fermi surface is made up by three bands mainly originating from t_{2g} orbitals of Nb 4d, as reported for 3d based perovskite systems. The experimental results are consistent with the band dispersion predicted by bulk Density Functional Theory (DFT) calculations that I performed by means of the open source QuantumEspresso software. The narrower bandwidth observed in the ARPES spectra with respect to calculations suggests mass renormalisation arising from electronic correlations.

Anatase TiO_2 is utilised in a number of applications ranging from photocatalytic devices to sensors as well as solar cells. To efficiently tailor

high performing devices, the understanding and control of carrier concentration in the material is a key aspect. I therefore investigate the role of oxygen vacancy defects at the (001) anatase surface that are known to induce extended metallic states on the surface of this nominally insulating material, by means of ARPES and Resonant-ARPES. I observed both localised and metallic delocalised electronic states and investigated the evolution of the spectral intensity as a function of varying oxygen vacancies. I found that the excess oxygen, provided by O_2 dosing at the surface, significantly quenches the localised states, whereas O_2 reaction has weak impact on the delocalised electronic states: the number of free carriers is reduced but could not be suppressed. These results are very promising for future applications as they may be exploited to tune the excess carriers' concentration in novel anatase-based devices.

Introduction

To see a World in a Grain of Sand [...]

William Blake - Auguries of Innocence

Electrons in solids

Each solid is formed by many atoms, of order $10^{23}\,\mathrm{cm}^{-3}$, and interatomic distances, likewise in molecules, range from 0.2 nm to 0.4 nm. Under these circumstances, one has to tackle a many-body problem to understand the behaviour of the bound electrons, as they are affected by each other and from the hosting ionic lattice as well. Drastic approximations are customarily done to classify the (huge) number of electrons contained in any piece of condensed matter in two main subgroups: the *valence electrons* and *core electrons*. The latter electrons are strongly bound to the nuclei (E_B>30 eV), occupying the inner orbital shells. The wavefunctions of those electrons are extremely localised near the nuclei, partially screening the positive nuclear charges. Consequently, the core electrons

display negligible energy dispersion and resemble the atomic-like wavefunctions with renormalised energies with respect to free atoms. Hence, in first approximation core electrons can be considered only slightly affected by the surrounding environment (e.g. by crystal field splitting or by the symmetries of the lattice), whilst they are a very sensitive probe of the chemical properties (e.g. atomic species and oxidation states) of matter. The valence electrons instead actively participate in the chemical bonds, as the more extended electron wavefunctions of the atoms hybridise each other and split into bands representing electron states ranging from the extreme bonding and anti-bonding limits. The crystal symmetry determines the boundary conditions for the electron wavefunctions and the resulting bands reflect all the symmetries of the crystal as well. As a result, even tiny variations in the local environment can strongly affect the valence band structure.

The electrons are not independent from each other and from the solid which hosts them, but their behaviour is the result of a thick net of many-body interactions. In such a many-body framework

A rigorous theoretical description of the valence electron is rather complex as electrons interact with each others, with the lattice and possibly electric/magnetic fields. The outcome electronic bandstructure is therefore determined by the solutions for this many-body problem, and advanced discussions of the topic are given in several solid state physics text books. [1–3] A much simpler picture is provided by the combination of the Bloch's theorem [4] and the Muffin-tin approximation [5]. The nuclei and the localised core electrons form positively charged ions that act as attractive quantum wells for the valence electrons. The overall crystal field (V_i) arises from the sum of all the ionic potentials and follows the crystal lattice periodicity. Its shape is approximated to a muffin tin (panel a of Figure 1), where each ion site occupies . The wavefunction of the (delocalised) valence electrons $\psi(r)$ must fulfil the Shrödinger equation:

$$\left[-\frac{\hbar^2}{2m}\nabla^2 + V_i\right]\psi_n(r) = E_n\psi_n(r) \tag{1}$$

where m is the effective electronic mass and V_i is the potential associated to the crystal field presented above. The n index explicitly links the eigenfunction $\psi_n(r)$ to the specific eigenvalue E_n. A general expression for the eigenfunction of Equation 1 is given by a linear superposition of Bloch's wavefunctions $\psi_n(r) = \sum_{\mathbf{k}} e^{i\mathbf{kr}} u_{\mathbf{k}}(\mathbf{r}+\mathbf{R})$, being $\mathbf{R}$ the periodicity of the crystal and $\mathbf{k}$ is the crystal wavevector associated to E_n. The result-

ing set of electronic eigenvalues determines a energy spectrum interrupted by ranges of forbidden energies (the *band gaps*) that is called the band structure. The Fermi level E_F separate the occupied bands from the non-occupied electronic states. In the material's ground state the electrons fill the band structure up to E_F and the whole set of wavevectors intersecting the Fermi level at $\mathbf{k}_F$ identifies the Fermi surface. The Fermi surface (i.e. the isoenergetic surface of the most energetic bound electrons in the ground state) contains all the symmetry elements of the solid and of its surface. As electronic excitations necessarily involves transitions towards the non-occupied band structure, the Fermi surface is closely related to the low energy-excitation of the materials. The spectrum of low energy excitations is therefore highly characteristic of a solid and of a given solid surface and provide deep insights in the low-temperature phase diagrams of the macroscopic systems.

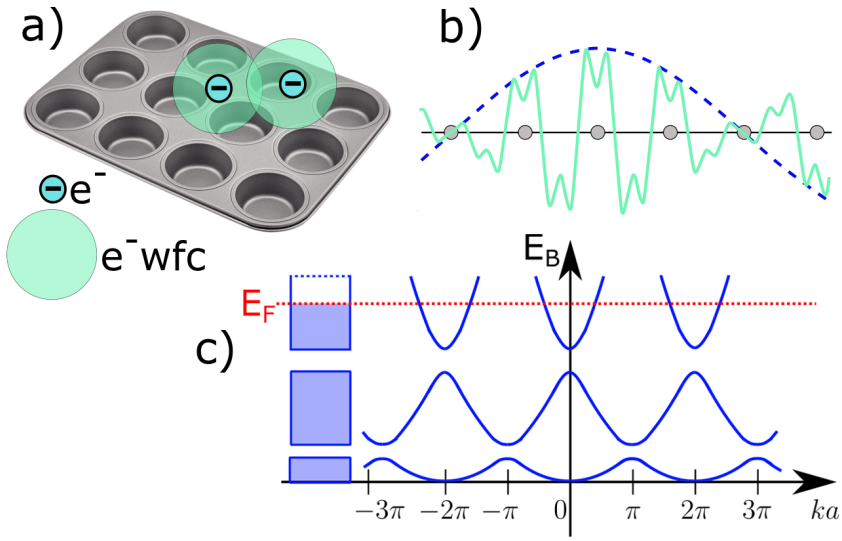

Figure 1: (a) The periodic arrangement of the ions originates a periodical potential characterised by a muffin-tin look. The valence electrons are delocalised over the whole sample experiencing the periodical potential of the lattice. Their wavefunction can be represented through a plane wave modulated by the lattice symmetries, i.e. the (b) Bloch's wavefuntion. (c) The set of energy eigenvalues associated to the valence wavefunctions originates the band structure ($E(\mathbf{k})$) of the solid. For the ground state configuration the bandstructure is filled up to the Fermi level.

Spectroscopy experiments with surface sensitivity are direct way to access the Fermi surface. Techniques such as electron scattering and direct or inverse photoelectron spectroscopy allow to explore the inter-band/intra-band transitions extending to very highly energetic empty band states, in other words to investigate the electronic states of the solid.

Photoemission spectroscopies (PES) are very powerful experimental techniques to investigate the electronic properties of matter. Exploiting the photoelectric effect, PES probes the properties of bounds electrons and carries information about the interactions within the correlated many-body electron system. XPS core electron spectroscopy is in first approximation used to estimate the presence and abundance of an atomic specie in the solid. The element-specific binding energy also represents the local electrostatic field at the atom site, which reflects the kind, the number and the spatial arrangement of the ligand neighbours. For example, chemical shifts and surface shifts can be deduced and analysed. On top of that, the low-energy interband transitions across the Fermi level enters the XPS core level spectra as energy loss spectrum lineshapes. High resolution electron spectroscopies directly explore also the low energy excitations across the Fermi surface and determine the shape and size of the Fermi surface itself. This is achieved through the proper choice of experimental conditions and the exploitation of highly performing detector apparatuses. The accurate determination of the full set of quantum numbers of the final photoelectron state (momentum k, energy E and spin polarisation P) is mastered by the so called spin-ARPES or all-resolved PES. However, the understanding of the measured intensities is a complex problem as these are determined by the materials properties (what is usually called the "initial states" e.g. the electron bands in the ground state of the material) and by the particular conditions of the specific experiment. These effects can hinder the interpretation of the photoemission spectra and must be carefully handled.

To successfully perform a PES experiment severe prerequisites must be fulfilled. Firstly, a suitable light source providing monochromatic radiation is mandatory to investigate the electronic band structure with adequate energy resolution and reasonable statistics. Moreover, Ultra-High-Vacuum (UHV) environment (i.e. background pressure below 10^{-9} mbar) must be provided in the experimental chamber. Several reasons make UHV an essential condition: it prevents the light beam to be scattered, it avoids the loss of photoemitted electrons through interaction with air particulate and it hinders the sample's degradation caused by external contaminations

adsorption. Finally, the sample preparation and survey represent crucial and integral part of the experiment, particularly stringent for ARPES and Spin-ARPES experiments. Two approaches are possible. The most common consists in the cleaning of sample's surface (e.g. with sputtering and annealing processes or cleaving methods). The second strategy involves the sample is directly fabricated *in-situ* and transferred to the experimental chamber avoiding air exposure.

All these requirements are fully satisfied by the NFFA and APE-beamline facilities, where this thesis work has been mostly carried out. [6] Synchrotron radiation in the ultraviolet and soft X-ray range and fully tunable polarisation is provided by two independent Apple-II insertion devices. The end-stations of the two branches are directly connected each other throughout a multicomponent UHV transfer system. Chambers specifically devoted to the *in-situ* growth as well as surface preparation and characterization of the samples are attached to the same UHV manifold. Overall the NFFA laboratory enables both to grow thin epitaxial films and to clean single crystals, whose electronic properties can be directly assessed *in-situ* by means of advanced spectroscopic techniques immediately after the sample preparation.

1. Photoemission

> We break the surface tension
> with our wild kinetic dreams
> Curves and lines – of grand
> designs
>
> Rush - Grand Designs (1985)

1.1. The photoemission process

Photoemission spectroscopies are powerful tools to investigate the bound electrons in a solid state system. [7] The term defines the class of "photon-in electron-out" techniques exploiting the photoelectric effect.[8, 9] books [7, 10] and reviews. [11–13] The main features are sketched in Figure 1.1. A photon characterised by energy $h\nu$ and possibly in a defined polarisation state impinges on the surface of the sample with a particular angle α. For suitable energies the photon is able to extract a bound electron from the solid to vacuum and the sample is left in an ionized (excited) state. The emitted electrons are called *photoelectrons* and are said to be *photoemitted* from the material with kinetic energy E_k an angular distribution (Θ,φ)

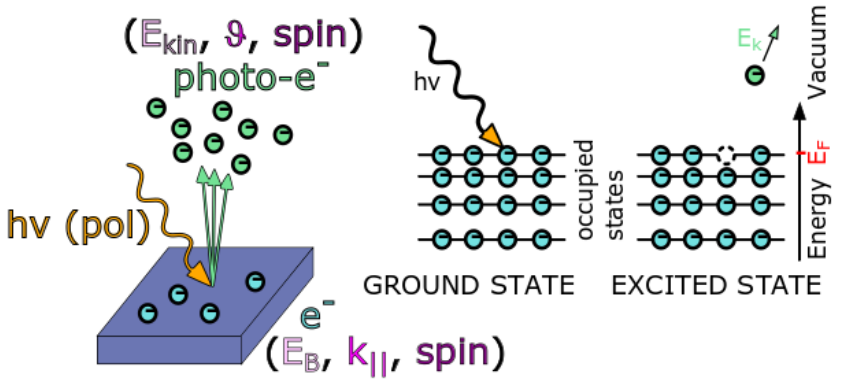

Figure 1.1: Scheme of the photoemission process leaving the sample in an ionized state. The capability to resolve the whole set of quantum numbers and to successfully relate them to the initial state gives access to the electronic properties of materials

and spin. Finally, the photoelectrons ejected in the solid angle aperture determined by the analyser geometry are collected and filtered. The full description of the photoelectron's final state is achieved by measuring the whole set of its quantum numbers (i.e. kinetic energy, emission angle and spin). Depending on the type of the analysis performed on the photocurrent, three spectroscopic techniques can be identify:

- data acquired filtering just the kinetic energy of the final state (i.e. integrating both the angular dependence and spin) are commonly defined photoelectron spectroscopy (PES)
- energy and momentum resolved spectra are named angularly resolved photo-electron spectroscopy (ARPES)
- full resolved photocurrent is achieved when spin polarisation analysis is combined with ARPES to get Spin Polarised ARPES (Spin-ARPES). The capability of spin-ARPES experiments to probe the average spin polarisation of the initial state is ensured by the $\Delta S=0$ dipole selection rule.

A photoelectron does not travel freely throughout the solid, but may be inelastically scattered by interaction with other electrons or atoms as well as with electric/magnetic fields. The average distance a photoelectron covers without being scattered is named inelastic mean free path (λ_{IMPF})

and it is a function of the photoelectron kinetic energy E_k.[7, 14] For the present work typical value of E_k are ~5-10 Å. As a result, photoemission spectroscopy is inherently a surface sensitive technique as the probing depth is spatially limited to this narrow region. Consequently, all the surface's contaminations (e.g. C, CO, O) must be carefully prevented to measure the pristine band structure of clean, freshly prepared surfaces. This is pragmatically achieved performing the experiments in Ultra High Vacuum (UHV) controlled ambient.

The interpretation and analysis of the spectra rely on the level of detail provided by the theoretical model. The so-called one-step model is the most rigorous one. It treats the photoemission process as a whole and demand the full calculation of the involved in the electron transition from the bound initial state to the detection.[13, 15–17] The three-step model is a much simpler phenomenological approach which will be described in the next paragraph.

1.1.1. The three step model

The three step model is the simplest and very intuitive picture to describe the photoemission process.[7, 12, 18] It consists in three independent steps also reported in *panel a* of Figure 1.2

- The bound electron identified by the binding energy (E_B), momentum ($\mathbf{k}_i$) and spin state S absorbs a photon of energy $h\nu$. For suitable energies, the photon excites a bound electron into a Bloch bulk state of the solid. In this scenario the energy is strictly conserved, while the three dimensional momentum vector is conserved within multiple reciprocal lattice vector $\mathbf{G}$ provided that the photon momentum is negligible. Spin is conserved in the excitation process thanks to the $\Delta S = 0$ dipole selection rule.

- The excited electron propagates in the crystal towards the surface. Given the short λ_{IMFP}, the travelling electron possibly undergoes several inelastic scattering processes. These photoelectrons lost the information about their initial state and simply contribute to the spectral background. The multiple scattering processes also produce secondary electrons which contribute to the final intensity of the spectra too.

- Photoelectron with suitable kinetic energy is transmitted through the surface potential barrier (Φ) into a final free vacuum state with

kinetic energy (E_k), final momentum ($\mathbf{k}_f$) and spin polarisation (S).

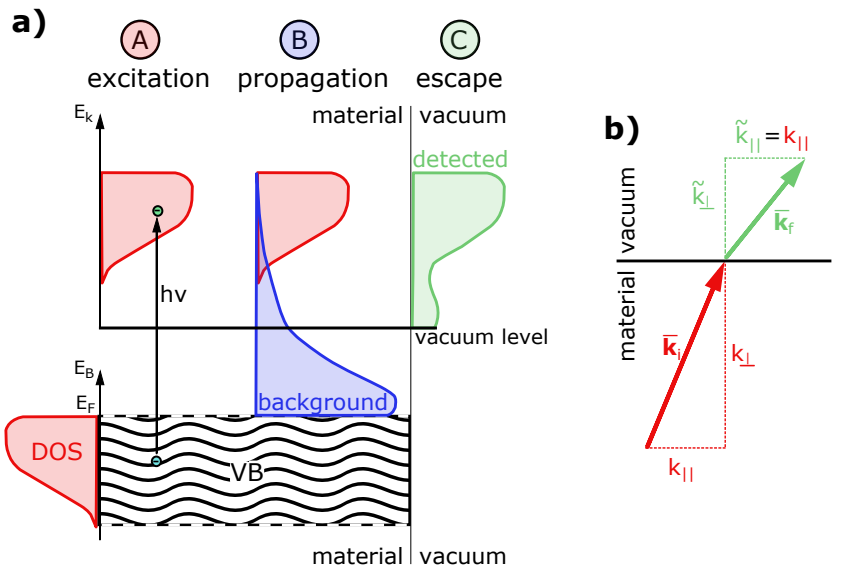

Figure 1.2: a) Cartoon representing the three steps model. b) Photoelectron momentum in the material (red) and momentum of the photoelectron travelling in vacuum (green) after surface refraction.

The binding energy E_B of the initial bound electron state can be unequivocally related to the kinetic energy E_k of the detcted photoelectron thanks to the energy conservation law[9, 13]: $E_k = h\nu - |E_B| - \Phi$. Φ is the surface potential barrier that prevents the bound electrons to be freely released in vacuum by the solid.[9] It is also called work-function and is characteristic of the material's surface (of the order ~5 eV).

To retrieve the initial electron momentum $\mathbf{k}_i$ is not straightforward and it should be treated carefully.[7, 12, 19] As mentioned above, the infinitesimal spatial translation symmetry is broken according to lattice periodicity and the momentum is conserved within multiple of the reciprocal lattice vector. However, this scenario holds just inside the solid. The spatial lattice symmetry is broken as the photoelectron cross the interface between the material and the vacuum. As a result, only the projections parallel to the surface plane of the final momentum ($k_{||,f}$) are strictly conserved and can be related to the respective initial state momenta $k_{||,i}$ by the

equations:

$$k_{||,\mathrm{i}} = k_{||,\mathrm{vac}} = \frac{\sqrt{2m_e E_{kin}}}{\hbar}\sin\theta \simeq 0.5\sqrt{E_{kin}[eV]}\sin\theta\frac{1}{\text{Å}} \tag{1.1}$$

where Θis the emission angle (measured from the surface normal) of the photoelectron in vacuum with kinetic energy E_{kin}. On the other hand, the momentum component perpendicular to the sample's surface ($k_\perp$) is not conserved due to the symmetry breaking imposed by the interface of the crystalline material with the vacuum. However, it may be retrieved with some assumptions. The surface potential lowers the E_{kin} of the photoelectron. Due to the conservation laws, only the $k_\perp$ component is affected and the ejected electron is refracted at the surface as depicted in *panel b* of Figure 1.2. [11]

$$k_{\perp \mathrm{i}} = \frac{\sqrt{2m_e E_{kin}\cos\theta^2 + V_0}}{\hbar} \tag{1.2}$$

V_o is celled the inner potential and it is a material dependent constant value (commonly in the range from 10 eV to 18 eV).[7, 13] Finally, the photon momentum may be disregarded in conventional ARPES (i.e. for photon energies hν< 120 eV). Otherwise, it must be explicitly included in the equations considering the photon transferred momentum. [12] Although this simple picture allows to efficiently describe the photoemission data, the assumption of dividing the single process into three independent steps is quite rough and miss a lot of information. Only the photoelectron is considered, while the remaining N-1 excited system is generally neglected as this model discards the de-excitation channels of the ionised sample. On the other hand, the sample is a many-body system that is involved as a whole in the photoemission process. All the variations in the photoemission spectra arising either from the system's relaxations or many body effects are not caught by this simple model. Therefore, a more rigorous one-step model, treating the process as a whole, has to be considered.

1.1.2. Many-body interactions, the sudden approximation and the A(k,ω)

The one-step framework not only describes the removal of one electron from a bound state, but also includes all the possible de-excitation processes of the remaining N-1 electrons in the ionised solid. [10] The process can be regarded as the transition between an initial many-body state (identified by the wavefunction $\Psi^{\mathrm{N}}_{\mathrm{i}}$) to the final state described by the

N-electrons wavefunction $\Psi^{N}{}_{f}$. According to the Fermi's Golden Rule, the photoemitted intensity is thus proportional to the probability amplitude of the initial many-body state to be scattered into the upon the interaction with the interacting Hamiltonian H_{int}:

$$P_{f-i} = |\langle \Psi_f^N | H_{int} | \Psi_i^N \rangle|^2 f(\epsilon)\delta(E_f - E_i - h\nu) = |M_{f-i}|^2 f(\epsilon)\delta(E_f - E_i - h\nu) \tag{1.3}$$

The Fermi-Dirac distribution f(ε) has been included to explicitly express photoemission probes only the occupied states. The Dirac delta distribution δ(E_f - E_i - hν) account for the energy conservation law and states that the scattering between the initial and final state is allowed provided that the photon energy matches the energy difference between the two states. The interaction matrix element $M_{f\text{-}i}$ in Equation 1.3 bears all the details of the many-body nature of the system and all the possible responses of the latter to the photo-excitation. For simplicity, the sudden approximation is introduced in the model.[12, 13, 19] It assumes that the time required by the photoelectron to escape the solid is significantly shorter than the recovery transient necessary to the ionised system to relax. If this request is fulfilled the consider N-body system can be regarded as composed by two non-interacting parts. The single photoelectron and escaping the sample after photon absorption and the left (N−1)-body system, being N the total number of electrons in the initial ground state of the solid. This is mathematically expressed with the factorisation of the wavefunctions involved in the matrix element M_{f-i} of Equation 1.3 which becomes:

$$|M_{f-i}|^2 \propto \left|\langle \phi_f | H_{int} | \phi_i \rangle \langle \Psi_f^{N-1} | \Psi_i^{N-1} \rangle\right|^2 \tag{1.4}$$

The explicit definition of the interaction matrix element of Equation 1.4 states that the transition probability do not uniquely relies on the wavefunction of the single electron excited into the vacuum, but it also contains information on the other N-1 electrons and their interaction with the photoexcited electron. The photoelectron is no more sufficiently described as a single free particle, but the so called quasiparticle must be considered instead. The quasiparticle is *dressed* by all the possible interactions between itself and the surrounding system (i.e. both electrons and ions). In particular, the N-1 body cross-product states the probability that the hole creation in the i-th level will result in the specific excited f-th final state. [13] When the interactions of the system are discarded, the cross-product reduces to a delta function peaked on the initial state and the three step model is recovered. Conversely, the one-particle Green's function formalism G(**k**,E) is usually introduced to describe the photoemission process.

[20, 21] In this framework, the cross product of Equation 1.4 is expressed by means of the so called *spectral function*, A(**k**,E). It is a functional defined from the imaginary part of the Green's function and describes the probability to add/remove an electron from the ground state of a many body electronic system. It thus comprises all the possible responses of the many-body system to the excitation. [10, 13, 19] A explicit expression for the spectral function is given by Equation 1.5 and it can be achieved by introducing the self energy $\Sigma = \mathrm{Re}(\Sigma) + i\mathrm{Im}(\Sigma)$, which represents the energy of the interacting electron system as a whole. In particular, the real part accounts for the system's energy renormalisation in respect to the energy of the non-interacting system (E_o) and the imaginary part quantifies the lifetime of the quasiparticle.

$$A(\mathbf{k}, E) = \frac{1}{\pi} \frac{Im(\Sigma)}{(E - E_0 - Re(\Sigma))^2 + Im(\Sigma)^2} \tag{1.5}$$

The spectral function of Equation 1.5 can be computed through *ab initio* calculations based on the Green's function formalism (e.g. GW or GW_o). However, the measured ARPES signal contains even more information than A(**k**,E). As expressed in Equation 1.4, the spectral function signal is weighted by the one-electron $\langle \phi_f | H_{int} | \phi_i \rangle$ term. It is strongly affected by extrinsic factors through the perturbative Hamiltonian, namely the experimental geometry, the photon energy and the light polarisation as well. Besides, it reflects the symmetries of both the initial and final state electronic distributions too. The overall modulation of the photoemitted intensity experimentally detected is generally known as *matrix element effects*. [12, 13, 22, 23] A detailed and quantitative interpretation of the matrix element is not straightforward. Nevertheless, simpler qualitative prediction can be done in the dipole approximation by considering the light polarisation and the orbital symmetries of the sample. A final state phtoemitted by the (0,0) BZ must have even spatial distribution to be detected with a finite probability. Hence, the vector $H_{int} |\phi_i\rangle = \mathbf{A} \cdot \mathbf{p} |\phi_i\rangle$ must be even too otherwise the scalar product is zero and no photoemitted intensity would be detected. Hence, linearly polarised light may be exploited to probe the symmetry of the occupied states. Figure 1.3 reports as an example the d_{xy} orbital. Two orthogonal mirror planes can be identified: xy and yz. Both the light polarisation vectors (**A**) and the orbital under investigation possess well-defined symmetries in respect to the planes. The $d_{x,y}$ orbital has always odd reflection symmetry. Linear horizontal polarised light (LH) is even(odd) when reflected about the yz(xz)

planes. For linear vertical polarised light (LV) the situation is reversed. Hence, when the electronic state is probed with LH the photoemitted intensity is zero for the k_x=0 axis (the yz plane) as the scalar product is odd (even $\mathbf{A}\cdot$ odd $|\phi_i\rangle$). On the other hand, LH polarisation has both even and odd components when the xz plane is considered. For the orbital under investigation the even component of LH gives zero intensity in the photoemission spectra, whilst the odd one gives finite matrix element. As

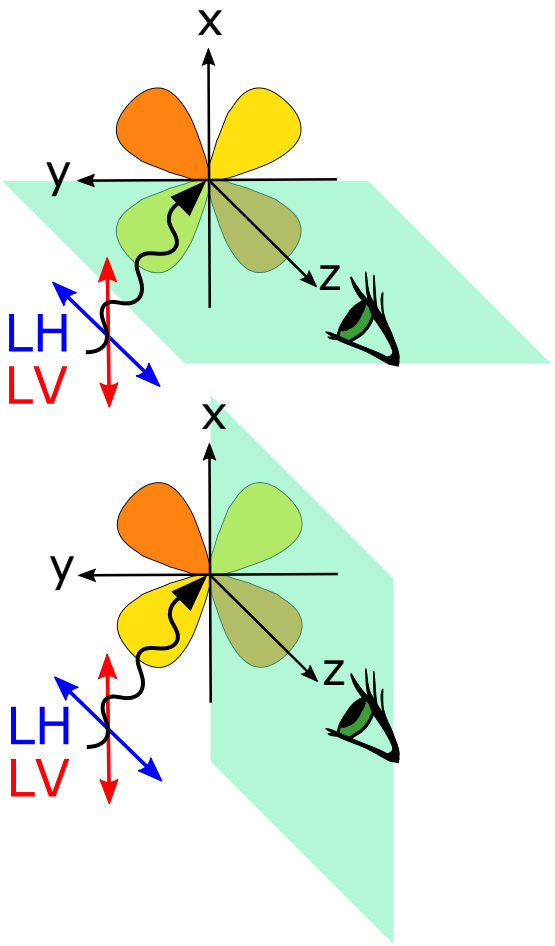

Figure 1.3: Symmetry selection rules for a $d_{x,y}$ orbital. Both the light polarisation vectors and the orbital possess well-defined parity in respect to the yz and xz mirror planes

mentioned above, LV presents the opposite situation. The vector **A** lies in the xz plane (even symmetry) and zero intensity (odd scalar product) is found along the k_y=0 axis in case of odd orbitals such as $d_{x,y}$. Conversely, the vertical polarisation is odd under reflection in respect to yz and an overall even scalar product is obtained.

Finally, the dipole selection rules still hold and determine their conditions for a non-zero single-electron matrix element. The most important one requires the single electron satisfies $\Delta l=\pm 1$ and $\Delta m=0,\pm 1$. In case the spin degeneracy is lifted by spin-orbit coupling, similar laws are defined for the total angular momentum. In particular, $\Delta m_j=0$ for linearly polarised light and $\Delta m_j=\pm 1$ circularly polarised light. The spin quantum number is left unaffected $\Delta S=0$.

1.2. Revealing the electronic character: Resonant Photoemission

Resonant photoemission spectroscopy (ResPES) a powerful and element-selective technique to investigate the orbital character of the valence states.[19]

The keystone of ResPES is the exploitation of the chemical selectivity intrinsic of photon absorption. When the photon energy is tuned at an absorption edge of one of the material's elements (i.e. at resonance), a secondary process can verify beside normal photoemission. A naive description is sketched in Figure 1.4, where the ResPES proccess is represented by two separated steps. The first step is the core excitation, the photon is absorbed by a bound core electron. The electron is transferred to the empty conduction states and the system is highly excited because to the presence of the core hole. The second step is an Auger process. The excited electron decays and the released energy is exploited to emit a secondary electron from the valence bands. As for conventional photoemission, the picture presented above is oversimplified and the whole process should be coherently described by a one-step model. Yet, this very basic framework already shows that the ResPES's initial and final states coincide with those of the conventional photoemission process reported in Figure 1.1. Hence, the two process interfere and the photoemitted intensity from the valence state is strongly enhanced at resonance. More precisely, the dipole selection rules hold and only the portion of the elec-

tronic bands originated from the orbitals of the element involved in the absorption intensify.

The power of this technique is best exploited in complex materials (i.e. where more than one atomic species are present). The ResPES capability to select the chemical specie (absorption edge) and the orbital character (dipole selection rules) disentangles the contributions of the single elements to the whole band structure. Finally, band structure originated by different oxidation states of the same element can be tracked by exploiting the chemical shift of core levels for different valency states.

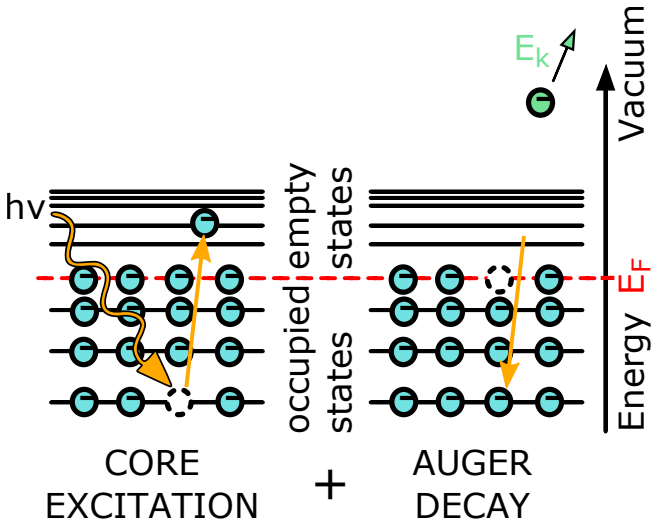

Figure 1.4: Resonant photoemission can be regarded as a 2-step process. In the first step a core electron is excited in an empty state near the Fermi level through photon absorption. The subsequent electron decay leads to the emission of a secondary electron (Auger decay).

2. Methods

> Le travail était là.
> On travaillait bien.
> Il ne s'agissait pas d'être vu ou pas vu. C'était l'être même du travail qui devait être bien fait.
>
> Charles Peguy - L'argent (1913)

In this chapter the experimental setup used in this thesis work are described. The main activity has been performed at the Nanofoundries and Fine Analysis (NFFA) facility that includes the Advanced Photoelctric Effect (APE) beamline in the experimental hall of the Elettra synchrotron radiation facility in Trieste.[6, 24] The techniques exploited for this work among those available at this open-to-users facility are illustrated in the first section of this chapter. The second section is dedicated to the description of the I09 beamline of the Diamond Lightsource (UK) radiation facility. This beamline has been employed to investigate the electronic properties of TiO_2 and their evolution following *in-operando* molecular oxygen adsorption at the sample's surface. Finally, the last section is dedicated to a brief description of the theoretical calculations performed during this thesis work.

2.1. *In-situ* experiments with synchrotron radiation: the APE-NFFA laboratory

The main features of the APE beamline were described by Panaccione and collaborators.[24] Two fully independent lines constitute the APE laboratory, each of them receives photons generated from one of two independent dedicated APPLE-II undulators.[25, 26] The latter are mounted in a chicane configuration on the same straight section of the Elettra storage ring (i.e. between two bending magnets). The electron trajectory between the undulators are bent by ~2 mrad angle to obtain the entirely independent double branch scheme sketched in Figure 2.1. The two branches exploits different photon ranges. Low Energy one (APE-LE) is served with VUV photons (hν= 15-90 eV) and it is dedicated to high-resolution spin and angle resolved photoemission spectroscopy. The second branch receives photons in higher energy range (hν= 140-1500 eV) and is thus named High Energy branch (APE-HE). It is used to investigate low dimensional magnetic systems and has been recently equipped with a cell to study surface reactions under atmospheric pressure conditions. Finally, both the APPLE-II sources provide full light polarisation tuning (i.e linear horizontal LH, linear vertical LH, circular right CR, and circular left CL).

The two end-stations are mutually connected through a suite of communicating UHV transfer chambers. Moreover, thin film deposition chamber as well as surface preparation and characterisation tools are available without breaking the UHV conditions. The whole infrastructure therefore supports the manipulation and characterization of the samples directly connected to surface-sensitive probing technique using Elettra synchrotron facility. All the surface related problems were therefore circumvented by allowing the synthesis and the characterization within the same UHV manifold (*in-situ*).

2.1.1. APE-LE

The APPLE-II undulator of the APE-LE branch was appositely designed with a quasiperiodic arrangement of the magnets.[26] This choice was made to suppress the higher harmonics and obtain high spectral purity in the monochromatic photon beam over a large photon energy range.[24] A dispersive monochromator with three interchangeable gratings allow to tune the photon energy between hν= 15 eV to 90 eV. The optical path continue with an exit slit followed by a toroidal refocusing mirror. The

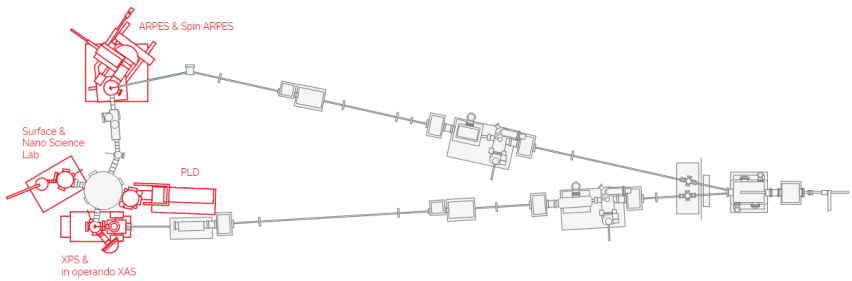

Figure 2.1: APE laboratory scheme showing double branch beamline strucutre and the interconnected UHV system, which allows to perform *in situ* surface experiments on as-grown samples. *Adapted from NFFA web-page*[6]

best photon resolution is found to be $\frac{E}{dE} = 30000$ corresponding to photon flux $> 2 \times 10^{11} < \frac{\text{photon}}{s}$. The scheme of the Spin-ARPES setup is reported in Figure 2.2. The photon beam impinges on the sample at 45° off-normal angle and with average spot size of $150 \times 50\mu m^2$. [6, 27] The sample is hosted on a manipulator with five-degrees of freedom (i.e. x, y, z, polar and tilt angles). The axis coordinates are chosen to have the z axis along the sample normal (i.e. aligned with the analyser axis) and the x direction aligned with the manipulator vertical axis. Rotations of the sample around the x (polar) and y (tilt) axes allow to explore wider portion of the reciprocal space. Moreover, the manipulator is equipped with a cryostat allowing sample cooling down to about 15 K by circulating liquid helium. The photoemitted electrons are collected by the Scienta DA30 hemispherical analyser [28], capable to resolve both energy and momentum distribution of photoelectrons within ~30° cone acceptance. The hemispherical analyser consists in two main parts: a straight section (i.e. the nose) and the hemispherical body. The nose is made by a series of axially symmetrical electrostatic lenses and a set of extra electrodes that resolve the emission angle of the photoelectrons. The electrostatic lenses also tune the electrons kinetic energy to match the pass energy (E_p). Then the electrons travel through the hemispherical condenser that acts as a energy pass-band filter with resonance frequency equal to E_p. The applied voltages fix the energy window $E_\Delta = E_p \pm \Delta$. The kinetic energy of a focused photoelectron must matches E_Δ to reach the exit slit without hit the hemispherical plates. In particular, the faster the electrons the larger possible orbit will be performed and vice versa. The photoelectrons that passed through the exit slit are then projected onto the exit plane and

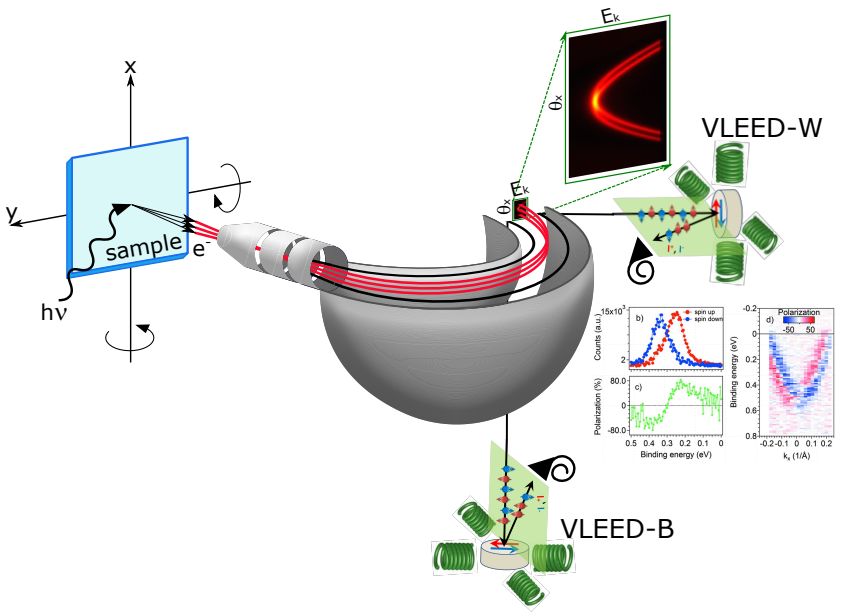

Figure 2.2: Scheme of the Spin-ARPES setup installed on the APE-LE endstation. Sample Red lines represent the electron beam trajectory inside the analyser reaching the MCP together with their angular vs energy dispersion. Black hemispherical trajectories indicate the electron beam path to the VLEED scattering chamber.

multiplied by a two Micro Channel Plates (MCP) stacked in Chevron configuration and excite the phosphorous screen. The screen fluorescence is finally recorded through a window by the CCD camera placed in air. The MCP are formed by a dense matrix of electron multipliers, each of them exploiting the secondary emission processes to amplify the signal. This position-sensitive signal amplifier allows to simultaneously resolve the kinetic energy distribution of the photoelectrons on the axis defined by the energy band E_Δ and their angle of emission Θ(readily converted to $k_{||}$) along the entrance slit. The formed image consists in a two dimensional map of energy vs momentum ($k_{||}$) dispersion. The data are therefore acquired in display mode, according to the selected interval of photoelectron energies and momenta. In the geometry of APE-LE, the analyser slit is aligned with the manipulator rotation axis (i.e. the x direction in Figure 2.2). The extra electrodes present in the DA-30 analyser can suitably select the incoming photoelectron directions included in the acceptance

cone of the cylindrical lenses (30° at maximum) to obtain (k_x, k_x) isoenergy maps. Moreover, a vectorial spin polarimeter has been implemented on the ARPES analyser. The vectorial polarimeter is based on the Very Low Energy Electron Diffraction (VLEED) which exploits the exchange coupling between the photoelectrons' spin and a ferromagnetic target in a reflection geometry (see ref. [29] and reference reported therein). The two VLEED scattering chambers are mounted at 90° with respect to each other as sketched in Figure 2.2. Each one of the chambers receives the energy/momentum filtered photelectrons from a dedicated variable aperture placed in the exit plane of the analyser. Two independent set of electrostatic (i.e. non affecting spin) lenses and retarding potentials focus the photoelectrons onto the VLEED targets and tune their kinetic energy to the maximise the reflectivity. The near-normal reflectivity is then measured by channeltron amplifiers. In such a way the vectorial the spin polarisation can be reconstruct upon measuring all the three components. The VLEED-B polarimeter measures the spin component aligned with the y-axis (perpendicular to the analyser slit, parallel to the sample surface). VLEED-W probes the other in-plane spin polarisation component, i.e. aligned with the analyser slit. Finally, both the VLEEDS measure the out-of-plane component (aligned with the z axis, namely the surface normal), which allows to cross-normalise the data. The APE-LE chamber is also provided with a Low Energy Electron Diffraction (LEED) setup to *in-situ* probe of sample surface crystal quality.

All the ARPES experiments conducted at APE-LE were performed at a base pressure $< 10^{-10}$ mbar. The samples were cooled at Nitrogen temperature and the overall energy resolution was set to ~40 meV for conventional ARPES and ~110 meV for Spin-ARPES experiments, angular resolutions were 0.2° and 0.5°, respectively.

2.1.2. APE-HE

The High-Energy (HE) experimental endstation of APE beamline is served by an APPLE-II type undulator, which provides full polarisation control and tunable photon energy in the range from 150 eV to 1600 eV [25]. The optimum resolution is $\frac{E}{dE} > 8000$ at hν= 400 eV and $\frac{E}{dE} > 3000$ at hv > 900 eV. The photon flux is ~5×10^{10} photons/s and the beam spot on the sample is about $500 \times 200 \mu m^2$ size. The sample is hosted on a 4 axis manipulator equipped with a cryostat for sample cooling down to 50 K X-ray Absorption Spectroscopy (XAS) is performed in total electron yield

(TEY). In the absorption process and the subsequently de-excitation generate a number of photoelectrons (mainly Auger and scattered secondary electrons). The photocurrent is directly proportional to the absorption probability and it will be higher in correspondance of chemical absorption edges. The TEY spectra is obtained by measuring the drain current that flows from the ground to neutralise the ionised sample with a picoamperometre. X-ray Photoemission Spectroscopy (XPS) spectra were acquired by a hemispherical Omicron EA125 electron energy analszer. The detector is equipped with 7 channeltrons and the global resolution was set to ~500 meV.

2.1.3. Thin film growth technique: Pulsed Laser Deposition

Pulsed laser light had been exploited for materials' ablation since 1965. [30] However, the investigation boom triggered by high-temperature superconductors [31] fully revealed the flexibility, versatility, and speed of the Pulsed Laser Deposition (PLD) process and its capability to fabricate high-quality samples. [32–36] The processes involved in the deposition are complex and a full description goes beyond the aim of this manuscript. Detailed theoretical study [37] as well as extensive reviews [35, 38] can be found in the literature. A intuitive and schematic picture is given in the following. The main features of a PLD experimental setup are sketched in Figure 2.3. A laser beam is focused on a target containing the exact composition of the material to be grown, either as polycristalline powder or single crystal. For suitable laser's power density, the material is unable to dissipate the absorbed energy via thermal conduction. As a consequence atoms are ablated from the target's surface and form the so called "plume". It is the plasma produced by the interaction between the laser pulse and the evaporated species accelerated along the target surface normal. [36] The laser used in this work is an UV excimer laser with 10 ns pulse duration. Therefore, a power density of ~50-100 $\mathrm{MW\,cm^{-2}}$ is needed to successfully ablate single atoms from the target. [35]. An iris may be introduced in the laser's optical path to tune the laser fluence. Eventually, the expanded plume condense on a single crystalline substrate. Stoichiometric, substrate-driven crystalline growth may occur if the physical-chemical nature of the substrate and the kinetic conditions are met. The substrate is hosted on an heating stage to improve the mobility of the adsorbed atoms and to provide higher crystal quality.

Background gases (e.g. O_2, O_3, N_2, Ar) may be introduced in the

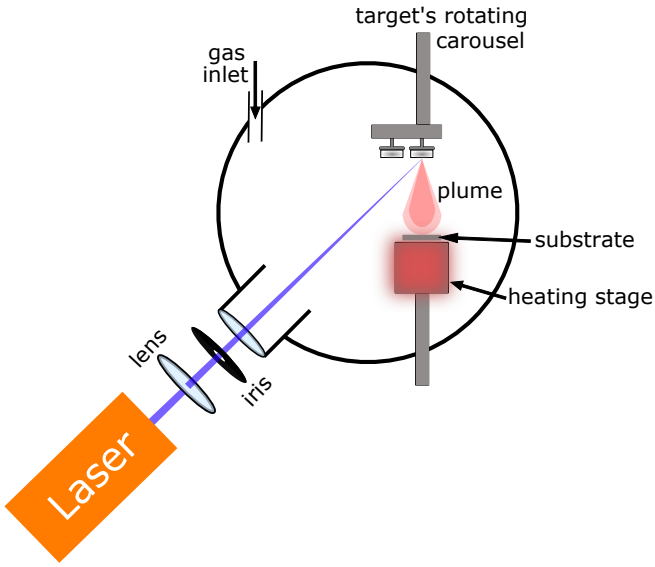

Figure 2.3: Sketch of the main features involved in a PLD process

chamber during deposition to prevent the re-evaporation of the volatile species from the film. However the optimal background pressure must be carefully set not to compromise the film stoichiometry. Background pressures exceeding 10^{-2} mbar increase the collision rate of the ablated species. As a result, the plume deviates from the $\cos(\Theta)$ distribution and turns into an elliptical shape. The ablated atoms may decelerate until they reach the stopping distance where the plume is thermalized. In this scenario, the substrate has to be placed in correspondance to the thermalised edge of the plume. No growth will occur for farther distances. On the other hand shorter distances may cause the substrate to be sputtered by the incoming fast elements. In the case of complex oxides, O_2 background pressure is a powerful tool to tune the amount of the oxygen vacancies in the sample.[39, 40]

The PLD apparatus available at APE-NFFA laboratory is directly connected to the UHV manifold of the APE-NFFA suite. The as-grown samples can, thus, be transferred to both the beamline's endstations without UHV interruption, fully exploiting all the surface analysis techniques available at APE-NFFA. Moreover, *in-situ* structural characterisation can be performed by means of LEED diffractometer and a room temperature

Scanning Tunnelling Mycroscopy (STM) apparatus, both connected to the beamlines through the UHV transfer system. *In-situ* cleaned W tip was used for the STM imaging *Ex-situ* structural characterization is routinely carried out by means of a four-circle diffractometer with a Cu K_α radiation source. In particular, high-intensity configuration has been used in the present thesis work as it provided acceptable photon flux to perform effective samples' characterisation. The overall resolution was worsened because both the Cu $K_{\alpha 1}$ and the $K_{\alpha 2}$ wavelengths are selected. Beam spot on the sample is in the mm^2 range.

2.2. Beamline I09

Measurements were also performed exploiting the soft X-ray branch of the I09 beamline hosted at the Diamond Lightsource Source, UK. [41] The beamline is sketched in Figure 2.4 and it consists in two branches. The high-energy endstation (EH2) receives tunable soft x-rays from 452 eV to 4222 eV and hard x-rays up to 18 keV essentially in the same position and with the same energy resolution. The purely soft X-ray endstation (EC) is served by a 4.5 m APPLE II helical undulator, capable of polarization control [25]. The photon energy is continuously tuned in the 200-2000 eV range by a monochromator featuring a 3 grating system. The spot size on the sample is ~$15 \times 30 \mu m^2$ for focussed configuration. However, the monochromator has been tuned to suppress the higher order components coming from the beamline optics. The chosen configuration was the best compromise between resolution, flux and higher order rejection. maximum spot size obtained in completely defocused configuration have a $300 \times 300 \mu m^2$ area. The samples were cooled down to 90 K. The overall energy resolution was ~250 meV. Molecular oxygen was fluxed on the sample surface through a metallic capillary and the amount of O_2 has been monitored by means of a Residual Gas Analyser available in the experimental chamber. Base pressure in the experimental chamber was 10^{-10} mbar, up to a maximum oxygen partial pressure of 4×10^{-10} mbar.

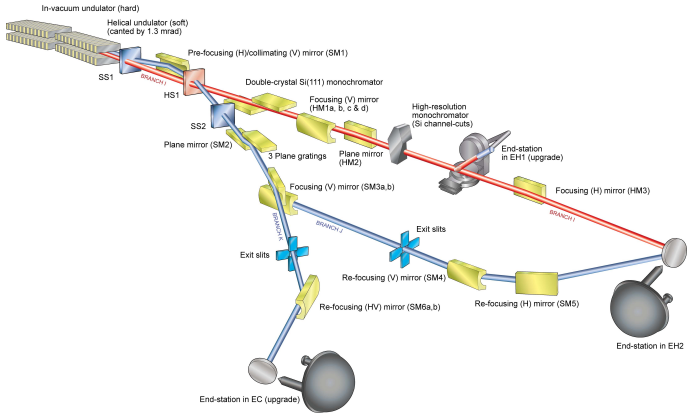

Figure 2.4: Scheme of I09 beamline layout. Adapted from [42]. Details can be found in the work of Lee and Duncan [41]

2.3. Modelling: DFT calculations with QuantumESPRESSO code

This section briefly describes the computational methods used for the calculation of the electronic properties of $SrNbO_3$. Density Functional Theory (DFT) is an *ab-initio* approach to calculate the ground-state properties of solids. [43, 44] DFT's strength is the capability of substitute the many-body puzzle associated with the Shrödinger equation with a much simpler one-body formulation based on the electronic density $n(\mathbf{r})$. The essential prerequisite is the existence of a bijective mapping between the many-body system and $n(\mathbf{r})$. This has been demonstrated in 1964 by the two *Hohenberg and Kohn Theorems* [45], whose diagram is reported in the left panel of Figure 2.5. Hohenberg and Kohn showed that for any n-body system of interacting particles in an external potential (V_{ext}), the latter is uniquely defined by the ground state density of the system ($n_o(\mathbf{r})$). The vice-versa automatically comes from the solution of the Shrödinger problem as V_{ext} determines all the eigenfunctions $\psi_i(\mathbf{r})$, including the ground state $\psi_o(\mathbf{r})$, and eventually $n_o(\mathbf{r})$ can be defined. The second theorem states that the energy of the system can be expressed as a functional of the electronic density $E[n(\mathbf{r})]$, whose minimum coincides with the energy of the ground state. Hence, the ground state properties are completely described by the functional $E[n_o(\mathbf{r})]$, the latter being determined through variational principles. To practically apply these results, the formulation

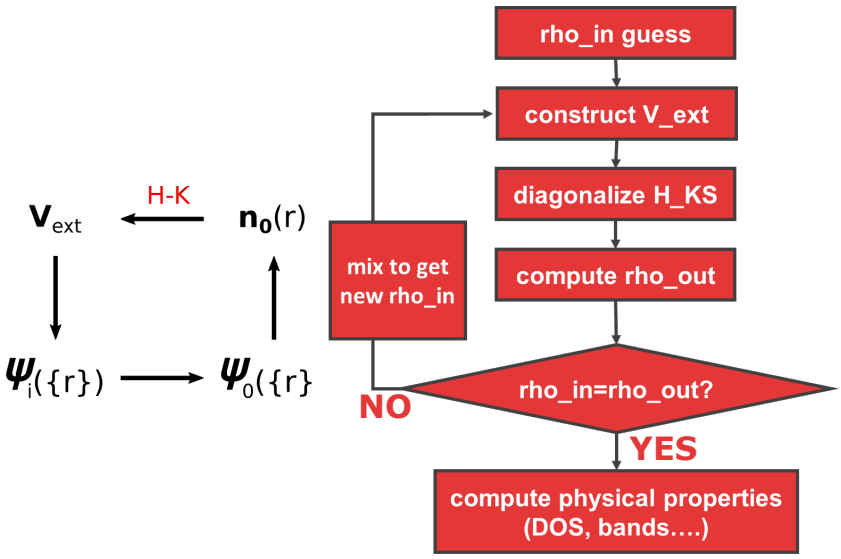

Figure 2.5: *Left* Schematic diagram of the first Hohenberg-Kohn theorem. *Right* Work-flow diagram of the self-consistent loop

of the functional E[n(**r**)] by means of explicit wavefunctions is mandatory. The most common approach was proposed by Kohn and Sham [46]. The Kohn-Sham method is based on the idea of auxiliary system: the original many-body problem is substitute with a fictitious non-interacting electronic system, provided that the ground state density $n_0(\mathbf{r})$ is left unchanged. Hence, a simpler set of independent particle equations has to be self-consistently computed instead of the complex interacting many-body problem.

The electronic properties of $SrNbO_3$ presented in this dissertation have been calculated by means of the QuantumESPRESSO open-source code. [47] The functional was implemented using the Generalised Gradient Approximation [48] with the parametrisation provided by Perdew-Burke-Ernzerhof (PBE) [49]. As the effective potential in the Kohn-Sham formulation is a functional of the density, a self-consistent solution has to be found iteratively. The right panel of Figure 2.5 reports the work-flow of a general self-consistent calculation. An initial guess for the electronic density has to be formulated to derive the starting effective potential V_{ext}. By means of variational methods the Kohn-Sham problem is diagonalised and the out-coming Kohn-Sham equations are used to compute the new elec-

tronic density. At this point the self-consistency of the process is checked, namely the calculated density is compared with the input guess. If the two coincides within the desired accuracy, the calculation is said to be *converged* and the physical quantities (e.g. DOS and band dispersion) can be derived. Otherwise, the process has to be repeated with a new guess obtained by a suitable superposition of the input and output densities.

In the DFT code, the Kohn-Sham equation are reduced to a system of coupled algebraic equations by decomposing the wavefunctions on the complete plane-wave basis set. Practically, the number of plane waves has to be finite and is controlled with the *ecutwfc* parameter according to the following equation:

$$\frac{\hbar^2 \left|\mathbf{k}+\mathbf{G}\right|^2}{2m} < ecutwfc \tag{2.1}$$

Large values for ecutwfc means better precision, but it implies more onerous calculation as well. Finally, localised electrons (e.g. the core electrons) increase tremendously the computational bill, as a bigger set of plane waves (i.e. higher ecutwfc) is needed to efficiently describe their steep wavefunctions. An efficient tool to reduce the number of plane waves is based on the concept of pseudopotentials. The basic idea is to simplify the complexities of the real Coulomb potential by introducing a fictitious effective pseudopotential. This is constructued in such a way it carefully simulates the real potential far from the nuclei (i.e. where the valence electron wavefunction is mostly delocalised), while it substitutes the divergent part with a softer (non-physical) shape. Of course, this approach can be applied only when the exact description of the core levels is not required.

3. All-Resolved PES

Circular Dichroism and Spin Polarisation measaurements on $NbSe_2$.

Hey Ahab hoist that sail
You gotta stand up straight
When you ride that whale

Elton John - Hey Ahab (2010)

3.1. The struggle to access the spin information

Probing and understanding the spin texture of materials has recently raised a lot of scientific interest. It gives key access to many phenomena as proximity effects or magnetism. Recently, high interest has risen for the investigation of the more exotic properties driven by spin-orbit in-

teractions such as in Rashba systems [50–52] and topological insulators [53, 54]. Tailored systems or heterostructures allowing fully manipulation of the electron spin open the way to augmented miniaturisation. Moreover, the information carried by spin instead of the traditional charge motion has been conjectured to be the watershed for more efficient devices with extremely low heat load.[55, 56]

In this scenario, big effort has been put to develop a technique capable of efficiently detect the spin-polarisation of the final photoelectron states. Conventional ARPES is a powerful tool to access the band structure of materials, while spin-ARPES constitutes the most direct and reliable probe of materials' spin texture. This technique simultaneously filters all the quantum numbers of the photoelectron final state in vacuum, so that it could be called an All-Resolved-Photoelectron Spectroscopy (All-RPES). In synchrotron radiation experiments, the photon degeneracy is smaller than one and all photoemission events are independently generated by a chaotic light source. Therefore, photon-photon correlations can be discarded and the weak excitation picture holds. The perturbative approach warrants that the measured spectral function is linked to the ground state electronic structure and its low energy excitations, while the final state is revealed by the detector. The detected photoemission intensity is determined by the selection rules entering the matrix elements of the transition between all the initial electron states of the sample and the measured final state. In particular, the selection rules are governed by the experimental symmetry and the relative orientations of all the symmetry lowering parameters of the material (e.g. orbital ordering, band structure, magnetisation) as well as the polarisation state of the incident photons. As a consequence, the experimental geometry must be fully understood and controlled when designing the ARPES experiment or when analysing ARPES data. This holds for the spin resolved data too. The basic assumptions of the dipole approximation invokes spin-conservation, yet photoemission intensities may influence the overall signal. Consequently, the spin polarisation measurement is possibly affected too. Theoretical work by Cherepkov [57] shows the directionality inherent to the photoemission experiment causes finite spin polarisation to photoelectrons originated from spin-degenerate spherical-symmetric initial states. Experimental proofs were achieved by Shönhense and co-workers for both unpolarised and linearly polarised light. [58, 59] Exploiting the symmetries of topological surface states (TSS) Park and Louie predicted the spin polarisation of the photocurrent detected in spin-ARPES may orient very differently in

respect to the initial state.[60] More generally, unexpected spin-polarised (or unpolarised) signal may occur when the matrix element describing the whole transition results from different channels coherently interfering. Zhu et al. investigated the layer-dependent, SOC-driven spin orbital texture of the Bi_2Se_3 topological surface state. [61] They report a dependence of the photoelectrons' spin-polarization upon both the photon energy and light polarisation. Through a phenomenological layer-dependent model the authors related the detected variations to the interference between matrix element channels generated from different layers (i.e. different orbitals) that affects the whole photocurrent.[62] A similar approach has been successfully adopted by Riley and co-workers in the case of exfoliated WSe_2 TMDC. The keystone of this picture relies on the strong layer-locking of the initial spin texture probed with photoemission.[63] In layered materials the interference effects between spin-up and spin-down polarised photoelectrons arises from different layers of the sample where inversion symmetry is locally broken.[64] Besides the photon energy, the light polarisation may alter the spin of the photoelectrons too. It is well known that the GaAs source of spin-polarised electrons is activated by absorption of circularly polarised light, exploiting the direct gap at the centre of the Brillouine Zone. [65, 66] The quantum mechanical selection rules give the theoretical polarisation of $\pm 50\,\%$ for band gap photoexcitation. The sign of the spin polarisation of these excited electrons is determined by the light polarisation handedness and can be easily switched reversing the light helicity.[66] These results show the photoemission consists in an interband transition between an occupied band state and an unoccupied state of the material. The final state distribution therefore possesses the symmetries of the empty state involved in the process, although it is generally described as a plane wave state (continuum limit) in the high kinetic energy range. Furthermore, in All-ARPES the photocurrent is selected in respect to k. The spin polarisation is no more angle-averaged like in angle-integrated PES and may present angle dependence, as experimentally reported for core levels [58, 59]. This hinders the quantitative determination of the spin polarisation in ARPES, as the hybridised orbitals in the valence band and their related symmetries are not straightforwardly identified. Overall, the spin-polarised initial states are regularly assessed in the spin-ARPES through the detection of the final state spin, yet the ARPES matrix elements may modify the photocurrent to the point that the absolute value of spin polarisation should be treated with care. A renowned example comes from the experimental

investigations of the TSS spin texture. The spin-polarisation measured in All-RPES experiments is generally lower than the theoretically predicted 100 % and can not be merely ascribed to sample quality, or experimental resolution. [62, 67–69] As discussed above, one possible cause yielding unexpected spin polarisation originates from the photon energy dependence. However, the light polarisation can also affect the spin polarisation of the photoemitted electrons. Linearly polarised light has been reported to flip the spin polarisation in Bi_2Se_3 [70]. Exploiting optical selection rules and the entangled spin-orbital texture up to 100 % spin polarisation has been obtained.[62] Moreover, interference effects in the spin photocurrent have been shown by Bentmann and collaborators in the case of linear dichroism have been reported in the Rashba splitted $BiAg_2/Ag(111)$. The authors attributed them to the intrinsic properties of the initial surface state. [71] The influence of the polarisation handedness have been investigated [72, 73]. Razzoli and co-workers investigated the spin polarisation of the bulk centrosymmetric 2H-MoS_2 and reported sign reversal of the spin polarisation upon the light helicity. Finally, the effects of circular polarised light on the spin photocurrent originated from the Dirac-cone-like W(110) surface state have been investigated by Miyamoto et al. [73] The observed complex spin-polarization texture arise from a superposition of the (extrinsic) experimental geometrical parameters of the experiment and the intrinsic spin polarisation of the initial state. All the effects enters the transition matrix element, which accounts for the orbital components of initial and final states that reflect the crystal symmetry, as well as the light polarisation and energy together with the angle of incidence.[73]

Despite the strong interest in the quest for exotic spin-texture has tremendously boosted the developments and installations of new spin polarimeters in the past decade [74–76], the data acquisition rates are still limited by the inherent low efficiency of the spin filtering process. Furthermore, the availability at large scale facilities of state-of-the-art instrumentation for All-RPES measurements is often overwhelmed by the high-demand of user's community. Circular Dichroism (CD) in ARPES is relatively more easily available technique, as circular polarisation can be mastered at beamlines featuring Apple-type undulators or at laser sources using quarter-wavelength filters. The measurement efficiency is of CD is higher than spin-ARPES (two sets of measurements instead of 10E-2 statistics). The idea to possibly link the spin-information to the CD-ARPES spectra has therefore been explored by several investigators. The CD signal is obtained by taking the difference of two ARPES spec-

tra measured with opposite helicity circular light. The explicit formula is $I_{CD}=\frac{I_{CR}-I_{CL}}{I_{CR}+I_{CL}}$ where CR (CL) are the circular-right(-left) polarisations respectively. Magnetic dichroism in photoemission or in the angular distribution of core level has proved to be a useful tool to investigate the symmetry of magnetization and its order parameter. Very direct evidence was reported by LMDAD experiments (Linear Magnetic Dichroism in the Angular Distribution) performed by Rossi et al. [77]. In their work the authors investigate the core levels of iron, whose degeneracy completely removed by the exchange interaction. The whole set of m_j values associated to the core holes is consequently distributed on the energy scale and. In this scenario, the photoemitted intensity is directly attributed to the space orientation of the specific m_j core wavefunction that couples with the linearly polarised photon beam. As a result, strong dichroic effects in photoemission signal can be achieved by changing the experimental geometry (e.g. by varying the light polarisation, or by inverting the magnetisation direction). Rossi and co-workers paper [77] and other studies demonstrated that photoelectron dichroism can be exploited as a tool to access ferromagnetism as well as atom-specific magnetometry of the surface.[78–81]

However, extended and energy dispersive states are less straightforward to be analysed in terms of intensity. Nevertheless, some reports on topological insulators claim the CD signal is connected to the spin of the initial state either directly [82] or indirectly through the orbital angular momentum (OAM). The latter has been reported to be aligned anti-parallel to the spin by the strong SOC of the system. The spin-momentum locking of the TSS has been thus inferred from the CD data. [83–85] Both linear and circular ARPES dichroisms were exploited to investigate the magnetic properties of the Ni(111) surface by Mulazzi and collaborators. [86, 87] If the experimental geometry mathces a mirror symmetry plane, parity rules affect the detected intensity. In this case, matrix element arguments can be exploit to infer properties of the initial state (e.g. by examining the dichroic response of both non-magnetised and magnetised samples). [86] For other geometries, theoretical modelling was performed to assist the interpretation of the measured intensities. [87] Moreover, non-trivial dichroic signal has been reported also in materials with small SOC. Mulazzi and collaborators measured the Schockley surface state in the L-gap of non-magnetic Cu(111) and observed a strong response to linear dichroism as well as in the CD spectra. [22] Their experiment showed how the plane-wave photoelectron final state is not strictly adequate to interpret

the measured intensity in ARPES spectra. The large variations of the photoemitted intensity distribution along the parabolic surface state call for theoretical description beyond the free-electron approximation for the final state. Few years later, Kim and co-workers investigated the CD of both Cu(111) and Au(111) Schockley states.[88] Despite the very different strength of SOC in these two materials, they found the OAM magnitude is quite similar in the two samples state. To infer the spin properties the authors rely on DFT calculation combined with an effective Hamiltonian which explicitly established the relation between OAM and spin in the two systems. However, strong modulation and sign reversal of the dichroism as a function of the impinging photon energy have been reported by several groups investigating the surface states of topological insulators [89–91] and BiTeX Rashba semiconductors. [92, 93] These works attribute the photon energy dependence of the CD to phase differences between channels entering the whole matrix element. Scholz and co-workers ascribe the dichroism evolution to purely final state effects [90], while other groups assign the same phenomena to complex interplay between the wavefunctions of the initial states (e.g. non-trivial orbital textures, atomic cross-sections, and possibly spin-momentum locking). [61, 93] [94] Finally, the change in the dichroic signal does not automatically reflect the spin-polarisation of the energy and angle filtered photoelectron current. Sánchez-Barriga and collaborators measured both the circular dichroism of the TSS of Bi_2Se_3 as well as the spin-resolved ARPES signal. [94] The authors report the spin polarisation of the photocurrent is robust upon the photon energy as well as for different light polarisation and helicity in the 50-70 eV photon energy range, while the CD undergoes a complete sign reversal in the same energy range. On the other hand, strong modulation of the photoemitted electron spin has been found for 6 eV circularly polarised light. Overall, all this works evidence the need of a better understanding of the spectral function that is effectively measured in a given experiment. A possible approach is to perform band calculations and then photoemission calculations accounting for detailed description of both the initial and final states to compare with experiments and help interpretation of the spin degree of freedom in the materials.

This rather complex scientific problem is here addressed by investigating the photoemission intensity of bands characterised by well-known spin polarisation. The effects of variations in the transition matrix element on the detected photocurrent were probed as a function of the experimental conditions. The experiment was performed fully exploiting the advanced

features of the APE-LE beamline: tunable energy, high photon energy resolution, entirely controllable light polarisation, combined with the All-Resolved PES equipment described in chapter 2. The chosen sample is the exfoliated clean surface of 2H-$NbSe_2$ bulk crystals, which hosts strongly spin polarised bands dispersing up to the Fermi level. Spin-Resolved and Spin-Integrated ARPES spectra were measured as a function of the photon energy and light polarisation. The spin-ARPES proved to be quite robust against the changes in the matrix elements as driven by photon energy, whilst the circular dichroism undergoes strong variation and sign reversal. The results clearly demonstrate that in this case, and therefore in general, the spin-resolved information cannot be borrowed by circular dichroism in photoemission, e.g. inferring spin polarisation from CD is not justified. A brief introduction on the 2H-$NbSe_2$ system is given in the following paragraph prior to reporting the experimental results.

3.2. The $NbSe_2$ prototype: SOC and inversion symmetry

Niobium diselenide ($NbSe_2$) is a metallic layered system that belongs to the transition metal dichalcogenide (TMDC) materials. The latter constitute a class of 2D materials characterised by MX_2 chemical composition, where M and X are a transition metal and a chalcogen atom, respectively. The building block of the TMDCs crystal structure is called monolayer and is formed by three, single-element hexagonal lattices stacked in such a way the transition metal is sandwiched between two chalcogen layers (i.e. X-M-X). The unit cell is then composed by piled up monolayers along the c-axis direction, kept together by Van der Waals interaction. There are several polymorphic structures that may occur depending on the specific stacking of the layers. In this chapter the 2H-$NbSe_2$ phase, one of the most common, is investigated. The 2H-$NbSe_2$ unit cell reported inFigure 3.1 is made by two monolayers stacked in A-B fashion as can be seen in the side-view of Figure 3.1. From the top-view a graphene-like atom arrangement is recognised with the metal and chalcogen atoms placed at two inequivalent sites.

The resulting bulk unit cell preserves the inversion symmetry and the crystal is centrosymmetric. As time reversal symmetry holds in this sys-

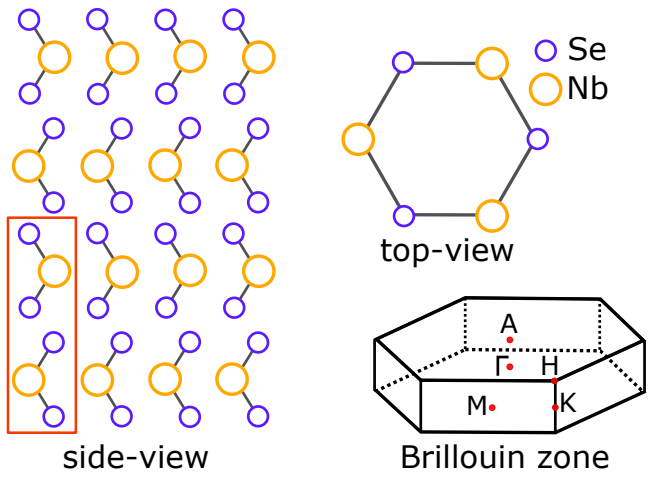

Figure 3.1: 2H-$NbSe_2$ crystal structure and Brillouin zone.

tem, the inversion symmetry forbids the removal of spin degeneracy to simultaneously satisfy E(↑,**k**)=E(↑,**-k**) and E(↑,**k**)=E(↓,**-k**). The constrain fails in the monolayer, which is not centrosymmetric. Hence, spin degeneracy can be lifted and SOC-driven spin polarised bands occur when suitable spin-orbit interaction is provided. TMDCs are generally characterised by strong SOC and spin polarised bands around the K (K') point have been predicted [95] and experimentally reported [96, 97]. The spin-orbit field arise from the crystal field and the electron momentum and it can expressed by $\mathbf{B}_{\mathrm{SO}} \propto (\nabla V \times \mathbf{k})$. This, combined with the C_3 crystal symmetry, leads to a nominally 100 % out-of-plane spin polarisation at K in the monolayer limit as the electronic wavefunction totally lies within the layer. Moreover, the sign of the splitting is linked to the valley index associate to the two inequivalent sublattices. This results in the so called *spin-valley locking* [98–101], where the spin polarisation is reversed in sign for K and K' points consistently with the time reversal symmetry. Finally, the A-B stacking along c-axis causes the second layer in the bulk unit cell to be 180° rotated in respect to the previous one. Hence, the spin-texture is exactly equal in magnitude, but opposite in sign. As a result, the spin polarisation cancels and the bulk band structure is spin degenerate as required by the global inversion symmetry.

Nevertheless, spin polarised states have been recently reported for the bulk centrosymmetric 2H-WSe_2 2H-$NbSe_2$ systems. [63, 102] The rea-

son of the unexpected spin polarisation lies in the electronic wavefunction in TMDC materials. The Van der Waals bonds are quite weak and the interlayer hopping is consequently rather small. This hinders the electrons to extend over both the layers of the Brillouine zone and leads to a wavefunction strongly localised within each monolayer. As this building block breaks the inversion symmetry, the system can host "hidden spin polarisation" [64]. Such a layer-locked spin texture [102] can be probed by spin-ARPES exploiting the surface sensitivity inherent to photoemission technique [63, 102].

Finally 2H-$NbSe_2$ presents a quite rich phase diagram, bearing collective electronic phases in the low temperature range. It hosts charge density waves below 33 K[103–105] and it becomes superconductor at even lower temperature (7.2 K)[103, 106]. Their description is well beyond the scope of the present chapter as the experiments were performed above the transition temperatures.

3.3. SpinARPES experiments, results and discussion

Commercial bulk $NbSe_2$ single crystals[107] were glued with the [0001] direction aligned along the surface normal. The (0001) is a good cleavage plane thanks to the weak Van der Waals bonds between the Se-Nb-Se layers. The samples were pre-oriented in plane by means of Laue diffraction and cleaved in UHV with the kapton scotch tape method. Spin-integrated ARPES and spin-resolved ARPES experiments were performed with the samples maintained at liquid nitrogen temperature of ~77 K (i.e. far from the collective phase transition temperatures). Figure 3.2 shows the band structure acquired with hν= 70 eV, which correspond to a Γ-K-M-K' plane of the Brillouine zone according to the inner potential reported elsewhere. [108] The cartoon sketches the Brillouin zone and the dashed rectangle emphasize the portion of the BZ measured by the ARPES detector. Energy vs. momentum dispersions along high symmetry cuts are also reported in the bottom panels of Figure 3.2 (i.e. from left to right Γ-M, K'-Γ-K and K'-M-K) and their locations on the Fermi surface are marked by the respective coloured lines. The very bright hexagonal contour centred at the Γpoint mostly arise from Nb-4d orbitals as well as the two concentric

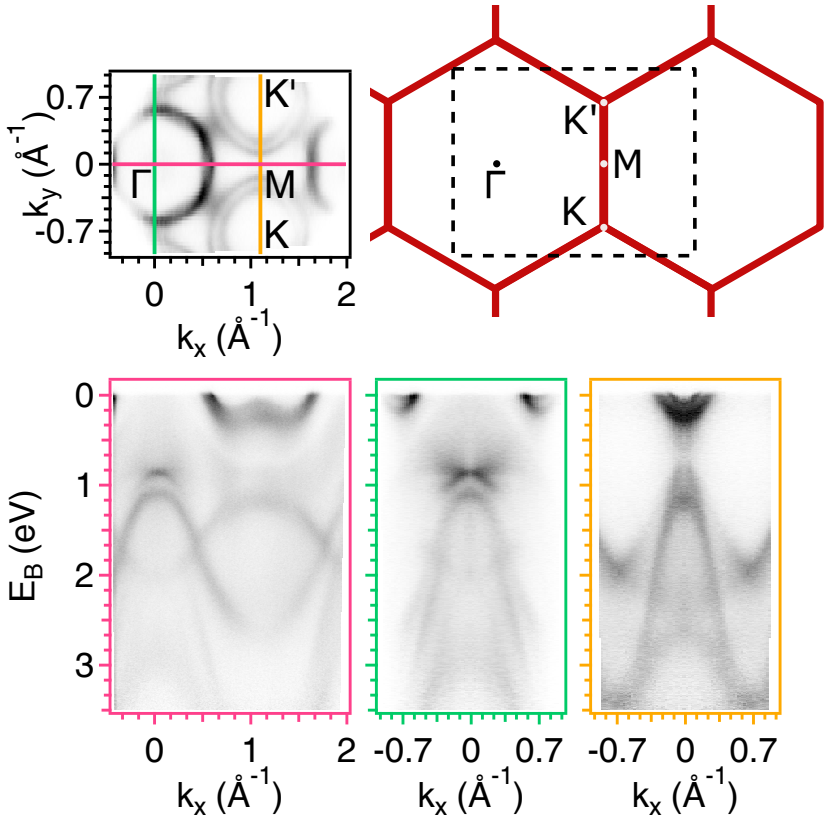

Figure 3.2: $NbSe_2$ Fermi surface measured with 70 eV linearly horizontal (LH) polarised light. A sketch of the Brillouin zone is also reported together with the BZ portion probed by the detector (dashed rectangle). Band dispersion along high symmetric direction (marked by coloured lines on the Fermi surface) are also reported. From left to right: Γ-M (pink), K'-Γ-K (green), and K'-M-K (yellow)

sheets centred at K and K'. The orbital character is mixed by the strong spin-orbit interaction of this system, In particular, the orbital character of the Fermi surface is mainly $d_{x^2-y^2}$ and d_{xy} near the zone corners, while d_{z^2} character is predominant close to the BZ centre. Finally, the last Fermi surface sheet is the so called "3D pancake" which derives mainly from the p_z orbitals and is centred at the Γpoint. The photoemitted intensity of the latter is much lower than the others at hν=70 eV and only faint signal of its presence is visible in the spectra due to unfavourable contrast in

respect to the other bands. [109, 110] For this reason, this state is best observed in the *bottom central panel* of Figure 3.2 and at hν=25 eV as reported in the *top left panel* of Figure 3.3. The "pancake" appears as a diffuse spectral weight, broadened in a wide range of binding energies up to the Fermi level, centred at the Γpoint. This is a consequence of the highly dispersive character of the P_z bands combined with the k_z broadening arising from the finite probing depth, $\Delta k_z = \lambda^{-1}$. At 70 eV photon energy, the electrons photoemitted from the Fermi level have a mean free path $\lambda(65\,\text{eV}) = 5\,\text{Å}$, i.e. $\Delta k_z = 0.2\,\text{Å}^{-1}$. Being the value of the c-axis of bulk 2H-$NbSe_2$ $c = 12.55\,\text{Å}$, the ARPES spectra are integrating the band structure over approximately two fifths of the BZ. The ARPES data measured along Γ-M as a function of the photon energy and for fixed linear horizontal (LH) polarisation are reported in Figure 3.3. Overall, the band dependence on the exciting energy (i.e. the dispersion along the k_z direction) is weak, consistently with the layered crystal structure of this compound. As reported in chapter 1, a way to access the band dispersion along k_z is offered by photon energy dependence. In particular, pure surface states as well as states whose electronic distribution is strongly localised along the direction perpendicular to the surface manifests essentially no k_z dispersion. The pockets appear to be confined in the Se-Nb-Se layer as their nearly undetectable k_z dependence indicate a 2D-like charge distribution. This is consistent with the expected Nb $4d_{x^2-y^2/xy}$ orbital character, mainly oriented within the layers. [63, 111, 112] Conversely, the band structure near the centre of the BZ derive from Se p_z and Nb d_{z^2} orbitals and manifest some dependence on the photon energy, reflecting the slight hybridisation between different layers. [105] As the Van der Waals bonds occur between the Se-Se atomic layers, the cleaved surfaces are most likely Se-terminated. However, the photoemitted intensities related to the Nb 4d orbitals are generally more prominent. This behaviour reflects the element specific photoionisation cross-sections relative to Nb-4d and Se-4p orbitals that hybridised in the valence band. The graph reported in Figure 3.3 summarises the cross-sections for Nb 4d and Se 4p orbitals. The former is always higher in the 20 eV to 65 eV photon energy range, but its magnitude falls about two orders of magnitude as the hνapproaches the Cooper minimum (located at about 85 eV). The cross section of the Se p orbitals does not have a Cooper minimum, although the intensity monotonically decreases for photon energies higher than 20 eV. At hν~70 eV the cross sections of Nb4d and Se 4p are almost equal and they cross between 75eV and 110eV photon energies. Consistently, the band dispersion

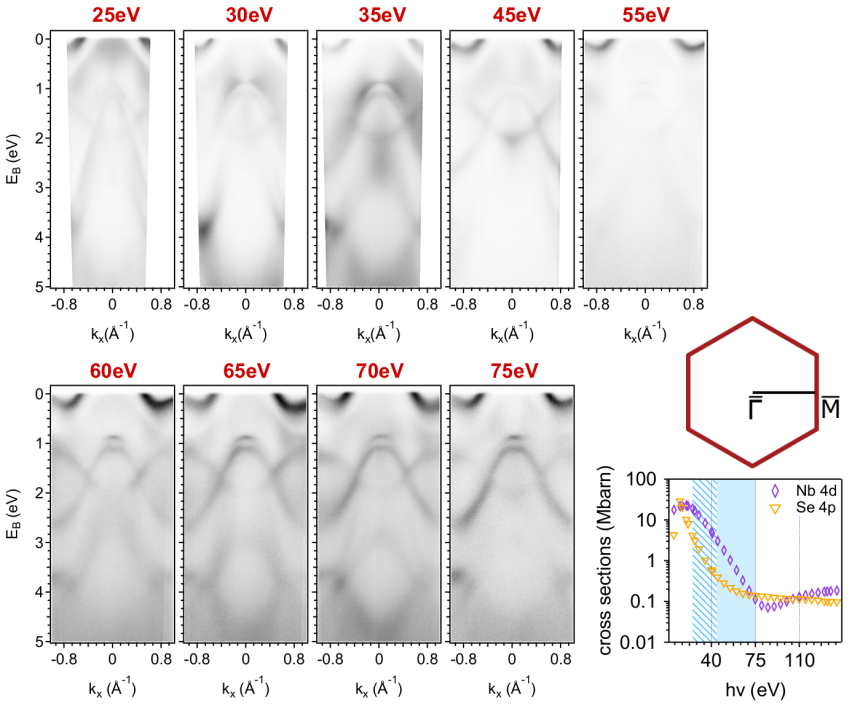

Figure 3.3: Photon energy dependence of $NbSe_2$ bands measured along Γ-M (as shown by the BZ cartoon) with LH polarisation. Photon energy was varied from 25 eV to 75 eV. The graph reports the element cross section for Nb 4d and Se 4p orbitals. The light blue coloured area marks the photon energy range explored with conventional ARPES. The pattern indicates where the spin-ARPES measurements were performed.

of both the pockets and the more dispersive states at the centre of the BZ have similar photoemitted intensity around ~70 eV photon energy. Following these observations, Se p character is attributed to the sharp bands dispersing between 1-3 eV binding energies. The fact that similar intensities are already observed at hν~60 eV may indicate deviations from the atomic behaviour arising from orbital's hybridisation within the bondings or reflect the resonance with the Se 3d core shell (~55 eV for the isolated Se atom). The latter case correspond to resonant photoemission introduced in chapter 1, a process where the electronic band structure arising from Se-4p orbitals can be selectively enhanced matching the excitation energy to the absorption edge of the selected element (Se in this particular case). Moreover, the absorption cross section is quite high at 25 eV

photon energy for both Se and Nb electron states (although is 4.5 times higher for the Nb). This photon energy corresponds to k_z close to the BZ centre (i.e. similar to 70 eV), consistent with the detection of the p_z-derived 3D-pancake band centred at Γ. The interpretation of the ARPES data acquired at hν=35 eV is less straightforward. The band dispersion looks different than both 25 eV and 70 eV photon energies although it also corresponds to k_z close to the Γ-K-M plane. This discrepancy may be interpreted considering the photoionisation cross sections and electronic resonances. The ratio between the Nb4d and Se4p cross sections is the highest of the whole energy range considered here ($\frac{\sigma_{Nb4d}}{\sigma_{Se4p}} \sim 8$). Moreover, the exciting energy is quite close to the absorption edge of the Nb 3p core levels (~55 eV for the isolated Se atom). Therefore, it can be inferred that the bands probed near Γwith 35 eV photon energy are mostly the $4d_{z^2}$ ones. This conclusion also accounts for the nearly absent spectral intensity of the 3D-pancake associated to Se p_z orbitals. However, the faint intensity photoemitted from the Nb $4d_{x^2-y^2/xy}$ pockets remains unclear. This is a warning bell calling for a description of the interaction as a whole throughout accurate matrix element, which is neglected by the naive picture here presented. The discrepancies could be ascribed to the hybridised nature of the valence states which deviates from the isolated atomic orbitals of reference. Hybridisation phenomena are generally expected in the TMDC systems because the spin-orbit coupling mixes the atomic orbital wavefunctions. Consequently, the photoionisation cross-section does not strictly hold as they rigorously describe the localised atomic states only. However, the reasonable applicability of these very simple criteria is consistent with the strong electron localisation within the layer of this material. [63, 111, 112] As discussed in the section 3.2, the latter is very important to successful spin detection even in the bulk exfoliated samples.

Figure 3.4 shows the circular dichroism of the $NbSe_2$ electronic bands for two different photon energies. The dichroism is strong especially at 55 eV photon energy where the effect is already visible comparing the ARPES spectra acquired with the two circular polarisations. The CD signal resulting for hν=70 eV is less apparent in the photoemitted intensity although the final dichroism is quite large too. For both both photon energies the Γ(k_x=0) axis present null CD signal. This can be accounted for by considering the experimental geometry reported in the cartoons of Figure 3.4. [90, 113] In general, null CD signal is expected for those configurations were a symmetry operation leaves the photoelectron **k** vector unaffected and flips the circular polarisation helicity. First consider the

case the electron is ejected along the surface normal as shown in the figure. By considering the mirror operation in respect to the green plane it is clear that the **k** vector remains unaffected while the polarisation is transformed from CR to CL. As a result the CD must be zero for the $(k_x,k_y)=(0,0)$ point. This argument can be generalised to coplanar photoelectrons and impinging photon beam (i.e. to the whole green plane) provided that it coincides with a symmetry inversion axis of the crystal. In this case $k_y=0$ constitutes a nodal plane for the CD. When the photon and the momentum of the emitted electrons are non-coplanar, the experimental geometry is said to have *handedness* and non-zero dichroism generally occurs. In our geometry, the analyser slit is placed vertically to the nodal plane discussed above (it is represented by the yellow vertical rectangle in Figure 3.4). The K'-Γ-K direction is aligned to the analyser slit. The Γ-M high symmetry direction thus lies in the green plane and origins the nodal plane also detected in the CD spectra of Figure 3.4. The strong CD observed for the

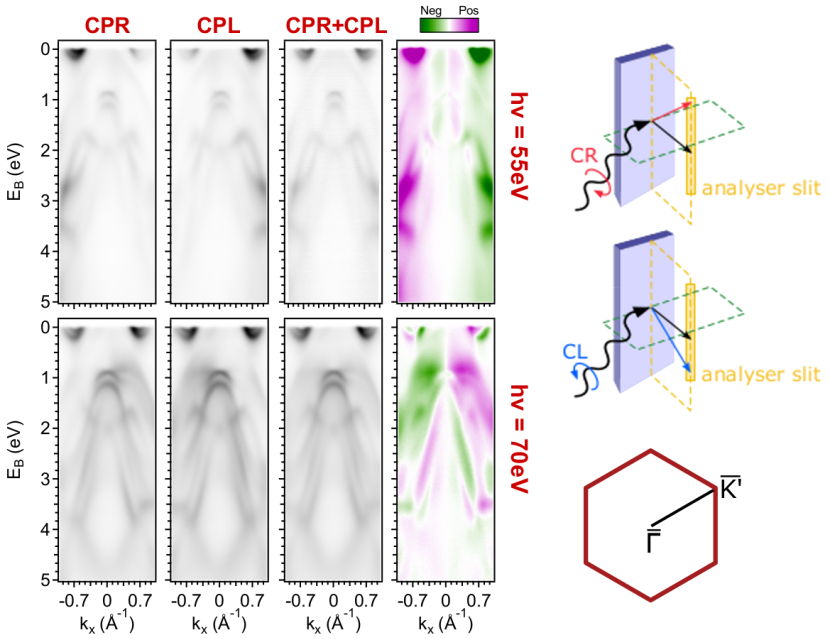

Figure 3.4: Circular dichroism ARPES of the $NbSe_2$ valence bands measured along K'-Γ-K at different photon energies (hν=55 eV (top row) and hν=70 eV (bottom row). The cartoons report the experimental geometry and the BZ direction probed with CD-ARPES

pockets is consistent with the so called *spin-valley locking* observed by photoluminescence [99, 100] and pump-probe experiments [101]. A recent theoretical study attribute the origin of the observed dichroism to the local chirality of the valley placed at inequivalent K and K' points. [114] It may also reflect the point group symmetries within the layer, as recently shown by a 2-photon photoemission experiment combined with one-step calculation study on the TSS of Bi_2Se_3. [115] However, the observed CD may contain also the chirality induced by the experimental geometry itself. The two experimental geometries reported in the cartoons of Figure 3.4 are linked throughout a reflection operation with respect to the horizontal green plane. Such operation will either reverse the photon helicity or change the photoelectron momenta. As a consequence, opposite sign of the CD is always detect for opposite emission angles in this geometry irrespective to the initial state symmetry. Further geometrical effects have been reported for initial state wavefunction spatially confined along the z-axis. Ishida and co-workers report large dichroism in $SrTiO_3$ and Cu-doped Bi_2Se_3. Furthermore, they report the existence of a second nodal plane, which is seen as signature of the 2D-nature of the electronic states investigated and orthogonal to the one defined by the coplanar geometry. [113] However, although the electronic wavefunctions are mainly localised within the layers, this additional nodal plane was not detected in the study presented here (it coincides with the direction where the measures here presented were performed). This result may suggest that the observed dichroism can not be merely described as due to a pure experimental geometric effect. Moreover, the geometrical induced CD is expected to increase monotonically with the $\mathbf{k}$ momentum [81, 83]. Thus, geometric chirality alone can not take into account the data acquired at 70 eV photon energy where the CD dependence on the momentum is more complex. In particular, the CD is strong also for bands near the Γpoint, i.e. where the spin-orbit coupling is expected to be small. This fact is not surprising as the existence of strong dichroic signal in system characterised by weak SOC such as graphite πbands [116] and Cu(111) Schockley state [22, 88]. In particular, the one-step calculations reported in [22] indicate the strong dichroic effect arise when the final state possesses d-character, which is consistent with our data. As previously discussed, Se $4p_z$-derived bands have quite strong photoemitted intensity at $h\nu$=70 eV and the transition towards d-like final state (rather than s-type) is generally favourite in the photon range used in this study. Finally a significant dependence of the CD upon the excitation energy is also observed. This feature is quite

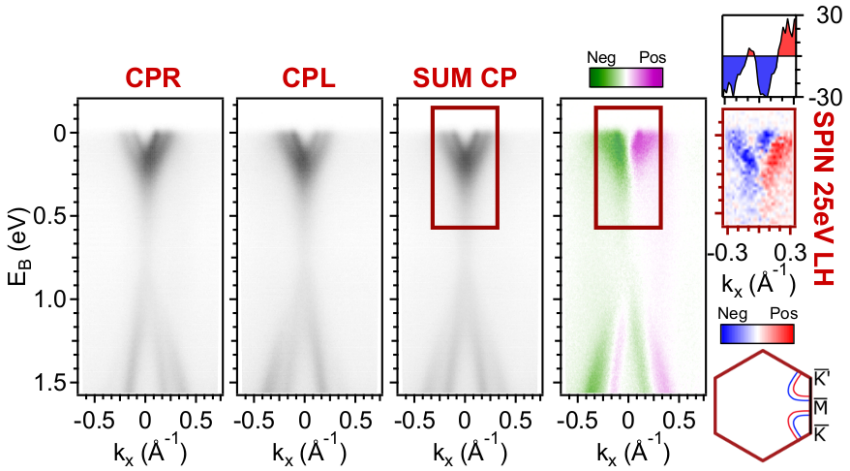

Figure 3.5: CD-ARPES investigation of the spin polarised pockets. The data were acquired at hν=25 eV along the Γ-M direction as also sketched by the BZ cartoon. For direct comparison the spin-ARPES data for the out of plane spin component are also reported as measured along the same direction with 25 eV linearly polarised light.

usual in CD spectra and as been reported on several system as topological insulators [61, 89–91, 117] and Rashba state in BiTeI [92, 93] and other BiTeX related compounds [92]. The origin of these effects is still discussed and it has been proposed to arise either from final state effects [90, 117] or driven by the initial-state [61, 89, 118]. Overall, these results strongly indicate that the proposal of Wang et al.[82] of directly infer the spin information from CD data is not applicable. Moreover, clear interpretation of the dichroic signal strongly requires to be accompanied by as detailed as possible models as also highlighted by other works [91, 92].

These observations become even more cogent when the full power of our VESPA setup are exploited and the photoelectron spin is directly measured. Figure 3.5 compares the CD-ARPES signal measured along the K'-M-K high symmetry direction and hν=25 eV with the spin-ARPES data acquired at the same photon energy and LH polarisation. At this photon energy the sampled k_z is approximately the Γ-K-M plane. Along K-M-K' BZ direction there are four dispersive states crossing the Fermi level as shown both by ARPES data and from the total intensity (SUM CP). These states correspond to the concentric trigonally warped pockets centred at K and K' inequivalent points. As for the previous case the

dichroic signal presents apparent left-to-right asymmetry already visible in the ARPES intensity spectra. This gives rise to sign reversal of the CD across the M point. The zero CD intensity occurring at the M point is a further evidence of the nodal plane discussed above. However, the CD spectra significantly differs both from the expected spin polarisation of the initial state and from the measured spin resolved signal. As the spin polarisation of the out of plane component at the M point is zero as spin-degeneracy is imposed by the time reversal symmetry (M is a TRIM point). A the k_x spans from the negative values (e.g. K) towards the positive values (e.g. K'), the measured spin polarisation undergoes four sign reversals. It starts from a negative value (blue) for the bands crossing E_F at $k_x \sim -0.3\,\text{Å}^{-1}$, which corresponds to the inner Fermi surface contour around the K point. The spin polarisation signal changes the sign (red) as k_x reaches the sharp state corresponding to the outer trigonal band that circles the K point, then it reaches zero at the M point. For positive k_x, the time reversal symmetry and the lattice three-fold rotational symmetry around the c-axis impose the reverse trend to the spin polarisation, i.e. negative(positive) for the outer(inner) band around the K' point. The quite small signal measured for the outer band around K is probably ascribable to background issues. Notably, the measured spin are consistent with the spin-valley locking texture expected for this material and already reported in literature. [98, 102] On the other hand, the CD-ARPES is negative (positive) for negative (positive) values of k_x respectively. This particular dependence resembles the one observed by Kim et al. in CD photoemission experiments on Cu(111) and Au(111) surface state. [88] In that paper the authors identify the OAM as the key driving force affecting the CD signal. To retrieve the spin information they need to compare the CD-ARPES data with an *ad-hoc* developed effective Hamiltonian, concluding that circular dichroism in ARPES is useful tool to investigate the presence and the texture of the initial states OAM.[88, 118] A different interpretation of the CD is given by Sácnhez-Barriga and co-workers, who directly compared the circular dichroic signal to the measured spin-ARPES texture of the Bi_2Se_3 topological surface states at various photon energies. In their work a strong dependence of the CD-ARPES on the photon energy is reported showing several sign reversal. Conversely, no sign reversal was reported for the spin resolved data in the energy range typical for conventional ARPES.[94] From these observations the authors concluded that the CD-ARPES is mainly affected by the d-like final-state, while the spin of the photoelectron is left unaffected. Figure 3.6 report

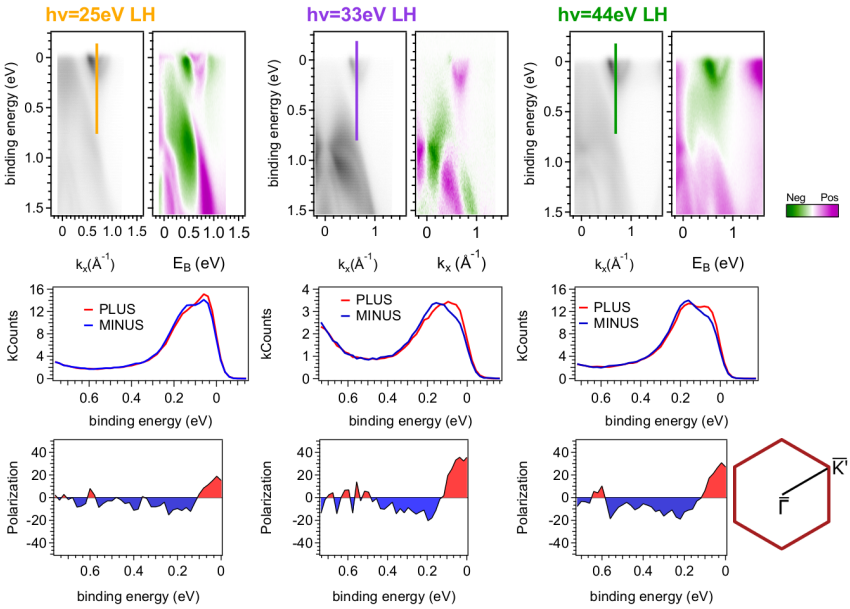

Figure 3.6: ARPES, CD-ARPES and spin-ARPES measured along the Γ-K' direction of $NbSe_2$ at different photon energies (namely 25 eV, 33 eV and 44 eV. The ARPES and spin-ARPES data were measured with linearly horizontal polarised light. The coloured lines on the ARPES spectra mark the k_x momenta where the spin texture has been probed. Top row present the ARPES and CD-ARPES spectra, middle panels report the raw spin filtered EDCs for the each photon energy. Bottom row show the corresponding spin polarisation values.

the direct comparison between the CD-ARPES and the out of plane spin component data of $NbSe_2$ at different photon energies. The data were measured along the Γ-K' direction in the BZ and LH polarisation for both ARPES and spin-ARPES. The selected photon energies were hν=25 eV, hν=33 eV and hν=44 eV. The last one correspond to k_z close to the BZ edge (i.e. the A-L-H plane). The other two energies sample the BZ close to its centre (k_z~Γ-M-K plane), however their ARPES intensity testifies a different response to the excitation energy as reported in Figure 3.3. It is therefore worthwhile to probe the sample with both these excitation energies as it has been reported that modulations in the ARPES photoemission intensity may be associated with strong changes in the detected spin through linear dichroism effects.[62, 71] Consistently with the data previously discussed, the CD signal displays strong changes at the differ-

ent photon energies. In particular, the dichroic intensity relative to the spin polarised Fermi bands undergoes a sign reversal between 33 eV and 44 eV photon energies. Conversely, the spin resolved out of plane component prove to be more robust, i.e. less affected, with respect to the changes in the matrix elements. As shown by the raw Energy Distribution Curves (EDCs) (*middle row*) and by the respective spin polarisation P_z in the *bottom row* of Figure 3.6, no sign reversal in the spin-ARPES dataset has been detected for the investigated energies. The result is consistent with the work reported in reference [94] and further demonstrates the impossibility to straightforwardly infer the spin properties of the materials by means of circular dichroism. However, closer inspection to the spin-ARPES results evidences that the degree of the spin polarisation varies upon the different photon energies. The spin polarisation value at the Fermi level is ~18 %, ~35 % and ~28 % for $h\nu$=25 eV, $h\nu$=33 eV and $h\nu$=44 eV excitation energies, respectively. To attribute these variation to k_z dependence of the spin texture is unlikely as the first two photon energies probe the same portion of the BZ. This indicates that the spin of the photocurrent is somehow affected during the interaction. Zhu et al. [62] reported oscillations as a function of the photon energy for the spin polarisation of the Bi_2Se_3 topological surface state. In their work they propose a phenomenological and general layer-dependent model to account for observed modulation of the spin polarisation. In this picture the effects of the final states are mostly ruled out by means of the plane-wave approximation and the main influence is derived by the detailed description of the initial state. The photocurrent generated by distinct layers is weighted by different phases defined by the energy-dependent probing depths. The detected spin polarisation is then qualitatively described as the results of the interference between the photoemission channels associated to the different layers. The key ingredient of this model interpretation is the layered dependent distribution of the initial spin texture. [62] It is licit to apply the same approach to our case given the strongly layer-localised electronic distribution and the consequent spin-layer locking of $NbSe_2$. [64, 102] These features are typical in the TMDC systems and the model of Zhu and co-workers has been successfully employed in the analysis of the related system WSe_2. [63] Following the method proposed by Zhu and collaborators [62] the spin-polarised photocurrent has been

calculated from:

$$I^{\sigma} = \left| \sum_{i=1,2} c_i^{\sigma} m_i \right|^2 \tag{3.1}$$

where i spans on the layer and σindicate the spin polarisation (up or down). The valence bands near the K point were described adopting the coefficients and the $d_{x^2\text{-}y^2,xy}$ orbital mixing from Riley et al. work on WSe_2. [63] Assuming a free-electron final state the i-th channel m_i of the total matrix element becomes:

$$m_i = e^{-ik_z z_i} e^{-z_i/(2\lambda cos\theta)} \langle e^{i\mathbf{k}_{\parallel}|\cdot\mathbf{r}_{\parallel}|} | \mathbf{A} \cdot \mathbf{p} | \phi_i \rangle \tag{3.2}$$

The explicit expression reported in Equation 3.2 states that the phase depends both on the photon energy (through k_z) and on the layer z_i. Figure 3.7 shows the oscillatory behaviour of the spin photocurrent predicted by this model together with the spin polarisation at the Fermi level extracted from the data reported in Figure 3.6. The results are not conclusive, although the experimental trend may be qualitatively consistent with the picture proposed in the literature. [62, 63] However, additional and denser photon energy steps (up to 60 eV at least) need to be investigated to really verify the oscillatory behaviour of the photocurrent. Moreover, the experimental degree of spin polarisation is systematically less than the one expected by the phenomenological model. This may arise from experimental errors, such as that the signal contains the contribution of two adjacent grains 180° rotated. Another possibility comes from the experimental geometry. As a matter of fact, the model rules out both polarisation effects and photon incident angles whose capability to affect the spin-resolved results have been reported before and cannot be overlooked. [62, 71–73] Day and co-workers recently released an open source software package (*chinook*) designed to predict the ARPES intensity modulations as a function of the experimental geometry and the detailed description of the initial state.[119] The software simulates the effects on the photocurrent induced by an arbitrary experimental geometry (the photon energy/polarisation, the incidence angle etc.), concurrently providing a careful description of the initial wavefunctions, ranging from orbital character, spin texture surface-vacuum interface effects. Overall, *chinook* provide a powerful framework to deepen the understanding of the matrix element effects, giving further insights on the electronic structure of materials. Finally, effects originated from the non-spheric final state distribution may also play a role in the process.[22, 90, 94] Overall, a full

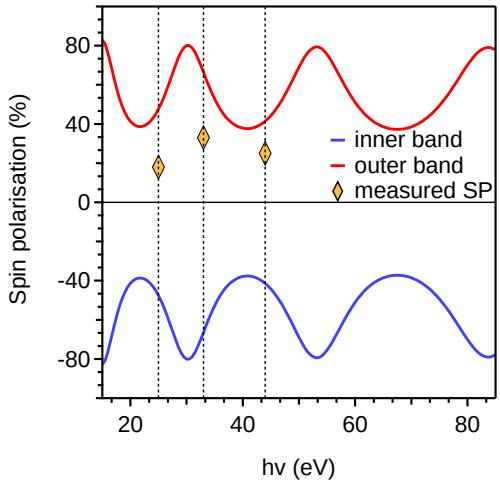

Figure 3.7: Red and blue lines represent the oscillations of the spin photocurrent for the two concentric Fermi contours as calculated by the model sketched above. The orange diamonds mark the values of the measured spin polarisation at the Fermi level estimated from the data presented in Figure 3.6.

description of the photoemission interaction may be necessary to quantitatively describe the photoemission process.

Figure 3.8 reports the spin-resolved ARPES spectra measured along Γ-K at hν=25 eV as a function of the light polarisation (LH, CR and CL). For direct comparison, the circular dichroic signal is also reported. Again, the spin-integrated circular dichroism overall differs from the spin-polarised data. In particular, the CD is mostly positive in the area corresponding to the spin-resolved investigation, whilst the opposite spin polarisation of the two bands are clearly observed in the spin-ARPES spectra. Moreover, the spin filtered data probed of the Fermi bands circulating K and K' points are robust with respect to the changes introduced by polarisation handedness in the matrix elements, at least for this photon energy. These results seems contradictory to the work performed by Razzoli et al. on the MoS_2 TMDC[72], where the authors report strong dependence of the spin-ARPES data on the light helicity. However, the discrepancy may originate from the different experimental conditions used. For example, the photon energies investigated in the paper are different from the one shown in Figure 3.8 as well as the geometric configurations may be inequivalent. A useful contribution is offered by the study of Miyamoto and coworkers [73],

that also reported variations in the 3D spin polarisation as a function of the photon handedness for the Rashba Dirac-like surface state of W(110). In their work it is also shown that one component is robust against the polarisation helicity. They demonstrate that the unaffected spin component arises from orbitals whose symmetry allows only photoemission when excited with LH polarised light. As the light polarisation can be decomposed in a coherent superposition of LH and LV polarisations, it means that no phase difference (i.e. interference effects) can be introduced by the circular polarisation handedness.[73] This picture suggests that the orbitals linked to the spin texture can be probed only by the LH polarised light, at least in the present experimental geometry. This hypothesis is corroborated by the spin-polarised data acquired at the same energy with the linear vertical polarised light. As reported in Figure 3.9, the photocurrent show null out-of-plane spin polarisation when probed with LV light. Moreover, significant differences are also visible in the spin-integrated ARPES spectra. In particular, the photoemitted intensity of two bands under investigation becomes more symmetric when probed with LV polarised light in respect to LH. This observation is consistent with the interpretation proposed by Miyamoto et al. [73] and hints linear dichroic effects may play an important role in the of the spin photocurrent. [62, 71]

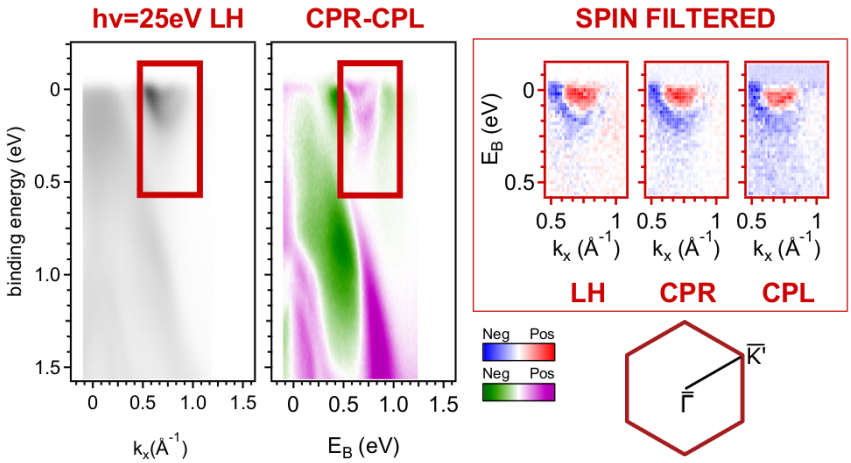

Figure 3.8: ARPES data measured along the Γ-K direction with 25 eV linearly horizontal polarised light. The green-purple image reports the intensity of the circular dichroism at the same photon energy. The spin-ARPES results obtained with different light polarisations (namely LH, CR and CL) are reported in blue-red scale. The red rectangle on both the ARPES and the CD-ARPES spectra marks the area where the spin-resolved texture was probed.

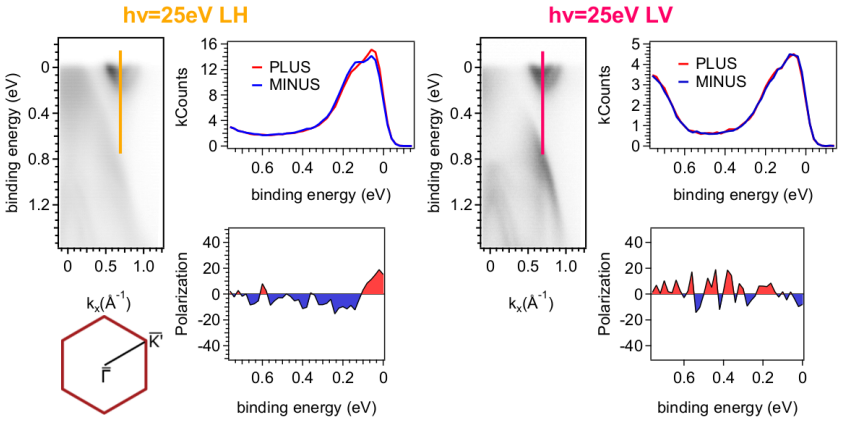

Figure 3.9: spin-ARPES results obtained at hν=25 eV for both the linearly polarised lights.

3.4. Conclusions & future outlook

This chapter investigated the role of the transition matrix element in determining the probed spectral function. The out-of-plane spin polarised Fermi surface of $NbSe_2$ have been chosen as a case study. Strong dichroic signal has been observed throughout the valence band of UHV exfoliated bulk $NbSe_2$ samples. The dichroism is strongly affected by the matrix element variation introduced by the photon light. Significant evolution up to sign reversal is reported when the photon energy is varied in the energy range typical of conventional ARPES (i.e. from 25 eV to 70 eV). The results are consistent with the interpretation of strong final state dependence of the photoemitted intensity on the light polarisation handedness. Conversely, the spin-filtered photocurrent experience minor variations as a function of the photon energy. The robustness of the spin-ARPES signal upon the circular light handedness is interpreted by means of coherent superposition of LH and LV polarisations combined with orbital symmetry arguments. Overall, the results here reported prove that the simplistic interpretations of the dichroic signal in angular distribution as a tool to infer the spin properties o the initial state is unjustified. The main reason for that appears to be the preponderant influence of the final state. The reliability observed in the spin-resolved ARPES data confirm that the direct measure of the spin is the technique of choice to assess the spin texture of the initial state, although the absolute values of SP are to some degree affected by matrix elements too.

To improve the understanding of the interaction matrix element and the quantitative analysis of the spin, linear orbital dichroism in combination with experimental geometry (e.g. light incidence angle, different sample alignment) is a must. Further interpretations of the spin-ARPES data by means of models presented in ref.[62, 72, 73] are scheduled together with tight binding calculations. In the pursue of these objectives, the new open source framework *chinook* offered by the very recent work of Day and co-authors [119] constitutes a promising and powerful tool to access the information encoded in the photoemission matrix element. Finally, comprehensive picture of the whole interaction, including as detailed as possible description of the wave functions involved in the photoemission process, is necessary to extract both the spin and the orbital textures of the initial states.

4. Direct insight into the electronic properties of $SrNbO_3$

> Well, research is like visiting a zoo. You wanted to see the white tiger, but you end up with several unknown birds.
>
> Dr. P. K. Das 2018

4.1. A new material for catalysis

Perovskites define through their structure a class of transition metal oxides (TMO) that are extensively investigated. The reason of this interest lies in their unconventional properties (e.g colossal magnetoresistance, ferroelectricity, superconductivity), which bear an obvious potential impact on technology [120, 121]. Perovskites are described by the chemical formula ABO_3, where A is a trivalent rare-earth ion or a divalent alkali-earth

ion and B is a transition metal (TM) element, octahedrally coordinated with 6 first-neighbour oxygen. The ions are arranged in a cubic lattice. However, distortions induced by the O-TM-O bondings may affected the structure and lower the symmetry.

In this class of materials the Nb-based $SrNbO_3$ system has recently raised interest for its potential of photo-catalytic activity driven by visible light.[122] $SrNbO_3$ belongs to the nominal $4d^1$ perovskites, which has been less investigated than the $3d^1$ counterpart. The 4d systems are expected to differ with respect to the equivalent 3d-based TMO. The wider extension of the 4d electronic states determines strongly hybridisation with the neighbouring oxygen ions and reduces the on-site Coulomb interaction. As a result, a more pronounced metallic behaviour (i.e. electrical conductivity) corresponds to the reduced electron-correlation effects. However, published works investigating the 4d-based perovskites and the ferromagnetic order observed in the 4d-ruthenate systems hint that correlation effects are not negligible in this class of materials too. [123–125]

$SrNbO_3$ structure presents slight distortion (i.e. ~10°) of the O-TM-O bonds that reduces the cubic symmetry to orhtorombic, with 20 atoms per unit volume. [126] *Panel a* of Figure 4.1 reports the unit cell. The Nb-O bond lengths are very similar (i.e. the maximum deviation is smaller than 0.02Å). Moreover, growing the $SrNbO_3$ on suitable substrates can stabilise the cubic structure of the samples. Hereafter the pseudocubic perovskite structure sketched in *panel b* is assumed for $SrNbO_3$.

After the photocatalytic properties of $Sr_{1-x}NbO_3$ (with $0.03 < x < 0.20$) polycrystals and thin films were reported by Xu and collaborators [122], intense theoretical efforts were made to understand the electronic properties of $SrNbO_3$. Zhu *et al.* extensively investigated the photocatalytic performance and reported a detailed band structure as obtained from conventional density functional theory and GW calculations.[127] The elastic properties as well as the electronic structure of $Sr_{1-x}NbO_3$ have been reported by Xu and co-workers.[128] Sun *et al.* investigated the effects of defects in the $SrNbO_3$ structure and suggested the occurrence of a ferromagnetic ordered phase when driven by Sr vacancies [129] Fewer experimental studies are available with respect to the rich theoretical literature. Oka and co-workers grew $SrNbO_3/KTaO_3$ thin films at different temperatures and investigated the resulting stoichiometries. [130] They reported metallic conductivity comparable with those of $SrVO_3$ and $SrMoO_3$ and colcuded that correlations have a significant role in the electrical conduction of $SrNbO_3$. Two recent works from Venkate-

san's group [131, 132] investigated the optical response of $SrNbO_3$ thin films. They claim that visible-light photo-catalytic properties are driven by plasmon-based resonances. This model has been corroborated by theoretical calculations. [133] X-ray/UV electron spectroscopy studied are very scarce. Standard XPS was reported by Isawa and co-workers [134] on polycristalline $Sr_{1-x}NbO_3$ samples and Miruszewski *et al.* investigated Nb-doped $SrNb_xV_1-xO_3$. [135] Angle-Resolved PhotoElectron Spectroscopy (ARPES) measurements reported in literature on Nb-based oxides are limited to the Ruddlesden-Popper series. The layered structure changes the orbital arrangement and is reflected in the electronic properties of the system. In particular, ARPES studies are reported for the quasi-1D metallic $SrNbO_{3.4}$ and the ferroelectric insulator $SrNbO_{3.5}$.[136–139] X-ray absorption studies were published on the NbO, NbO_2 Nb_2O_5. [140] Few works investigated $SrNbO_3$ · $_4$ Nb-carbides catalysts [140, 141] and Li-Nb based oxide superlattices. [142]

The aim of this chapter of the thesis was to perform an extensive investigation on the electronic structure of $SrNbO_3$ by exploiting advanced spectroscopic techniques.

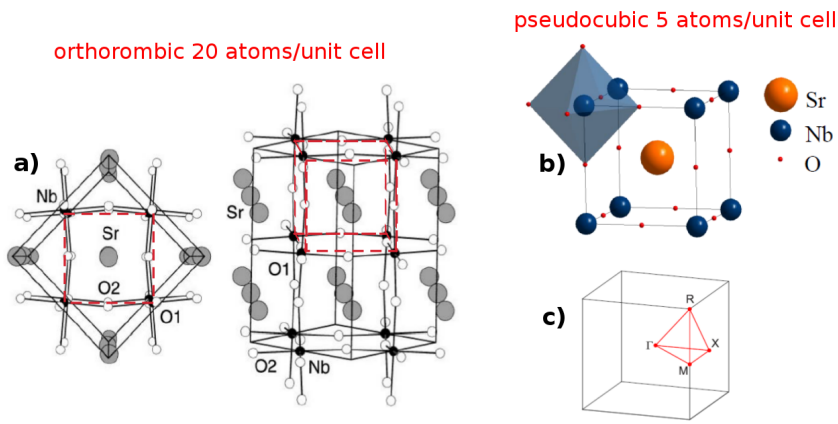

Figure 4.1: a) $SrNbO_3$ orthorombic crystal structure, the dashed red line indicates the respective pseudocubic cell (adapted from ref. [126]) b) pseudocubic perovskite structure and (c) the respective Brillouin zone (BZ)

4.2. Results

To perform this study, high quality $SrNbO_3$ thin films were grown on suitable substrates by means of Pulsed Laser Deposition (PLD) in ultra-high vacuum environment. *In-situ* and *ex-situ* structural characterization was carried out and proved the good quality of the films. The electronic states of the pristine samples were investigated by means of VUV and X-ray electron spectroscopies exploiting two variable polarisation undulator source at the APE beamline were performed on the as-grown, *in-situ* transferred films. X-ray absorption and photoemission spectroscopies (XAS and XPS) were used to characterise the chemical composition and ionic states of the TM and O atoms in the samples and their dependence upon the growth conditions, namely the oxygen background pressure. An extensive campaign of angle-resolved photoemission spectroscopy (ARPES) measurements has been performed on the best optimised $SrNbO_3$ thin film samples. The ARPES results were analysed and compared with Density Functional Theory (DFT) bulk calculations.

4.2.1. Material growth and characterisation

$SrNbO_3$ thin films were deposited in the PLD growth chamber under an ultra-pure (i.e. 99.9999%) oxygen pressure. A stoichiometric polycrystalline $SrNbO_3$ target was ablated by ~10 ns focused laser pulses with energy density ~2 J cm^{-2}, the repetition rate was varied from 3 Hz to 1 Hz. Samples were grown on several different substrates: $DyScO_3$ (110), $KTaO_3$(001) and $NdScO_3$(110). The growth temperature was set at 700 °C, which has been reported to give the optimum stoichiometric 1:1:3 ration. [130] The background pressure of oxygen was varied for different growth sessions from 0.1 mbar to 10^{-4} mbar.

The crystallographic properties of the samples were probed by means of *ex-situ* XRD. Figure 4.2 reports the X-ray diffraction patterns for the (002) and (004) symmetric lines of $SrNbO_3$ deposited on the three substrates used. Regardless of the substrate, no traces of spurious phases were detected. The films present only (00l) diffraction peaks, indicating the preferential c-axis orientation of the samples along the normal direction to the substrate surface. Fine inspection show the film grown on $DyScO_3$ (orange curve) has the out of plane lattice parameter slightly larger than the bulk value, which is consistent with the in-plane compressive strain imposed to the film by this substrate. The in-plane lattice constant of

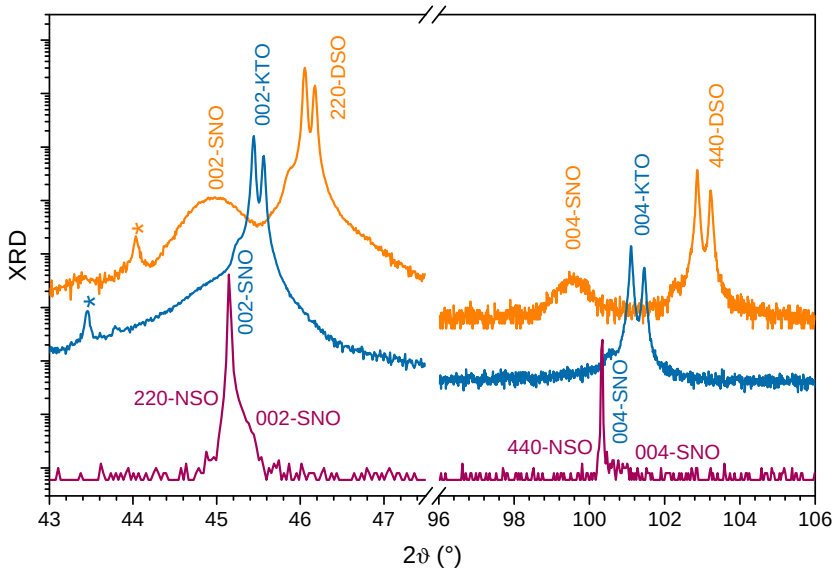

Figure 4.2: X-ray diffraction patterns around the (002) and (004) Bragg diffraction lines of the $SrNbO_3$ films grown on the different substrates: $DyScO_3$ (orange) $KTaO_3$ (blu) and $NdScO_3$ (red-purple). Due to the very small lattice mismatch between $SrNbO_3$, $KTaO_3$ and $NdScO_3$ the film peaks are hidden by the substrate's signal in these cases.

the film shrinks to adapt to the substrate periodicity 3.95 Å, while the c-axis expands up to 4.04 Å, exceeding the expected bulk value (4.02 Å). On the other hand, the very small mismatch between the film and both the $KTaO_3$ (4.00 Å) and the $NdScO_3$ (4.04 Å) results in negligible strain applied to the thin films. In this case the film's and the substrates' diffraction peaks largely overlap and the signal from the film is hidden by the more intense substrate's peak. To further confirm the strain of the grown samples Figure 4.3 reports the in-plane reciprocal space maps measured for films deposited on (a) $KTaO_3$ and (b) $DyScO_3$. The Q_x axis gives the in-plane lattice constant, while Q_y reflects the out of plane lattice parameter. The (003) symmetric diffraction peak of the film almost coincides with the $KTaO_3$ substrate, as expected for the very close lattice constants. The map was acquired by using high-resolution mode to better estimate the lattice parameter of the film. The analysis gave 4 Å value, which is very close to the expected bulk-like 4.02 Å. In case of $DyScO_3$ substrate,

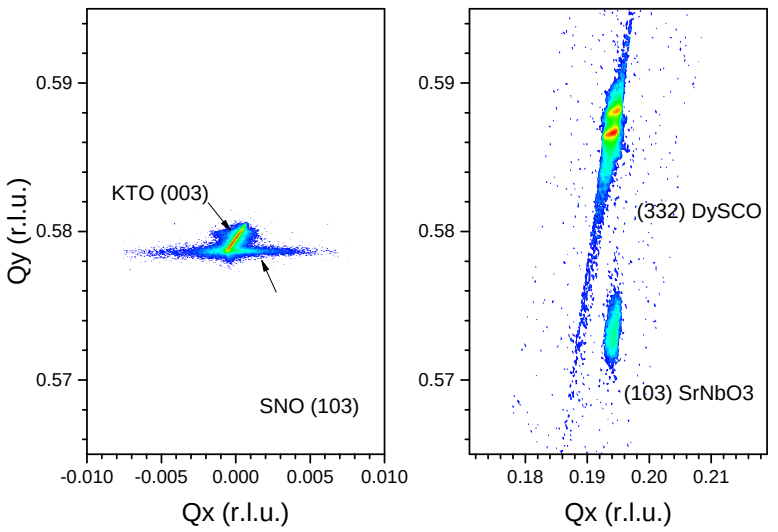

Figure 4.3: In-plane diffraction maps (a) $SrNbO_3$ (003) symmetric diffraction map shows a non-strained sample on $KTaO_3$ substrate (b) (103) asymmetric map indicate a fully strained $SrNbO_3$ film grown on $DyScO_3$. The axis indicate the peak position in the reciprocal space for the in-plane (Q_x) and the out of plane (Q_y) in relative lattice unit.

the reciprocal space map was recorded around the $SrNbO_3$ asymmetric (103) Bragg peak. As already detected from the symmetric diffraction scans reported in Figure 4.2, the peaks of the substrate and the film are well separated. Nevertheless, they are perfectly aligned along the Q_x axis, indicating the full in-plane matching of the film and substrates lattice parameters, with no trace of film relaxation. These results prove that the films grow as "fully strained" on $DyScO_3$, i.e. maintain the interfacial strain for the entire thickness. Figure 4.4 shows XRD measurements for $SrNbO_3$ thin films deposited at different oxygen pressure on $DyScO_3$. This substrate was chosen because of the complete separation between its own diffraction peaks and the those of the overlayer. This condition allowed to use the high-intensity XRD configuration for better estimation of the c-axis of the differently grown samples. The *top panel* shows the shift towards smaller angles of the (002) $SrNbO_3$ Bragg reflection, i.e. the film's out-of-plane lattice parameter slightly increases as the growth pressure is lower. The *bottom panel* reports the calculated values of the out-of-plane

lattice parameters as a function the O_2 background pressure. The c-axis constant increased from 4.02 Å to 4.09 Å as the pressure was reduced from 0.1 mbar to 10^{-4} mbar (the red straight line was superimposed to the data as a guide to the eye). This phenomenology is standard for perovskite systems: it is related to the relative amount of oxygen vacancies in the sample[143]. The reduction of the highly electronegative oxygen atoms in the film induces an expansion of the sample structure, which manifests itself as a shift towards lower diffraction angles in the XRD patterns. Concurrently, the presence of oxygen vacancies determines a higher density of free electrons in the system, favouring the metallicity of the sample. Thus, the fine tuning of the oxygen background growth pressure allows to influence the concentration of oxygen defects and consequently the degree of metallicity of the as-grown $SrNbO_3$ films. Energy Dispersive Spectroscopy (EDS) confirmed that the Sr:Nb ratio was not affected by the O_2 background growth pressure. The fine structure of the films was also carried out by *ex-situ* High-Resolution Transmission Electron Microscopy (HRTEM). Figure 4.5 shows the HRTEM image of a $SrNbO_3$ thin film deposited on $DyScO_3$. The interface with the substrate appears atomically sharp and the film displays a unique crystallographic phase. Contrast variations in the HRTEM of this film are ascribed to the sample preparation (cross-section thinning). The Fast Fourier Transform (FFT) analysis of the HRTEM results is shown in the red insect of Figure 4.5. The absence of any extra peak excludes the presence of secondary orientations. The position of the peaks is fully consistent with the cubic perovskite-like structure of the films fabricated by the procedure described in this work. The FFT of the orthorhombic substrate is also reported (green insect) of Figure 4.5.

Once the detailed growth protocol leading to the desired crystalline quality and orientation was acquired, the issue of surface structural homogeneity was addressed. The low-energy electron spectroscopies used in this work are intrinsically very surface sensitive. Hence, the sample surface must be long-range ordered to successfully study the electronic bands, at least displaying suitably large domains to be individually probed by synchrotron radiation beam (~100 µm lateral spot size). The surface roughness must therefore be controlled and kept to a minimum. The PLD technique allows to pursue these stringent requirements by careful tuning of the growth rate. Low rates provide more time to the impinging atoms for laterally diffusing on the substrate and the overall crystalline order and the surface quality is therefore increased. To calibrate the samples' growth

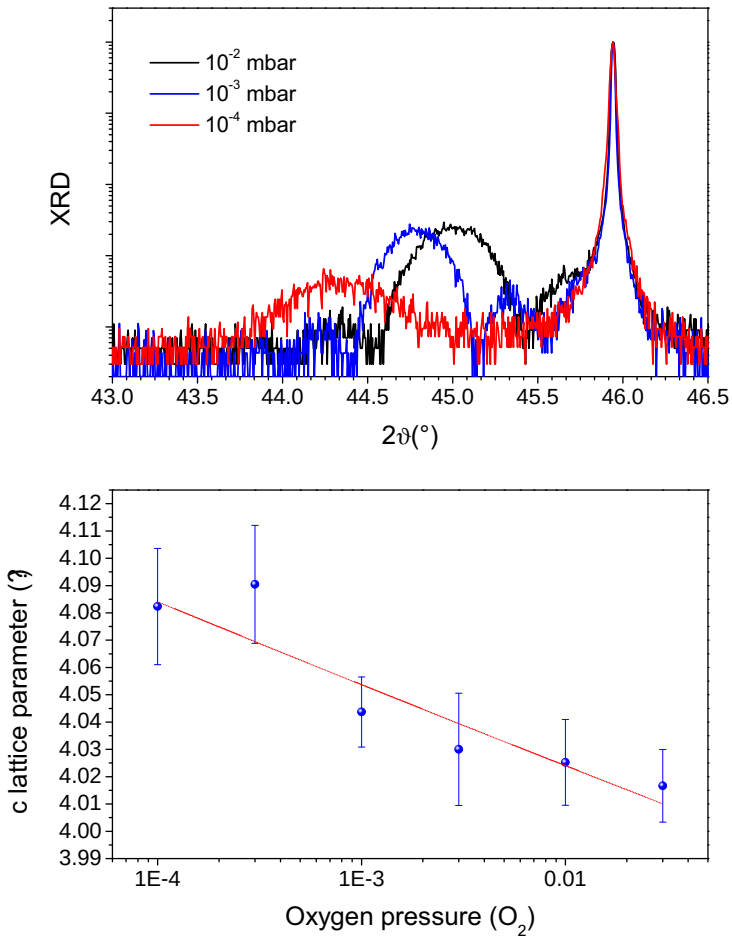

Figure 4.4: Effect of the background pressures on the amount of oxygen vacancies in the sample. *Top panel* X-Ray diffraction patterns of $SrNbO_3$ (002) diffraction line for thin films deposited with different oxygen background pressures. *Bottom panel* c-axis lattice parameter as a function of the growth background pressure, the straight red line is reported as a guide to the eye.

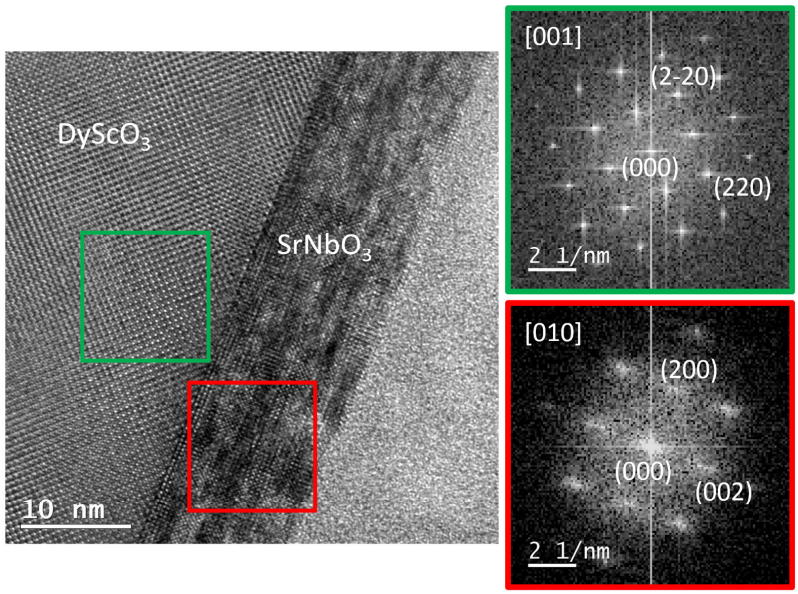

Figure 4.5: HRTEM image of $SrNbO_3/DyScO_3$ sample. The insects reports the FFT of the substrate (green) and the film (red) respectively. Coloured frames on the HRTEM image indicate the regions where the FFT were calculated

rate and to monitor the surface roughness *ex-situ* low-angle X-ray reflectivity (XRR) measurements were performed. Figure 4.6 shows the XRR curve of $SrNbO_3$ thin films grown on $DyScO_3$ and $NdScO_3$ substrates at two different target-substrate distances. Varying slightly the target-substrate distance allows to change the amount of material deposited on the substrate per each shot. Therefore, the growth rate can be tuned in a controlled way, e.g. shorter distances will correspond to higher growth rates and vice versa. As shown in Figure 4.6, the periodicity of the XRR oscillations is different for the two different target-substrate distances and thicker film (shorter oscillation period) was obtained for closer distance between the target and the substrate, as expected. It is noteworthy to note that the choice of the substrate does not affect the XRR oscillations. The thickness analysis was performed by mean of the IMD package of XOP software [144, 145] and a representative result is reported in the insect of Figure 4.6. The best fit (red curve) of the data (blue circles) was obtained in correspondence of 12.3 nm film thickness. Estimated growth rate was ~39/50 laser shots per unit cell, (i.e. $0.11\,\mathrm{nm\,min^{-1}}/0.08\,\mathrm{nm\,min^{-1}}$ at

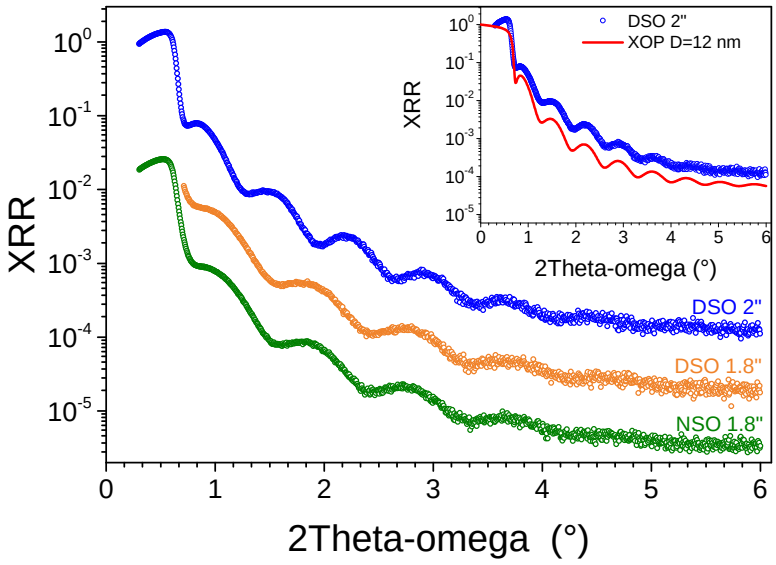

Figure 4.6: X-ray reflectivity curve of three $SrNbO_3$ films deposited on $DyScO_3$ (green and blue data) and on$NdScO_3$ (orange circles) for two different target-substrate distance. The reported distance refers to the value as read on the scale of the linear travel (higher values means shorter target-substrate distances). The inset compares the XOP reflectivity curve for a ~12.3 nm thick to the $SrNbO_3$ grown on $DyScO_3$ at distance 2".

repetition rate of 1 Hz) per the closest/furthest target substrate distance, respectively. Such a low rate allow to control the sample's thickness by adjusting the total deposition time. To avoid finite size effects to appear in the spectroscopy ~20 nm thick films were prepared with the fully refined protocol. The surface roughness extracted from the XRR data of Figure 4.6 is ~0.4 nm, which corresponds to about one single $SrNbO_3$ unit cell. However, this value is the upper limit of the surface roughness, as the oscillations above $2\Theta = 4°$-$5°$ fall below the experimental resolution of the XRD apparatus used in the present work. *In-situ* Low Energy Electron Diffraction (LEED) and Scanning Tunnelling Microscopy (STM) were also performed on freshly grown films in the UHV environment of the whole APE-suite. Figure 4.7 shows the LEED patterns of all the $SrNbO_3$ films as grown on all the substrates used in this work. Independently of the choice of the substrate, the LEED patterns confirm the long range order of the films' surface, showing the expected simple cubic structure with no

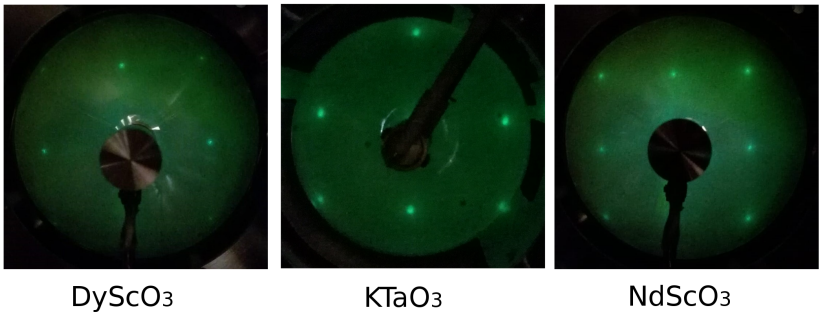

Figure 4.7: LEED patterns of ~20 nm thick $SrNbO_3$ film grown on different substrates, i.e. $DyScO_3$,$KTaO_3$and$NdScO_3$ (from left to right)

sign of surface reconstruction (i.e. absence of extra spots). These results were achieved for a large range of growth conditions, suggesting the both the perovskite structure and the layer-by-layer growth are unaffected by slight changes of oxygen content in the sample. Finally, Figure 4.8 reports the STM topography images taken with constant current mode for (a) $SrNbO_3/DyScO_3$ and (b) $SrNbO_3/KTaO_3$ samples. For the film grown on $DyScO_3$ $V_s = 2.1$ V, $I_s = 0.1$ nA and the X, Y axis were aligned to the [1-10] and the [001] substrate directions respectively. For $SrNbO_3/KTaO_3$ the sample bias voltage (V_s) and the tunnelling current (I_s) were set to -0.68 V and 0.1 nA respectively. The $KTaO_3$ [100] and [010] directions are aligned along the X and Y axis of the image, respectively. For both substrates the maximum deviation in Z height of the tip is ~1 nm. However, the topography image indicate the quality of the film grown on $KTaO_3$ is slightly better, as expected from the minor strain condition applied to the film by this substrate. The sample morphology is homogeneous over the whole area measurable at once by the STM (i.e. 200x200nm^2), which is 4 times wider than the area found for chSrNbO3/DyScO3. Moreover, the film's terraces in case of $KTaO_3$ substrate are bigger and characterised by sharp edges, mimicking the square structure of the sample surface. The roughness of the film was analysed with the WSxM software [146]. The STM analysis indicate a very smooth surface with RMS roughness < 0.2 nm, i.e. less than half of the $SrNbO_3$ unit cell. This value is the bottom limit for the film's surface roughness as it has been calculated on a very small area of the sample (i.e. 100x100 nm^2 for $DyScO_3$ and 200x200 nm^2 in the case of $KTaO_3$ substrate). Overall, the structural investigation confirmed that the samples were suitably optimised for the electronic

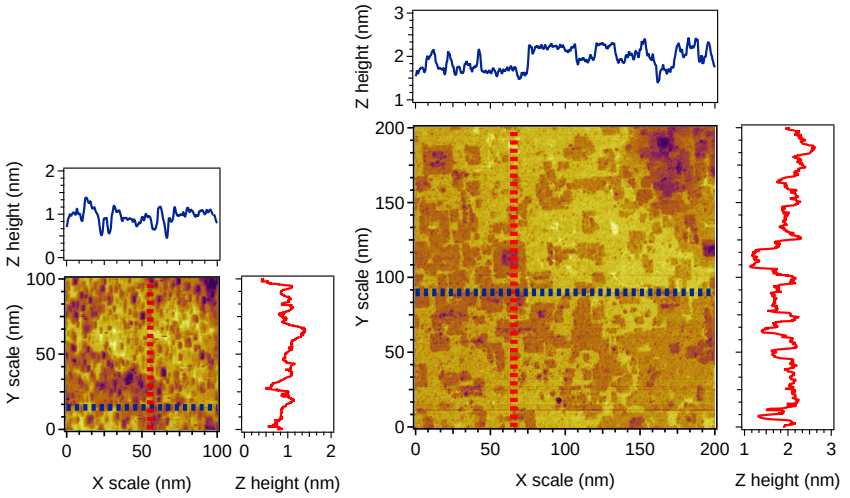

Figure 4.8: STM topography of $SrNbO_3$ grown on (a)$DyScO_3$ and (b)$KTaO_3$. Horizontal (blue) and vertical (red) profiles are also reported for both samples and coloured dotted lines on the STM image mark the position were the profiles were extracted.

properties investigation and, in particular, for ARPES experiments.

4.2.2. Electronic properties

Once the detailed growth protocol leading to the desired crystalline quality and orientation was acquired, fresh $SrNbO_3$ films were grown, and transferred under UHV conditions into the APE-suite to perform high resolution photoelectron spectroscopy with polarised synchrotron radiation. No spectral changes have been found for samples grown on different substrates, indicating the minor role of the strain applied by the substrate on the electronic properties.

To provide a reference for the ARPES, XPS and XAS experimental results we proceeded to carry out density functional theory calculations of the bulk electronic structure. The DFT computations are presented first and followed by the surface sensitive experimental results.

DFT calculations

The DFT calculations were performed using the open-access QuantumESPRESSO code [47, 147]. Perdew-Burke-Ernzerhof (PBE) [49] parametri-

sation was adopted for ultrasoft pseudopotentials from the pslibrary [148]. The choice of the ultrasoft pseudopotential was made to find a compromise between the accuracy of the calculation and its computational cost (CPU time). *Panel a* of Figure 4.9 compares the convergence test for the plane-wave (PW) basis cutoff (ecutwfc) of a norm-conserving pseudopotential (blue) and the ultrasoft PBE selected for this study (red). It clearly appears that the ultrasoft reaches a plateau faster, while the norm-conservng pseudopotential has not reached convergence at 100 Ry yet. This occurs typically in oxygen-based compounds as the strong electronegativity of oxygen tends to localise the electrons close to the nuclei. The resulting wave functions are very steep, thus a higher number of Fourier components is needed to describe accurately the electronic density of the material. To circumvent this inconvenient, the ultrasoft pseudopotentials relax the hard-core assumption for the positive ions, which is a safe choice if the simulations describe ions close to the equilibrium distance (i.e. negligible external pressure). Figure 4.9 also reports the optimisation of the PW ba-

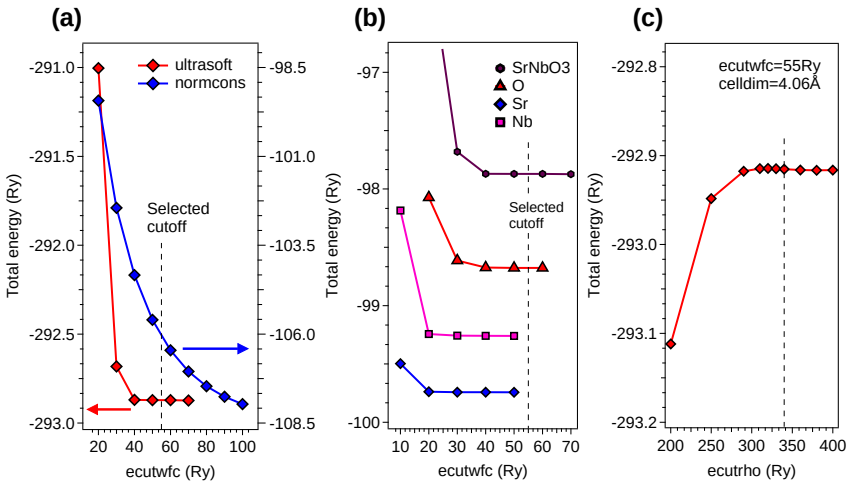

Figure 4.9: (a) Choice of the pseudopotential set. Calculated total energy vs the energy cut-off on the wavefucntion basis set for two different pseudopotentials: a norm-conserving PZ-LDA (blue curve) and an ultrasoft functional generated by PBE parametrization (red line), which converges faster. (b), (c) Convergence tests for the ultrasoft pseudopotential. (b) Choice of the cut-off on the number of plane waves basis set for $SrNbO_3$. Total energy of the single elements are also reported (c) density cut-off convergence test for the selected ecutwfc = 55 Ry

sis set. A value of 55 Ry has been selected for the energy cutoff (ecutwfc). *Panel b* reports the total energy of the system and for the individual atomic species. It is clear that fixing ecutwfc = 55 Ry the total energy has reached a plateau. This means the simulation has converged and the calculation's outputs are reliable. For ultrasoft pseudopotential the $|\Psi|^2$ no more equals the electronic density of the system and its convergence has to be verified. The results are shown in *Panel c* of Figure 4.9 and the optimum value selected is ecutrho = 340 Ry. The calculated relaxed structural parameter of the $SrNbO_3$ pseudocubic unit cell was 4.06 Å, which is not far from both the expected 4.02 Å bulk value and the experimental value of the fully strained thin films. The Monkhorst and Pack method was adopted for the Brillouine zone sampling [149], a uniform 13 x 13 x13 grid of k-points was selected for the self-consistent calculation. The grid density has been increased to 33 x 33 x 33 for the non-self-consistent calculations for the density of states (DOS) and the electronic Fermi surface physical quantities.

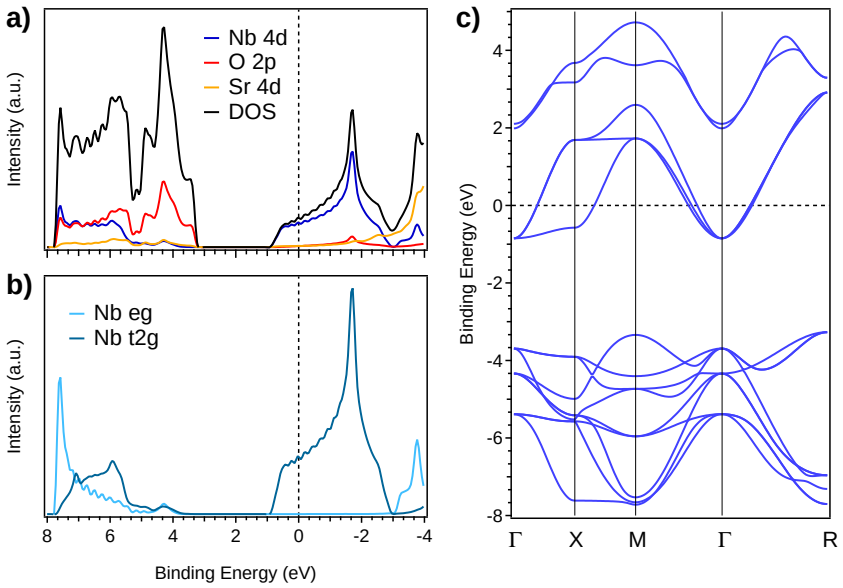

Figure 4.10: Calculated electronic properties of bulk stoichiometric $SrNbO_3$ (a) Integrated total DOS (black) and the partial DOS projected on the individual atoms. (b) DOS projected on the t_{2g} and e_g orbitals of Nb4d to emphasise the t_{2g} character of the conduction band. (c) Valence and conduction band structure along the Γ-X-M-Γ-R high-symmetry directions

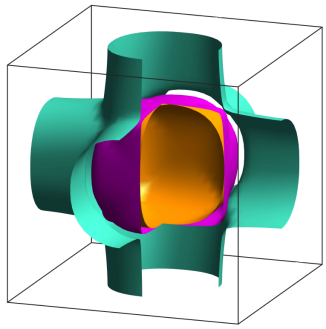

Figure 4.11: 3D view of the three calculated Fermi surface.

The results of the DTF calculations are summarised in Figure 4.10 and Figure 4.11. *Panel a* of Figure 4.10 shows the total DOS of both the valence and conduction bands, together with the partial DOS projected on the individual atoms. The computed $SrNbO_3$ bulk shows a metal behaviour with ~2.3 eV gap separation between valence and conduction bands (VB and CB). The main contributions to the valence band arise from the oxygen 2p and the Nb 4d orbitals, while the Sr 4d weight in the extended state is less important. On the other hand, the bottom of the conduction band is entirely made of Nb d electrons. Moreover the partial DOS projected on the single Nb 4d orbitals (*panel b*) indicates the conduction band is characterised by t_{2g} orbital character. This is a typical feature of 3d-based perovskites TMO [150–152] and consistent with the theoretical results reported in the literature for $SrNbO_3$. [127, 153] *Panel c* reports the band dispersion along the Γ-X-MΓ-R high-symmetry path, which are in consistency with Ref. [127]. The conduction band minimum is found at the Γpoint and its value is E_B ~0.85 eV. The valence band maxima are located in the R point (E_B ~3.27 eV) and in the M point (E_B ~3.34 eV), while the top of the valence band is ~3.69 eV in Γ. Finally, Figure 4.11 reports the 3D Fermi surface iso-energy contour, which is made up of three electronic bands. Two spherical electron pockets are centred at Γ point and the third band is formed by three interpenetrating cylinders crossing at the centre of the Brillouin zone (Γ). Overall, the here-presented DFT calculations are consistent with previous theoretical works reported in the literature for $SrNbO_3$ and for similar oxide perovskites[124, 127, 154]

XAS and XPS

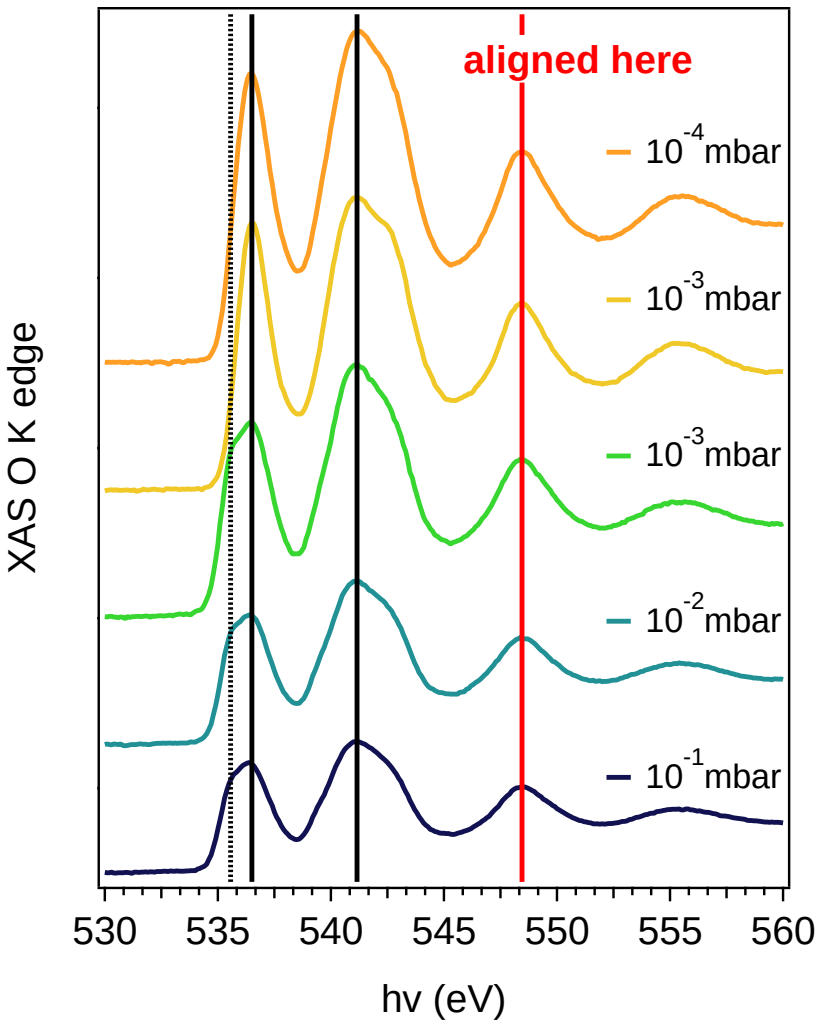

Figure 4.12: XAS spectra for O K (1s) absorption threshold measured on $SrNbO_3/DyScO_3$ samples deposited at different oxygen pressure.

X-Ray Absorption (XAS) and Photoemission (XPS) spectroscopies have been performed to study the effects of different concentration of oxygen vacancies on the $SrNbO_3$ electronic structure. Figure 4.12 shows the XAS spectra around the oxygen K-edge energy for as-grown $SrNbO_3$ films deposited on $DyScO_3$ at different O background growth pressures (i.e.

from 10^{-1} mbar to 10^{-4} mbar of pure O_2). The absolute calibration of the photon energy was not available at the time of the esperiments, thus only the relative energies of the peaks in the spectra have been considered. The O K-edge spectra were aligned on the peak centred at ~548.5 eV (marked by a red straight line on the graph). The spectra are stacked accordingly to the P_{O_2} used during the film deposition. Aside the peak at 548.5 eV, two other main structures are recognisable at about 12 eV and 7.3 eV relative energies. According to literature, the two features at higher energies are ascribable to the transition towards oxygen 2p level hybridised with Sr4d and Nb5sp states, while the one located near the edge is due to promotion of bound electrons in the empty states with O2p-Nb4d character. [140, 141] Moreover, the O K-edge spectra have been widely investigated by EELS in case of NbO (Nb^{2+}) Nb_2O_5 (Nb^{5+}), providing a first rough reference for the Nb valence ionic states. [155] The intensity ratio between the peaks is related to the cubic structure of $SrNbO_3$ thin films and the comparison with the orthorombic Nb_2O_5 is not straightforward. However, the separation of ~4.7 eV measured between the peaks at lower energies is consistent with a dominant Nb^{5+}(d0) character of the sample. [156] Another relevant spectral change occurs at the O K pre-edge. A new peak appears ~1 eV below the O K-edge as the oxygen deposition pressure is increased. The change happens abruptly around a threshold pressure of $P_{O_2}=10^{-3}$ mbar. Although the yellow and green curves correspond to samples fabricated at the same nominal $P_{O_2}=10^{-3}$ mbar deposition pressure, the O-K pre-edge intensity is clearly different for the two films. This behaviour hints the existence of a threshold-like modification in the electronic properties as a function of oxygen defect density. In particular, this change appears to be correlated with a change of metallicity: the near-edge extra feature reflects the less abundance of empty states in the CB available for the electron absorption tranisition., whilst its suppression for samples grown at low P_{O_2} deposition pressures indicate the higher free electron carriers provided by the oxygen vacancies, consistent with the results reported for other hole-doped TMO.[157–159]

Figure 4.13 shows the Nb $M_{2,3}$ absorption edge for two characteristic $SrNbO_3$ samples, namely a n-doped film deposited at $P_{O_2}=10^{-4}$ mbar (orange curve) and a less metallic sample $P_{O_2}=10^{-2}$ mbar (light blue line). The spectra were aligned to the first high intense M_3-t_{2g} absorption edge (red straight line on the graph). The spin-orbit splitting between the two absorption edges is ~15 eV, similarly to other Nb oxides (e.g. NbO, NbO2 and Nb2O5) reported in literature. [140, 155, 156] In particular,

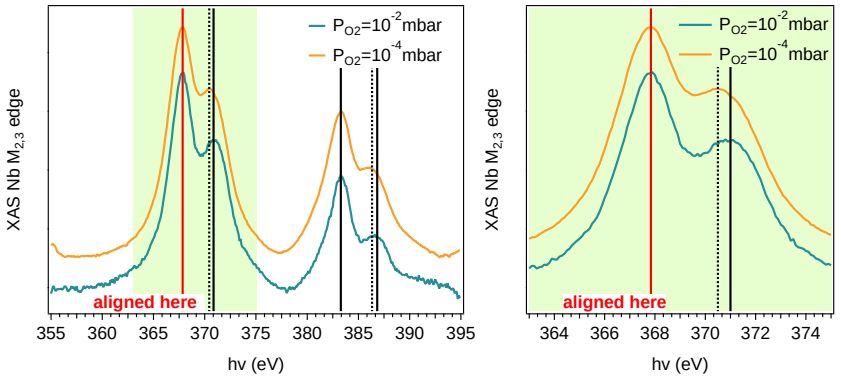

Figure 4.13: *Left panel* Nb $M_{2,3}$ absorption spectra for the $P_{O_2}=10^{-2}$ mbar (light blue) and the $P_{O_2}=10^{-4}$ mbar (orange) $SrNbO_3$ films. The shaded area correspond to the zoom of the M_3 edge reported in the *right panel* to better show reduction of the t_{2g}-e_g splitting.

the spectra present a double-peak structure for both the Nb M absorption thresholds in good consistency with the ligand-field splittiong in the t_{2g}-e_g levels. This lineshape resembles closely the spectra of $Nb^{5+}(d0)$ of Nb_2O_5 and the energy separation of ~3.1 eV is compatible with the data reported for Nb^{5+} valence state. [155] Moreover, the *right panel* of Figure 4.13 denote a spectral evolution as a function of the growth pressure. The splitting between M_3t_{2g}-M_3e_g absorption peaks is reduced by about 500 meV for the lower oxygen pressure. This result suggests a relation with the n-carriers concentration driven by the growth pressure.

Overall, the XAS investigation suggests the $Nb^{5+}(d0)$ ground state configuration is the dominant valence state of the Nb ions, instead of the $Nb^{4+}(d1)$ expected from the ionic model. As the typical probing depth of the total electron yield is of the order of several nm, surface oxidation processes are quite unlikely. Moreover, charge compensation through excess oxygen atoms would have led to the formation of extra oxygen layers in the films' structure, whose presence was not detected by the XRD characterisation results. Finally, Sr deficiency effects were also discarded as Energy Dispersive Spectroscopy (EDS) did not show changes in the Sr:Nb ratio for the whole set of samples.

The XPS investigation on the core levels shows that samples grown with background P_{O_2} higher than 10^{-4} mbar manifests considerable charging effects due to the photoelectric effect. Photon energy of $h\nu$=650 eV was

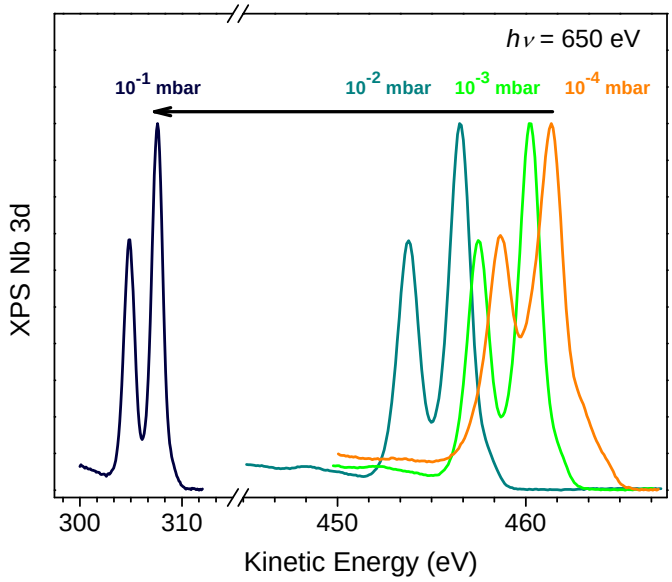

Figure 4.14: XPS spectra of Nb 3d peak acquired at hν= 650 eV for $SrNbO_3$ samples grown at different P_{O_2} pressures.

chosen to avoid any contrast effect arising from electronic absorption resonances and the photon beam flux was reduced to get the best compromise between low sample charging and acceptable signal to noise ratio. Figure 4.14 reports the Nb 3d core level spectra as a function of the oxygen deposition pressure. The shift to lower kinetic energy largely overcomes any value compatible with chemical shift and increases progressively with the preparation P_{O_2}. The maximum shift detected is about 150 eV. This result corroborates the correlation among the conducting/insulating character of the $SrNbO_3$ films and the P_{O_2}. As a consequence, the calibration of the binding energy scale of these spectra is not straightforward. To perform the spectroscopic analysis, the spectra have been aligned to the position detected for to the most conductive samples, namely those deposited at $P_{O_2} = 10^{-4}$ mbar. The latter have been calibrated by means of the Au 4f reference spectra.Figure 4.15 reports the XPS of Nb 3d core levels for two samples grown at the highest (P_{O_2}=10^{-1} mbar) and the lowest (P_{O_2}=10^{-4} mbar) deposition pressures. Stoichiometric samples are obtained for the highest growth pressure (*top panel*). Conversely, several Nb valence states are detected when P_{o_2} is lowered, suggesting oxygen va-

cancies formation. The fitting analysis has been performed using doublets of Voigt functions and adopting Shirley profile for the background. The XPS curve in *top panel* has nearly a unique contribution (>96% relative weight) for the dominant peak. On the other hand, 4 doubled-components are needed to reproduce the data for sample grown at $P_{O_2}=10^{-4}$ mbar. In the framework of the intuitive picture of the hard-sphere model, one can relate the dominant contribution (70%) to the nominal Nb^{4+} valence state expected for stoichiometric $SrNbO_3$. The spectral features occurring at lower binding energies are readily assigned to the Nb^{3+} (14%) and Nb^{2+} (2%) lower valence states, respectively. Finally, Nb^{5+} (14%) is associated to the last doublet at larger binding energy. Thus, the Nb

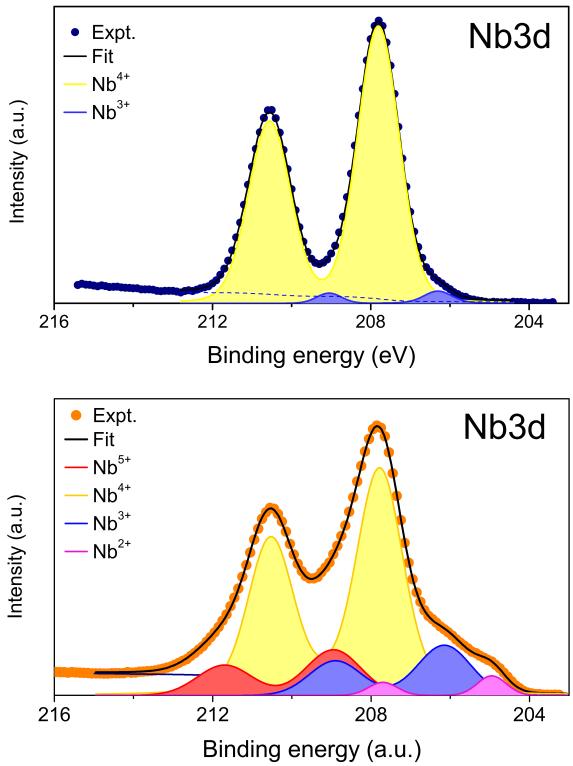

Figure 4.15: Nb 3d core-level spectra measured at normal emission, shining 670 eV photon energy and room temperature on$SrNbO_3$ thin films grown at the highest ($P_{O_2}=10^{-1}$ mbar) and the lowest ($P_{O_2}=10^{-4}$ mbar) O_2 background pressure respectively.

3d core level spectrum highlights the presence of some oxygen and strontium vacancies in the SNO lattice. The loss of oxygen ions in the octahedral cage surrounding the Nb sites favours the formation of the lower 3d valences. Conversely, the higher Nb5+ oxidation state is promoted by Sr deficiency. However, this picture is not completely convincing as re-evaporation of the Sr alkali-earth ion is unlikely. Moreover, XAS investigation suggested a majority Nb^{5+} oxidation state, revealing the presence of electronic carriers and mixed Nb valence only for samples grown at low oxygen pressures. Finally, the huge charging effects for fully oxidised thin films indicate a $4d^0$ (i.e. Nb^{5+}) oxidation state. This fact is also corroborated by comparison of the binding energies of the most conductive sample (fabricated at $P_{O_2}=10^{-4}$ mbar) and the literature on Nb-based oxides core levels. The absolute binding energy scale of this sample could have been calibrated with Au4f reference as this sample did not show any charging issue. The position of the highest peak of the dominant doublet is placed at 207.78 ± 0.01 eV is more consistent with the values reported for Nb^{5+} oxidation state than the expected for Nb^{4+} valence. [160, 161] Thus the dominant Nb valence state has 5+(d0) character and the additional features at lower binding energies correspond to Nb^{4+}(d1) and Nb^{2+}(d3). As a consequence, the doublet at higher binding energies has to be discarded as it would correspond to non-physical oxidation state (i.e. Nb^{6+}) and the asymmetric shape of the core level spectra has to be explained otherwise. A possibility is to attribute the asymmetric profile to the increased metallicity of the sample. In fact, the occurrence of the asymmetric lineshape is abrupt and simultaneous to the change observed in the XAS spectra (i.e. across the $P_{O_2}=10^{-3}$ mbar thresholds), without any progressive change, contrary to the appearance of Nb lower oxidation states. Figure 4.16 compares the Nb asymmetric profile measured in the present work with the tail of metallic Nb^0. The latter was shifted accordingly to match the highest peak of the measured Nb^{5+} and both spectra have been normalised to unity at the peak position. Although additional components at lower binding energies are required to reproduce the data, the two curves coincides at higher binding energies. Thus the asymmetric profile can be regarded as an indicator of the $SrNbO_3$ metallicity. Correspondingly to these results, the Sr 3d core level spectra are reported in the *right panel* of Figure 4.16. The data show the appearance of analogous asymmetric tail that must be attributed to increased metallicity of the system. In fact, oxidation states higher than Sr^{2+} are not possible in the alkaline-earth metals, corroborating a +5 dominant oxidation state for the Nb ions. The asymmetric

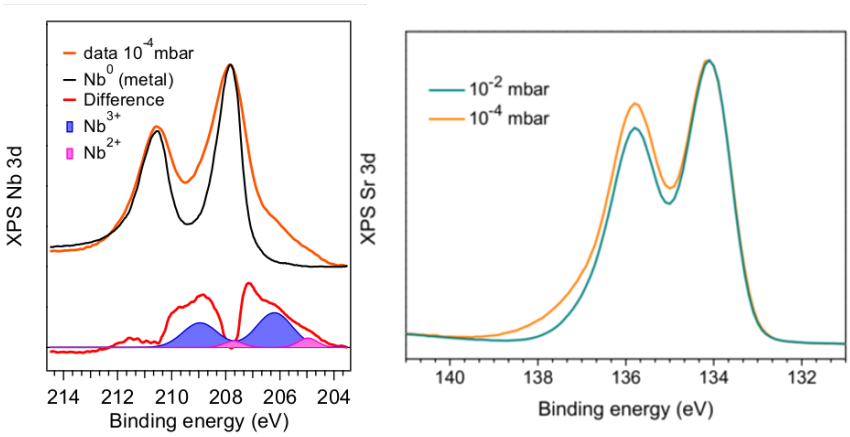

Figure 4.16: *Left panel* Comparison of the Nb3d peak of the metallic samples. *Right panel* Sr 3d core level showing the appearence of the asymmetric tail as the growth pressure is lowered below the thresholds.

tail for core levels could be described by Sunjic and Doniac line-shape, resulting from an almost continuous spectrum of low energy losses of the core level photoelectron due to excitation of electron-hole pairs across the Fermi level.[162] This phenomenon is readily observed in all metals and metallic surfaces of semiconductors. [163, 164]

ARPES

Detailed ARPES study was performed on the most metallic sample at the Low-Energy branch of APE beamline (APE-LE). $SrNbO_3$ samples grown with $P_{O_2} = 1 \times 10^{-4}$ mbar were readily transferred *in-situ* to the APE-LE spectrometer and cooled down to ~77 K. The photoelectric effect final states were probed as a function of the monochromatised synchrotron radiation beam energy and polarisation. All the light polarisations available at APE-LE (linear horizontal LH, linear vertical LV, circular left CL and circular right CR) were exploited to investigate the orbital character of the $SrNbO_3$ conduction band. No trace of the localised in gap states commonly associated with the oxygen vacancies was detected.

Figure 4.17 presents the ARPES $E(\mathbf{k}_{||})$ data as measured at normal emission $h\nu$= 40 eV and two perpendicular linear polarisations (Linear Horizontal and Linear Vertical as referred to the laboratory frame). Panel c displays the DFT calculated band dispersion along the Γ-X high symmetry direction. The observed flatness of the valence band is consistent with

the hybridization of the Nb 4d electrons and the strongly localised O2p orbitals. The major features of the measured VB are ascribable to the electronic structure of the bulk. The flat bands at about 5-6eV binding energy and the hole-like top of the VB in Γare visible in the ARPES data measured with horizontal polarisation. The more dispersive hole like band at higher binding energy (E_B ~8 eV) is best observed when the sample is probed by LV polarisation. The exact matching and the gap values are not exactly reproduced by the calculation, even if the overall shape of the bands is well described. The conduction states are not visible in *panels a, b* because of the weak contrast with respect to the strong photoemission signal coming from the VB. The CB dispersion and its response to light polarisation are reported in *panel d* of Figure 4.17. The blurred flat intensity visible at the Fermi edge for LH arises from the flat cylindrical conduction band. This signal is completely suppressed when the light polarisation is shifted to LV, consistent with d_{xz} symmetry expected for this heavy band. The two degenerate light bands respond differently to light polarisation: the intensity loss around Γfor LH polarisation suggests the light band in the top insect of *panel d* has d_{xy} orbital character. The data measured with LV show an intense signal from the light band that is compatible with d_{yz} symmetry. These features are common in this kind of systems and were extensively reported in ARPES studies on 3d based oxide perovskites [150, 165, 166]. Figure 4.18 reports the ARPES dispersion when the sample is probed by linear polarised radiation of hν=70 eV. This photon energy value gives access to the X-M high symmetry axis for the valence bands as confirmed by comparison with the DFT calculation reported in *panel c*. The conduction band is not visible due to the image contrast. The two features located at E_B ~4 eV at the BZ edges (i.e. $k_x = \pm 0.8$ Å) are detected when LV polarisation is used *panel b*. Moreover, the "dove-shaped" band located between 5 eV and 6 eV binding energies appears with strong intensity when the sample is probed with LH polarised light.

The photon energy dependence of the Fermi surface is reported in Figure 4.19. Data were acquired in the first BZ using LH polarised light. *Panel a* shows the sketch of the reciprocal space investigated with the photon energies. Red lines mark the edges of the extended Brilloin zone, while the Fermi energy contour are represented with the same colour scale of the 3D rendering of Figure 4.11. Finally, the blue arcs highlight the reciprocal space portions accessible for the different photon energy values. In particular, they can be assigned to k_z values assuming a free-electron

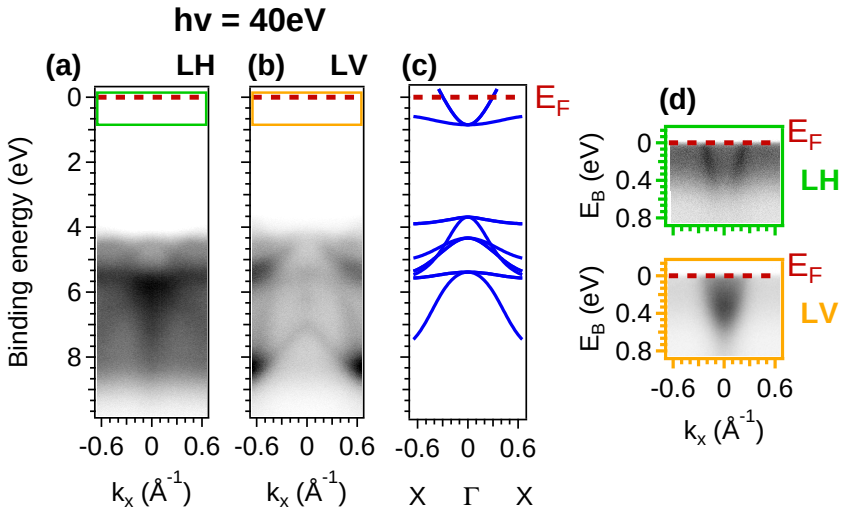

Figure 4.17: ARPES data measured at hν= 40 eV with linear polarised light as a function of light polarisation. (a) linear horizontal (b) linear vertical (c) ARPES results are compared with the theoretical bands calculated along Γ-X high symmetry direction. (d) Details of the conduction band dispersion along Γ-X are also reported as a function of linear light polarisation.

final state and using $V_o = 15$ eV inner potential and the pseudo-cubic cell a = 4 Å lattice constant. ARPES (k_x,k_y) Fermi cuts are reported in *panels b - f* for photon energies in the range from 40 eV to 80 eV. Comparison between the data set and the sketch in *panel a* confirms that ~80 eV photon energy correspond to k_z close to Γ_{oo3}. Photons of ~70 eV also probe a BZ portion quite close to the BZ centre (Γ-X-M plane). The heavvy bands cross the Fermi level at ~0.3 Å along the edge of the Brillouin zone. The two light bands appears as circular Fermi contours centred at Γin the middle of the cross formed by the heavvy bands. Conversely, the bandstructure at the BZ edge (i.e. the X-M-R plane) is reached when ~60 eV photon energy is used. The cylindrical band is the only one accessed at this photon energy, in consistency with the calculation. The finite, blurred signal outside the circle is probably due to k_z broadening, which is related to the electron inenlastic mean free path λ_{IMFP}[167]. The λ_{IMFP} is of the order of few angstroms in the photon energy range investigated here, that corresponds to few tenths of the Brilloine zone of k_z broadening as reported for other oxide perovskites [168, 169]. Finally, intermediate portions of the BZ (namely near the cylindrical tube nesting) are probed

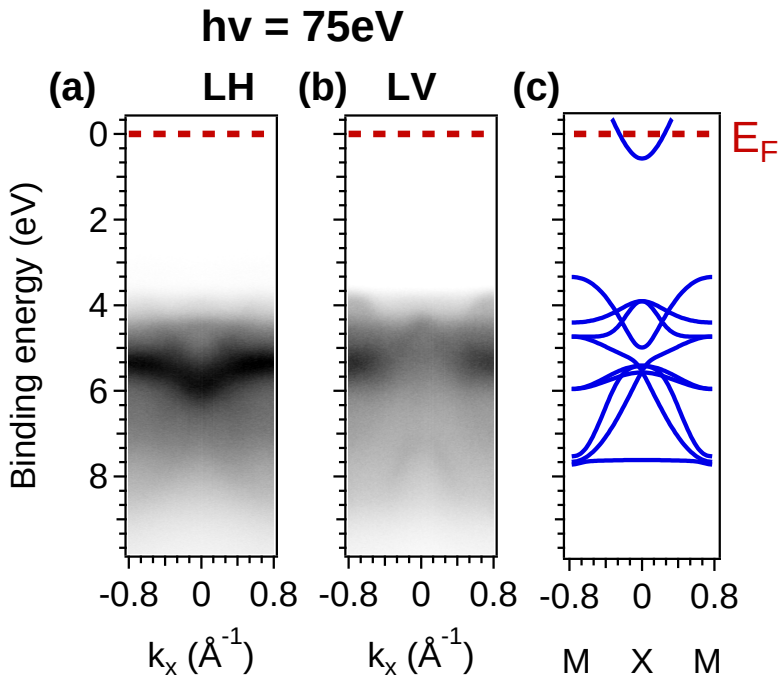

Figure 4.18: Valence band dispersion of the $SrNbO_3$ sample measured with hν= 70 eV as a function of light polarisation: (a) linear horizontal (b) linear vertical. (c) Comparison with DFT calculations aloong X-M high symmetry direction.

when the sample is probed with hν~40 eV and hν~65 eV. The results are consistent with the ARPES data reported for other perovskites [150, 152, 154]

The carrier density $n_{3D} = V_{FS}/(4\pi^3)$ has been estimated from the volume enclosed by the Fermi surfaces (V_{FS}), by means of the generalised Lüttinger theorem [170]. V_{FS} was estimated assuming electron-like character for all the three conduction bands. The flat band was approximated with three mutually orthogonal cylinders of ~0.3 $Å^{-1}$ radius, $\frac{2\pi}{a}$ height and interpenetrating at Γ. The contribution to the total volume of the flat band is ~($3*V_{cylinder}$-$2*V_{intersection}$). The volume of two spheres of was then added to obtain V_{FS}. This gives n_{3D}~1×10^{22} cm^{-3} (i.e. ~0.6 e^- per unit cell volume). This result derived from ARPES is consistent with the results of transport experiments reported in the literature for $SrNbO_3$ thin films[130–132] and in typical range of carriers concentration for oxide

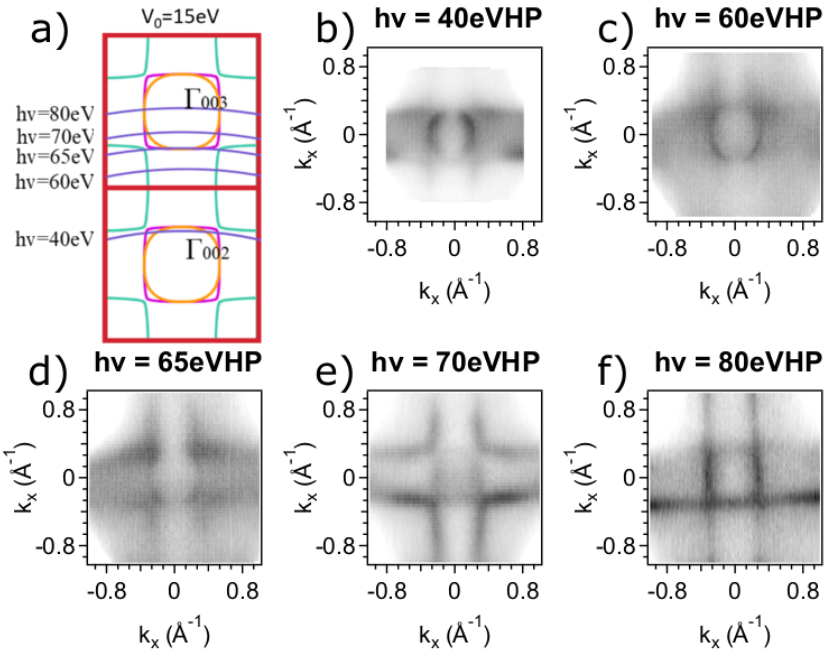

Figure 4.19: Photon energy scan probing the k_z dispersion of the Fermi surface (a) Sketch of the Fermi surface in the extended Brillouin zone scheme. Red lines represents the pseudocubic Brillouin zone edges, while the calculated Fermi surface is drawn in orange, pink and light blue for the two spherical electron pocket and the cylindrical bands, respectively. Blue curves highlight the isoenergy cuts investigated as a function of the photon energy. (b) - (f) (k_x,k_y) Fermi energy contours measured using linearly horizontal polarised light at different k_z positions (i.e. different photon energy) (b) 40 eV, (c) 60 eV, (d) 65 eV, (e) 70 eV, (f) 80 eV

perovskites systems[151, 152].

The ARPES data reported in Figure 4.20 gave more insight in the orbital character of the conduction band. The data set compares the Fermi surface measured at different photon energies (from 40 eV to 80 eV) for the two orthogonal linear polarisations (LV *top row* and LH *bottom row*). According to the APE-LE experimental geometry described in chapter 2, LH and LV possess even mirror symmetry with respect to the x-z and the y-z emission planes, respectively. These are also well defined symmetry planes for the $SrNbO_3$ d orbitals, thus the orbital character of the three electronic bands could be determined. The flat cylindrical bands

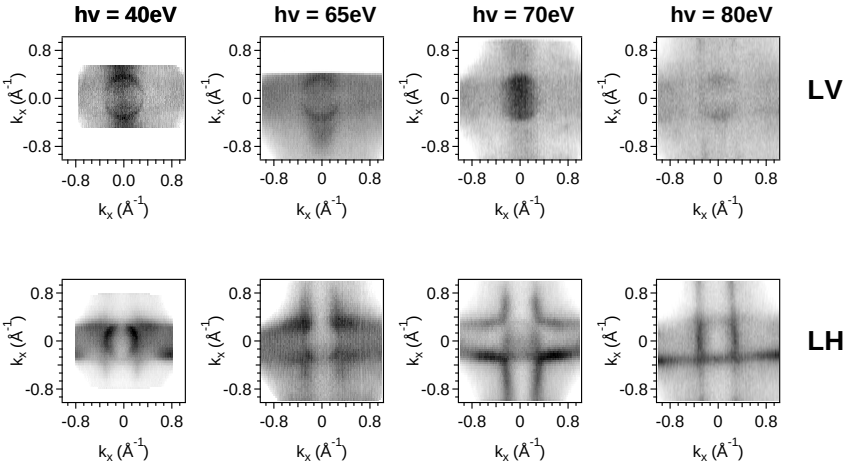

Figure 4.20: Fermi surface as a function of photon energy and linear light polarisation. *Top row* Fermi surface measured with linear vertical polarised light and for 40 eV, 65 eV, 70 eV and 80 eV photon energies. *Bottom row* Fermi surface probed with linear horizontal polarised light and the same photon energies.

are well visible and quite intense in photoemission with LH polarisation. On the other hand, these signals are strongly suppressed for Lphotoemission with V polarisation in the whole range of the investigated photon energies. These results indicate the flat conductive band arise from d_{xz} orbitals, which have even/odd mirror symmetry in respect to x-z/y-z emission planes respectively. Disentangling the behaviour of the two spherical bands is more difficult as they are nearly degenerate. Nevertheless, their different response to the photon energy may be exploited. A circle centred in $(k_x,k_y) = (0,0)$ appears when the sample is probed with $h\nu$=40 eV. In particular, for LH polarisation the spectral intensity is suppressed for $k_x = 0$, which means the electronic state has odd symmetry in respect to x-z plane. When the polarisation is changed to LV a similar suppression of the photoemission intensity is found for $k_y = 0$ (i.e. odd parity in respect of y-z emission plane). The situation is different for $h\nu$=70 eV. At this energy the highest photoemitted signal for the light bands is found in the case of LV polarised light, while LH polarisation moderately suppresses the intensity of those bands. The former response is consistent with the d_{xy} orbital, which has odd mirror parity for both the examined planes. The behaviour at 70 eV indicates the second light band arises from d_{yz} orbital, which has even parity for y-z plane and odd symmetry in respect

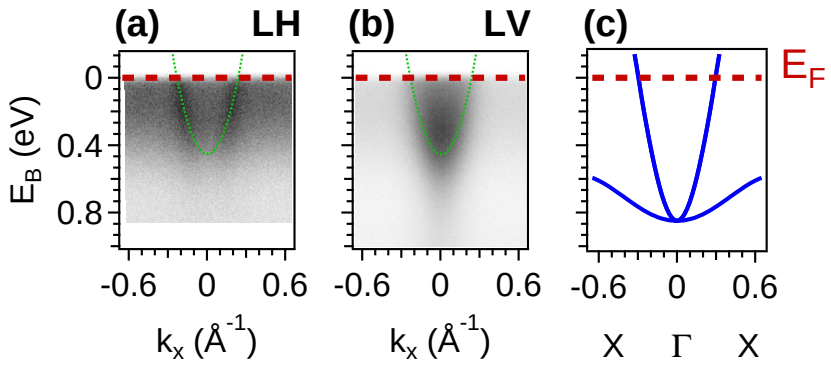

Figure 4.21: Conduction band along the Γ-X direction measured with hν30 eV and (a) LH (b) LV light polarisation. (c) Theoretical CB dispersion as predicted by the DFT calculation.

to x-z. Finally, d_{z^2} and $d_{x^2-y^2}$ orbital characters can be excluded, as their even parity for both x-z and y-z planes would have prevented the band suppression for both linear polarisations. All these findings confirm the conduction band is constituted by the t_{2g} orbitals, has expected from the DFT calculated projected DOS reported in Figure 5.13. These features are indeed quite usual in TMO systems and have been extensively reported in ARPES studies on 3d based oxide perovskites. [150–152, 165, 166]

The overall consistency of the ARPES data with the plain DFT calculations reported above could lead to overlooking correlation effects in this 4d based material. On the other hand, a closer look reveals some discrepancies between the experimental data and the bulk DFT calculation. Although the shapes of the bands along both the Γ-X and X-M directions are well captured by DFT, the exact matching of the features and the gap values are not correct. For instance, the flat calculated band in the deeper region of the VB (i.e. ~8 eV binding energy)has no counterparts in the whole set of the experimental data. The calculated valence bands are also rigidly shifted upward of about 500 meV with respect to the measured spectra. More differences are found when inspecting the conduction bands. Figure 4.21 directly compares the CB along the Γ-X direction. The energy-momentum dispersion of the light degenerate bands is readily fitted with a parabola that gives a value of $E_B = 0.45 \pm 0.01$ eV for the bottom of the conduction band. The calculated CB minimum, instead, is located at $E_B = 0.85$ eV binding energy, i.e. it is shifted downward by

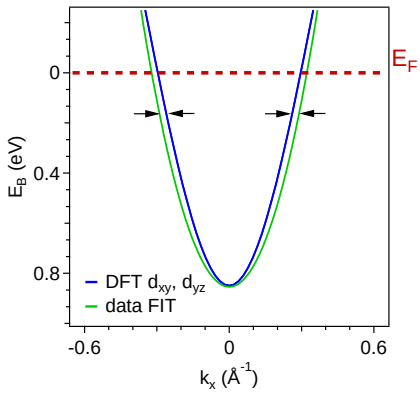

Figure 4.22: Band curvature of the calculated d_{xy}, d_{yz} bands (blue line) and the curvature extrapolated from the data fitting (green curve). For better comparison the FIT curve is shifted downard of 0.4 eV

~0.4 eV. It is well known that the gap is systematically underestimated by the DFT calculations. The experimental separation between the VB and CB at the Γpoint is indeed about 1 eV larger than the calculated one. The reason of this discrepancy may arise from errors in the calculations like an inadequate choice of the pseudopotentials. However, poor evaluation of the energy gap is unlikely in the simulation of metallic systems as $SrNbO_3$. On the other hand, GW calculation by Zhu and collaborators have reported the increases of the energy band gap accompained by slight mass renormalisation when e-e correlations are taken into account. [127] Figure 4.22 reports the band dispersion of the DFT calculated d_{xy} d_{yz} orbitals and the parabola extrapolated from the ARPES data. For better comparison the FIT curve has been rigidly shifted downard of ~400 meV. The different curvature of the two bands suggests mass renormalisation. To quantitatively explore this scenario, both the experimental (m^*_{EXP}) and calculated (m^*_{DFT}) effective masses have been estimated by means of the formula: $m^* = \hbar^2 |\frac{\partial^2 E_k}{\partial k^2}|^{-1}$. The curvature of the DFT band has been extracted through a parabolic fitting near the band bottom at the Γpoint, which gives an effective mass $m^*_{DFT} = 0.32 \pm 0.02 m_e$. The experimental effective mass was $m^*_{EXP} = 0.46 \pm 0.08 m_e$. The renormalisation mass factor of ~1.5 is readily obtained, which is quite close to the value reported for the $SrVO_3$ $3d^1$ correlated perovskite [152, 154]. This result hints to electron correlation being relevant in the $SrNbO_3$ system, despite the reduced localisation of 4d bands.

4.3. Conclusions & outlooks

This chapter reports the study of the electronic structure of PLD-grown $SrNbO_3$ thin films. A preliminary effort to obtain reliable, high bulk and surface quality thin films of the material has been carried out adopting a comprehensive array of *ex-situ* and *in-situ* structural characterisation methods. Once the growth protocol has been optimised, samples grown with different oxygen vacancy concentrations were produced by controlling the background partial pressure during the deposition. *In-situ* X-ray spectroscopic techniques investigated the electronic structure evolution as a function of the oxygen vacancies' concentration in the samples. XAS spectra surprisingly showed a predominant 5+ oxidation state for Nb suggesting a $4d^0$ electronic state of the transition metal in the optimally stoichiometric perovskite. The binding energy position of the main components of Nb 3d core levels and the asymmetric tail detected in samples with mixed valence states corroborate this hypothesis. The electronic bandstructure of the most conductive sample were probed by ARPES and the results were compared with those calculated with conventional DFT. The Fermi surface has been observed to have cylindrical shape, originated from three bands with t_{2g}orbital character. In general, the consistency between DFT calculations and ARPES data has been verified. The carrier density extracted from the volume enclosed by the Fermi surface is also consistent with reference values reported for perovskites. Nevertheless, discrepancies between the ARPES and the DFT results appear in the bandwidth and the consequent effective mass. These differences suggest that electron correlations are at work in $SrNbO_3$.

More experimental work should be performed to further study the electronic properties of this chameleonic oxide. ARPES studies of samples with less oxygen deficiency may be performed with alkali doping. Alkaline atoms adsorbed at the sample surface would indeed compensate for the reduced conductivity and allow to checking the evolution of the CB as a function of n-doping concentration. A gradual filling of the CB with n-doping concentration would be a further proof of the counterintuitive dominant Nb^{5+} (i.e. $4d^0$) state in stoichiometric $SrNbO_3$. This problem may be tackled also with Soft-Xray ARPES measurements. Resonant ARPES across the Nb and O edges may provide further insights on the electronic character of the electronic bands. Finally, *in-operando* compensation of oxygen vacancies (e.g. with oxygen dosing at the surface) may add information on the role of these defects in determining the sample

metallicity.

5. Role and manipulation of oxygen vacancies at the surface: the TiO_2 case study

> Solo dopo aver conosciuto la superficie delle cose, – conclude – ci si può spingere a cercare quel che c'è sotto. Ma la superficie delle cose è inesauribile.
>
> Italo Calvino - Palomar (1983)

5.1. The TiO_2 case study

Titanium dioxide (TiO_2), particularly its anatase allotropic phase, raises high interests as its functional properties may be exploited in new

devices such as solar cells, transparent conductive oxides, memristors and spintronics [171]. These performances are connected to the conductivity of this system and strongly depend on the presence and abundance of excess electrons that originate from intrinsic defects, dopants or light excitation processes [172–175]. Understanding the physics of the anatase conductive properties of anatase is thus crucial pand may lead to tailored control and exploitable functionalities. TiO_2 anatase is an insulator with a 3.2 eV band-gap, however, non-dispersive in-gap state (IG) as well as dispersive electron state (2DEG) near the Fermi level have been widely reported in the literature [176–181]. Nevertheless, an overall picture is still to be reached. The first extensive ARPES study of the metallic state in anatase (001) samples has been conduct by Moser and collaborators [177], who show that oxygen vacancies (V_O s) creation induce an electron doping in the TiO_2 system. They claim the excess electrons populate the conduction band as they detected quite strong band dispersion along k_z. They also investigated the evolution of the conduction state and its quasiparticles as a function of the abundance of oxygen defects. In that study the defects' concentration was determined either by intense beam irradiation or by oxygen exposure. Changes in the many-body excitations of the system were correspondingly detected. A polaron-like quasi particle was measured for samples with low doping. It evolved into a Fermi-liquid regime when the number of carriers is increased. These results are consistent with a picture developed by previous theoretical works. [182, 183] These papers report that the two excess electrons created by bulk oxygen vacancies V_O populate two different electronic states of anatase: a localised IG and a delocalised state which mimics the conduction band. The crossover between the e-ph coupling and the Fermi liquid excitation observed by Moser et al. has been recently reproduced by *ab initio* many-body calculations[184]. However, more recent experimental works have provided evidence of the near-Fermi two-dimensional nature of the metallic state, similar to what reported at the surface of other titanates [185, 186] and transition metal oxide (TMO) parent compounds (e.g. $SrTiO_3$,$KTaO_3$) [151, 166, 187, 188]. Rödel and co-workers have shown metallic states hosted on both (001) and (101) anatase surfaces, characterised by two-dimensional character. Their data show no k_z dispersion of the 2DEG, although the photoemitted intensity is strongly modulated by final state matrix element effects [178, 189]. They also probed the effects of beam irradiation which induces V_O at the surface, eventually leading to the local damage of the surface structure and the

disappearance of the 2DEG. Wang et al. [180] succesfully compare their data with a model linking the 2DEG to the peculiar anatase (001) surface reconstruction [190], but they did not observe complete destruction of the 2DEG. Excess electron may also be induced by depositing reducing agents at the TMO's surfaces, namely Al [191] and alkaline atoms [192]. In particular, Yukawa and collaborators show that K impurities transfer electrons to the 2DEG that may form within nanometres below the surface while localised electrons are formed at the TiO_2/K interface.

The aim of the present work is to explore:

- the surface/subsurface depth distribution of the V_O providing the excess electrons (i.e. within few nanometres from the topmost layer)
- the relation between those electrons and the 2DEG as well as the IG states
- the response of both states when the system is exposed to reducing or oxidising conditions.

5.2. Results and discussion

The research programme was carried out in two steps. The sample synthesis was directly addressed aiming to control the carrier's abundance in the material, whilst fine analysis of the electronic states was performed both with high resolution experiments (ARPES) and Density Functional Theory (DFT) calculations.

Thin film technology was exploited to tune the carriers in the sample. *In-situ* UHV growth epitaxial thin films obtained by PLD allows us to compare the electronic states of as-grown TiO_2 samples and thin films which underwent mild UHV annealing treatment. *Ex-situ* structural investigation probed the high quality of the grown samples. VUV and X-ray based electron spectroscopies were exploited to monitor the spectral evolution induced either by UHV annealing either by fluxing molecular Oxygen on the sample surface. Finally, a joint collaboration with Selloni's theoretical group provided Density Functional Theory (DFT) calculations which helps to clarify the role, the formation mechanism and the possible control of defect states formed at the (001) surface of anatase TiO.

5.2.1. Sample growth optimisation

Anatase TiO_2 thin films were grown by means of the *in-situ* UHV PLD setup described in chapter 2. Rutile TiO_2 single-crystal was ablated by aKrF excimer laser pulse (ns) of about $2\,J\,cm^{-2}$ energy density. The typical laser repetition rate was 3 Hz and the substrate was kept at 700 °C during deposition. Highly pure oxygen background pressure (99.9999% purity) was regulated around 10^{-4} mbar during the growth. Standard samples were grown with a nominal thickness of ~20 nm.

To determine the optimal anatase sample for ARPES investigation, several films were deposited on different substrates: $SrLaAlO_4$, $LaAlO_3$, $SrLaGaO_4$ and Nb−$SrTiO_3$ (i.e. 1 %wt). The structural and electronic properties of each film were characterised both *in-situ* and *ex-situ*. The results are summarised in Figure 5.1. The *left side* reports the Θ-2Θscans of the (004) Bragg diffraction peak of anatase films. The bulk anatase peaks position is marked by the straight black line. *Right side* shows the respective DOS of shallow states as probed by photoemission with hν=46 eV. Fully strained TiO_2 samples were obtained on $SrLaAlO_4$, $LaAlO_3$ and $SrLaGaO_4$: compressive (i.e. mismatch d ~ +1%), strain-less (d < -1‰) and tensile (d ~ -1%) respectively. A fully relaxed TiO_2 sample was deposited on Nb−doped $SrTiO_3$ substrate, which imposes a very large in-plane mismatch of ~-3%. The out-of-plane lattice parameters derived from the XRD spectra confirm that $SrLaAlO_4$ induce in-plane compression of the film as reflected by a c-axis elongation (i.e. 9.59 Å). Conversely, a reduced out-of-plane value 9.46 Å indicates the tensile in-plane strain of films grown on $SrLaGaO_4$. Finally the bulk-like value c = 9.49 Å lattice parameter proves that the strain is negligible strain for TiO_2 films grown on $LaAlO_3$ substrates. The very large in-plane lattice mismatch between anatase and $SrTiO_3$ leaded to a relaxed film (c = 9.50 Å) that is usually accompanied with the formation of dislocations, point defects and stacking faults, most likely occurring at the interface with the substrate. The stabilisation of the 2DEG state is not affected by the overall structural quality of the TiO_2 samples. As reported in the *right panel* of Figure 5.1, all the DOS measured at hν= 46 eV show the presence of the metallic state irrespective of the particular substrate used as growth template albeit the sharpest peak is measured for the sample with minimum mismatch (i.e. grown on $LaAlO_3$). The IG state is also detected for all the samples, but it is definitely sensitive ti the substrate: the IGs spectral weight is centred at different binding energies (i.e. ~2 eV for $SrLaAlO_4$, ~1.6 eV

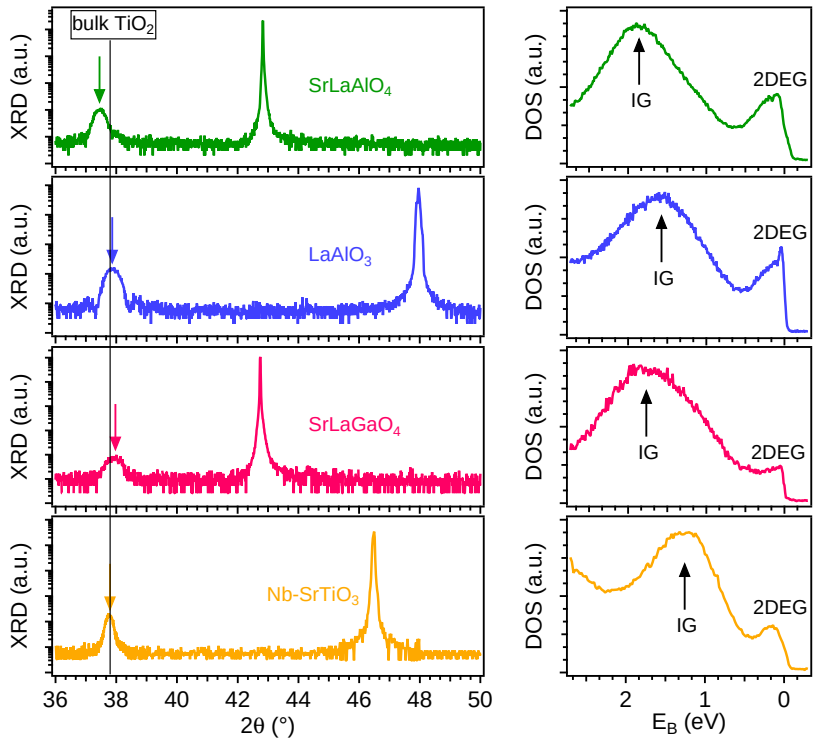

Figure 5.1: Anatase TiO_2 growth optimisation *Left side* Θ-2Θscans measured around the (004) Bragg diffraction peak of anatase films deposited on different substrates, namely $SrLaAlO_4$, $LaAlO_3$, $SrLaGaO_4$ and Nb−$SrTiO_3$ (*from top to bottom*). Straight black line emphasises the position of the Bragg reflection for bulk TiO_2.*Right side* The respective integrated DOS close to the Fermi edge. Both the localised IG and the delocalised 2DEG spectral intensities are marked.

for $LaAlO_3$, ~1.8 eV for $SrLaGaO_4$ and ~1.2 eV for Nb−$SrTiO_3$). The asymmetric shape of the peak, particularly evident for the strained films, indicates the presence of more components located at shallower binding energies (~1 eV). The origin of this spectral intensity variation was is likely related to fine structural modifications induced by the substrate strain which reflect on the films' electronic properties. However, this aspect of the electronic bands was not further investigated in the present work.

To perform ARPES investigation it is mandatory to grow samples with high surface structural quality, namely very low surface roughness and long range structural order. This can be achieved by operating low growth rates. Qualitatively the impinging atoms can reach an equilibrium distri-

bution onto the substrate at low deposition rate, favouring the epitaxial growth and to the formation of a highly ordered top surface. Systematic *ex-situ* low-angle X-ray reflectivity (XRR) measurements were performed after each film deposition to determine the optimal anatase film growth protocol as well as to monitor the surface roughness. Figure 5.2 reports a XRR pattern of a TiO_2 film deposited on$LaAlO_3$(blue circles) and the respective simulated reflectivity obtained by mean of the IMD package of XOP software (red curve) [144, 145]. An approximately 27 nm thickness is extracted from the oscillations of the simulated curve, which perfectly matches the experimental data. The estimated growth rate is about 171 laser shots per anatase TiO_2 unit cell (i.e. ~1 uc/min) and the sample roughness is ~4 Å, which is approximately half of the anatase unit cell. Furthermore, the XRR oscillations fall below the experimental resolution of the X-ray diffractometer starting from $2\Theta = 4°$-$5°$, thus the estimated value is the upper limit of the surface roughness. The surface long range order quality was probed by *in-situ* LEED and representative results are summarised in Figure 5.3, reporting the LEED patterns of TiO_2 thin films deposited at different growth oxygen pressure. The (4x1)-(1x4) reconstruction is readily observed, consistent with other experimental observations [193, 194]. The origin of such surface rearrangement has been proposed to arise from structural reorganisation to release the large surface stress of the unreconstructed anatase surface[190]. From Figure 5.3 it can be seen that the (4x1)-(1x4) surface reconstruction of (001) anatase is not affected by the oxygen growth pressure, albeit the sharpness of the spot changes according to the sample metallicity. In principle the weakening of the LEED spot intensity could be attributed to an increased surface roughness of the sample, but this interpretation can be excluded in the present case as the XRR patterns did not change upon annealing (i.e. the surface roughness did not change within 0.4nm). Therefore the diminished intensity of the LEED pattern have been ascribed to the reduced sample metallicity, which is directly linked to the oxygen vacancies concentration, which can be tuned by carefully setting the growth parameters, chiefly the oxygen background pressure during the growth [181]. The stability of the surface reconstruction corroborates the model proposed by Lazzeri and Selloni [190] and it differs from other transition metal oxide systems that display various surface reconstructions for small changes in the V_O density [195, 196].

Further improvements of the anatase film quality were achieved by depositing a buffer layer of few unit cells on the substrate(e.g. $LaAlO_3$,

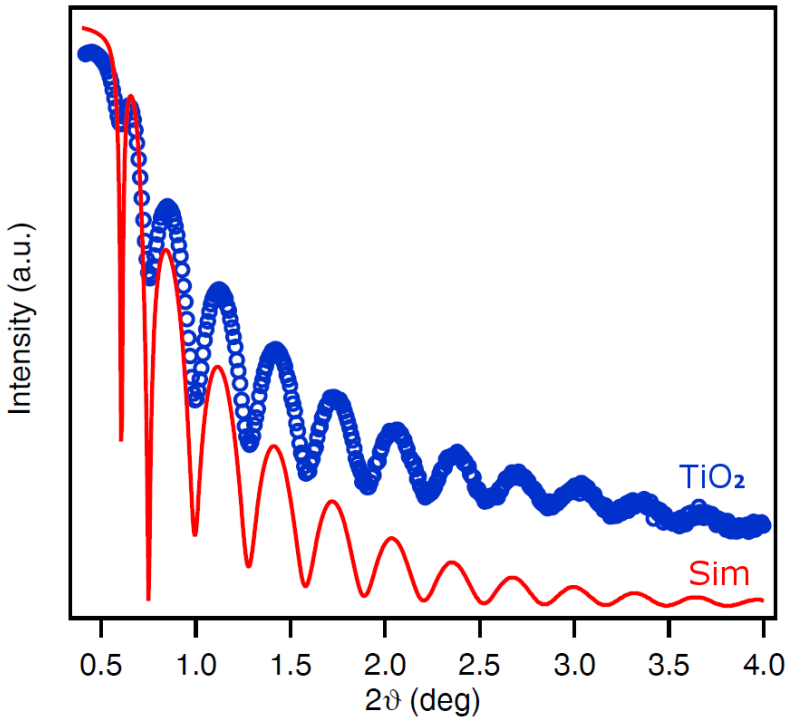

Figure 5.2: X-ray reflectivity (XRR) measurements for a standard ~27 nm thick TiO_2 sample. Simulation of XRR oscillations has been performed by using IMD package of XOP software.

$LaNiO_3$) to optimise the interface with the film reducing the overall surface roughness.

The systematic growth refinement and structural check led to the reproducible synthesis of high quality TiO_2 films grown as needed for a reliable ARPES investigation. The anatase samples presented in this thesis possess excellent crystal structure without any detectable minority phase, long range surface order and very low surface roughness. The samples were then readily transferred *in situ* to the APE-Low Energy beamline branch for ARPES measurements. This is a unique feature of the APE-NFFA laboratory that enables the spectroscopist to work on pristine, freshly grown samples, that do not see any background pressure between the growth and the fine analysis. New growth batches can be as well produced during ARPES experiments getting *on-line* feed-back to the growth conditions.

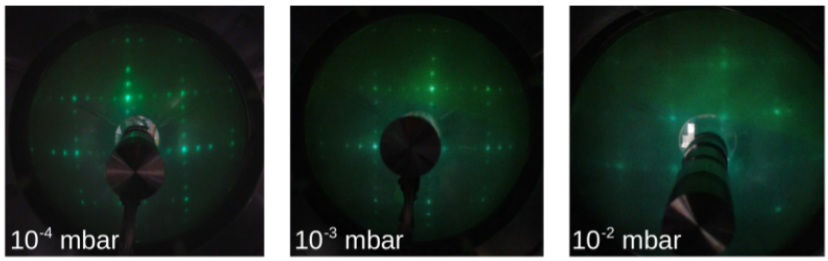

Figure 5.3: LEED patterns of anatase TiO_2 thin films deposited at different background growth-pressures, i.e. *from left to right* $P_{O_2} = 10^{-4}$ mbar, $P_{O_2} = 10^{-3}$ mbar and $P_{O_2} = 10^{-2}$ mbar. The same (4x1)-(1x4) surface reconstruction is found for all the growth conditions.

Figure 5.4 summarises the electronic properties along the Γ- X direction of the surface projected Brillouine zone for an optimal anatase sample. Dispersive and sharp features are detected in the valence band that spans from 4 eV to 8 eV binding energies (*right panel*), consistent with the ~3.2 eV energy band gap value expected for this insulating system [197, 198]. Nevertheless, additional spectral weight is present within the energy gap (i.e. in the 0 eV to 3.2 eV range) as clearly shown by the insects of the integrated DOS in the bottom left panel of Figure 5.4 and by the corresponding ARPES spectrum (*top left*). Two staes are readily identified: a broad, non-dispersive in-gap state (IG) located at E_B ~1.6 eV and a dispersive metallic state reaching the Fermi energy. Figure 5.5 shows the Fermi contours measured in the 1st Brillouin zone, measured on varying the light polarisation at $h\nu = 46$ eV. The bright circle centred at the Γpoint corresponds to an electron gas (2DEG), characterised by parabolic dispersion. Aside such a state, several replica occur along both k_x and k_y directions, reflecting the (4x1)-(1x4) reconstruction of Ti atoms at the anatase(001) surface [180, 190] also detected in the LEED patterns. The dependence on the light polarisation summarised in Figure 5.5 shows gaps in the photoemitted intensity, which reveal the symmetries typical of the t_{2g} orbitals arising from Ti 3d states. In particular, these symmetry-related selection rules indicate that the 2DEG state of anatase has a d_{xy} orbital character. As described in chapter 2, the slit of APE-LE analyser is oriented vertically in respect to Elettra electron beam orbit. As discussed above, the sample is probed with the Γ-X direction aligned with the analyser slit. Two orthogonal mirror plane are therefore identified: the xz plane (defined by the analyser slit and the surface normal) and the yz plane, which

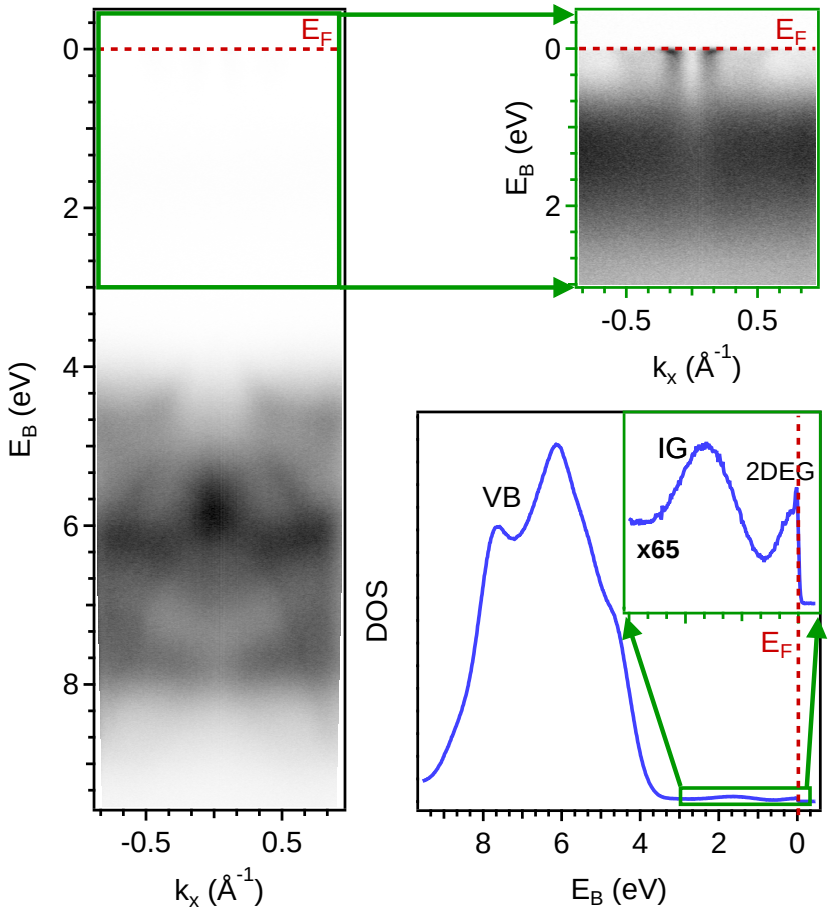

Figure 5.4: ARPES band dispersion of an optimised anatase $TiO_2/LaNiO_3/LaAlO_3$ thin film. Spectra have been acquired at hν= 46 eV and horizontal polarisation. *Left panel* Bulk valence band dispersion, *right top* Detail of the band dispersion close to the Fermi level, clearly showing the localised IG and the metallic 2DEG. The non-dispersive IG state corresponds to the flat broad state locate between 1 eV and 2 eV binding energies. Conversely, the 2DEG is characterised by parabolic electron-like dispersion obeying t_{2g} symmetry rules. *Right bottom* Integrated DOS, the insect has been enlarged ~65 times.

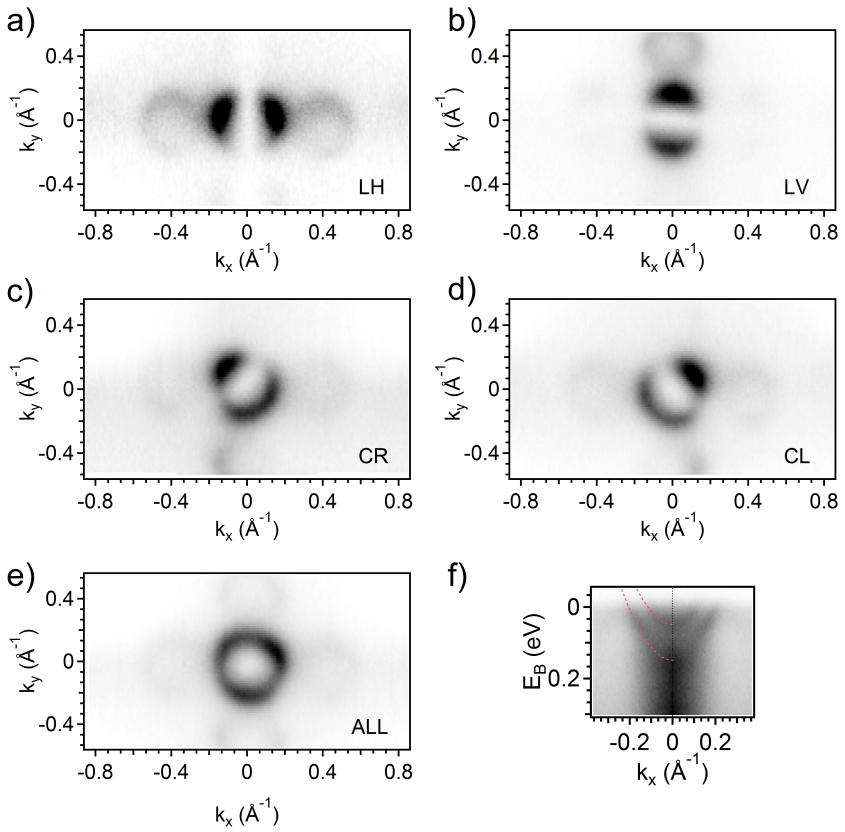

Figure 5.5: 1st Brillouin zone anatase Fermi surfaces measured with hν= 46 eV and all the photon polarisations available at APE-LE beamline: (a) linear horizontal, (b) linear vertical, (c) circular right (d) circular left. (e) Reports the sum of all the four Fermi surfaces - from (a) to (d) - that mediates the symmetry-related lack of intensity typical of electronic states with d_{xy} orbital character. e) The sum of all the spectra acquired with the polarisation available at APE-LE beamline. f) The parabolic dispersion of the 2DEG as measured in the 2nd BZ.

contains the photon beam and the surface normal. In this geometry, the linear horizontal polarisation (LH) has odd mirror symmetry with respect to the xz plane, whilst the vertical polarisation (LV) has even symmetry. Let's now consider the symmetries of the t_{2g} orbitals (i.e. d_{xy}, d_{yz} and d_{xz}) in respect to such a plane: the d_{yz} has even parity, while both d_{xy} and d_{xz} possess odd symmetry. Thus, from *panel b* of Figure 5.5 one can readily exclude d_{yz} orbital character, as photoemission intensity for k_y=0 Å^{-1} should appear when excited with LV polarisation (even symmetry of the

final state). On the other hand, switching to LH polarisation the spectral intensity vanishes for k_x=0 Å^{-1} (*panel a*). LH has even parity under reflection about the yz. To be detected in Γ_o the photoemitted final state has to be even in respect to both the xz and yz planes, namely it should have d_{xz} orbital character (even symmetry under reflection in respect to yz). Thus, the orbital character of the 2DEG is d_{xy}, as expected from the degeneracy-lifted of the t_{2g} caused by the tetragonal unit cell structure of anatase. These results are consistent with the reported literature both for anatase [177, 178, 180] and other transition metal oxides. [151, 166, 189] *Panel f* of Figure 5.5 reports the parabolic dispersion of the 2DEG as measured in the 2nd Brillouin zone, where no suppression due to symmetry rules is observed anymore. The inner replica arising from lateral confinements of the surface reconstruciton is also visible. The parabolic fit of the two metallic states is also reported as red-dashed lines on the left-side of the ARPES spectrum.

5.2.2. As-grown vs reduced anatase samples

To explore the dependence of the 2DEG electron state at the anatase surface upon V_O density, mild after-growth UHV annealing was performed to slightly modify the TiO_2 thin film oxygen stoichiometry. Annealed samples were maintained at the growth temperature of 700 °C for 10 minutes in UHV (PLD chamber base pressure is ~2×10^{-7} mbar). Annealing in vacuum is a common procedure to deplete oxygen from oxide systems [143, 195, 196], it can lower the sample quality, though (e.g. by increasing the interface disorder caused by Al segregation). Thus, structural investigation has been performed prior to ARPES experiments. The High-Resolution Transmission Electron Microscopy (HRTEM) images reported in Figure 5.6 show no difference in the sample structure after annealing: both the as-grown and the annealed thin films reveal the occurrence of a regular modulation in the HRTEM image. In the literature, this feature has been attributed to periodic displacement of V_O throughout the TiO_{2-x} film thickness[199–201]. Above all, the sample interface's sharpness was preserved in the annealing process as no indication of segregation of either crystalline or amorphous grains were detected within the TiO_2 matrix. Finally, the sample retains its surface's flatness as also confirmed by the LEED pattern of Figure 5.7. Figure 5.6 also reports the Θ-2Θscans around the (004) symmetric Bragg reflection for both the as-grown (black dots) and the annealed (red) samples. The peak position is slightly shifted

towards lower angles in the case of the annealed sample, which indicates an increase of the c-axis lattice increases of $\sim(2.0 \pm 0.1) \times 10^{-2}$ Å. This is a well known signature of the V_O creation during the annealing process, typical in other transition metal oxide systems, [143, 202, 203] and consistent with the unit cell expansion arising from repulsion among the Ti cations.

To probe the local electronic environment of the Ti atoms we have performed soft X-ray spectroscopy both in absorption and core level photoemission. Representative results are summarised in Figure 5.8. The top panels report the Ti2p core level photoemitted intensity and the bottom panel shows the XAS spectra across the Ti2p absorption edge for the as-grown (blue curve) as well as the annealed (red curve) samples. The results confirm the oxygen loss of TiO_2 as a consequence of the annealing process. The XPS signal shows two main peaks at binding energies of 459.4 eV and 465.1 eV, corresponding to the spin-orbit split $Ti2p_{3/2}$ and $Ti2p_{1/2}$ components respectively. The separation between the peaks is ~5.7 eV,

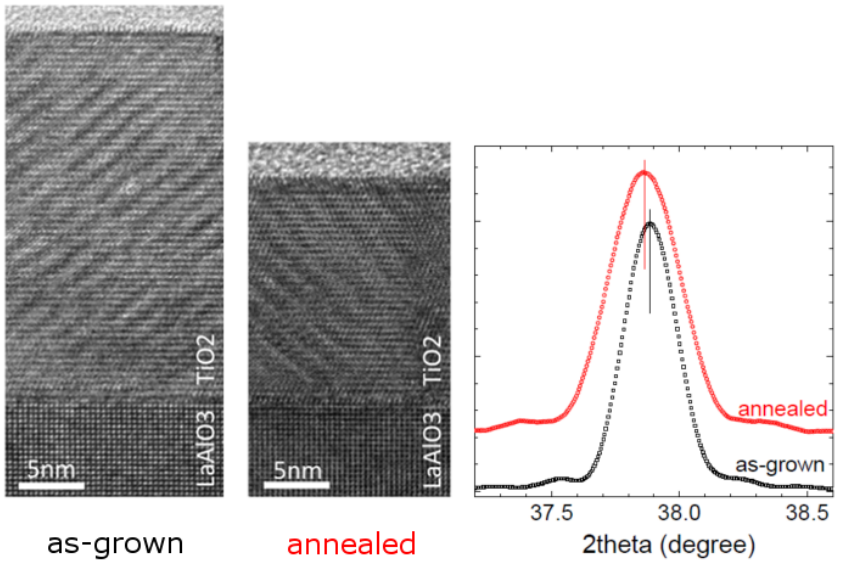

Figure 5.6: *Ex-situ* structural investigation on as-grown (black) and annealed (red) samples: HRTEM images confirm the mild annealing treatment had no impact on the overall crystal structure and preserved the sharp interface with the substrate as well as the surface's flatness. The slight shift of the (004) peak in the XRD pattern indicates a slight expansion of the unit cell due to V_O increment

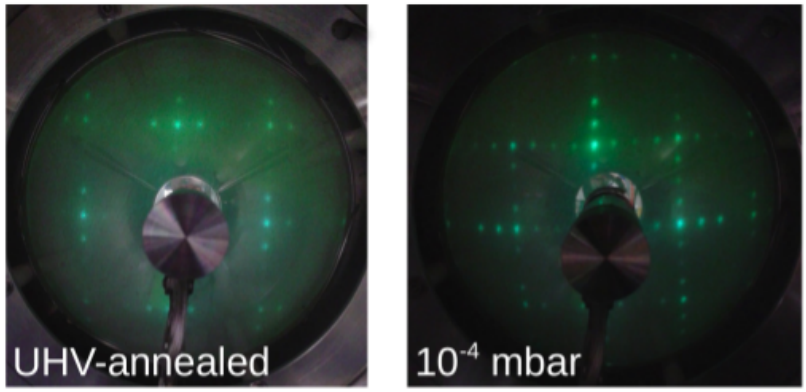

Figure 5.7: LEED patterns of an as-grown sample and an UHV-annealed thin film.

consistent with the Ti^{4+} oxidation state expected for the fully oxygenated TiO_2 [204, 205]. A shoulder around 457 eV reveals the presence of a small amount of Ti atoms in the 3+ valence, typically attributed to oxygen vacancies. The annealing treatment noticeably increases the Ti^{3+} contribution, consistent with the increase of V_O. The XPS data were fitted using pseudo-Voigt functions for all the peaks, after removal of a Shirley background. The $Ti2p_{3/2}$ and $Ti2p_{1/2}$ intensity ratio has been imposed equal to 2, as expected for spin-orbit split core hole statistical populations, for both the detected Ti oxidation states. The Gaussian-Lorentzian fraction has been left as a free parameter in the fitting with the only constrain to be the same for all the components. The Ti^{3+} fraction has been expressed in terms of the total amount of Ti atoms (i.e. the total area Ti_{tot} = Ti^{3+}+Ti^{4+}) and the percentage of reduced Ti atoms increases from 4% up to 11% after the annealing treatment. The X-Ray Absorption spectra confirm the same trend as shown in the bottom panel of Figure 5.8. The Ti2p absorption spectrum Ti^{4+} oxidation state presents four main lines, which are located at approximate excitation energies of 458.3 eV, 460.6 eV, 463.5 eV and 465.5 eV). These features are typical of the 4+ valence state and have been detected both in anatase and rutile structures, as well as in other perovskites (e.g. $SrTiO_3$,$BaTiO_3$) [181, 206–208]. Since early calculations, they have been attribute to the combination of spin-orbit splitting of the initial states (L_3-L_2) and crystal field splitting of the d orbitals in the final state (t_{2g}-e_g)[209]. The additional splitting in the L3-e_g peak ($h\nu$~460 eV) is the fingerprint of the anatase phase, but its nature is not

clearly understood. As a matter of fact, it has been tentatively attributed to a further crystal splitting arising from the distortions of the ideal octahedron around Ti atom [209], although it has been evidenced that only taking into account long-range effects such doublet can be reproduced by theoretical simulations [210]. After the annealing treatment the intensity of the L_3-t_{2g} peak is strongly lowered, while the signal at the pre-edge as well as in the valley ~459 eV is noticeably increased. These changes are consistent with the Ti^{3+} increment, whose absorption spectrum has been simulated [209, 211] and shows two prominent peaks in correspondence of the Ti^{4+} pre-edge and of the valley between L_3-t_{2g} and L_3-e_g tetravalent anatase peaks. Finally, similar results were also experimentally found comparing stoichiometric vs oxygen defected rutile TiO_2 and $SrTiO_3$ crystals [206, 207]. It is noteworthy that the characteristic anatase doublet of the e_g levels is visible for both samples. Overall, these results prove that quick UHV annealing protocol promotes oxygen depletion in the sample, while preserving the anatase crystal structure, thus ARPES investigation have been carried out.

Figure 5.9 compares the energy-momentum dispersion of the 2DEG and the IG states for the as-grown (blue) and the UHV-annealed (red) samples described above. The spectra have been acquired around the Γof the second Brillouin zone (Γ_1), where the signal of this state is generally more intense [151, 177]. In the case of the annealed sample (*top left panel*), two dispersive states are detected centred at Γ_1: a parabolic-like outer band and an inner, quantised sub-band attributed to the surface confinement potential [180, 192]. The bottoms are located at ~180 meV and ~65 meV for the outer and the inner band respectively, while the Fermi momenta (k_F) are found to be at ~0.18 $Å^{-1}$ and ~0.11 $Å^{-1}$. These values correspond to an electron density $n_{2D} = 5 \times 10^{13}\,cm^{-2}$, according to Lüttinger theorem assuming a two-dimensional nature with spin-degenerate bands for the 2DEG [170]. Such a value is well in agreement with results already reported in the literature for transition metal oxide films with high carrier's concentration[177, 192, 212]. Overall, the results are fully consistent with other ARPES studies reported in literature on anatase both single crystals [177, 178] and thin films [180, 192]. In the case of the as-grown sample (*middle left panel*) films the free carriers are reduced of ~25%. The bottom of the 2DEG is shifted upward in binding energy by ~45 meV, consistent with the assumption of electron doped sample due to the increase of V_O . Moreover, the outer parabola k_F is reduced to 0.14 $Å^{-1}$ and the inner parabola is no longer detected. For a direct comparison, the *bottom*

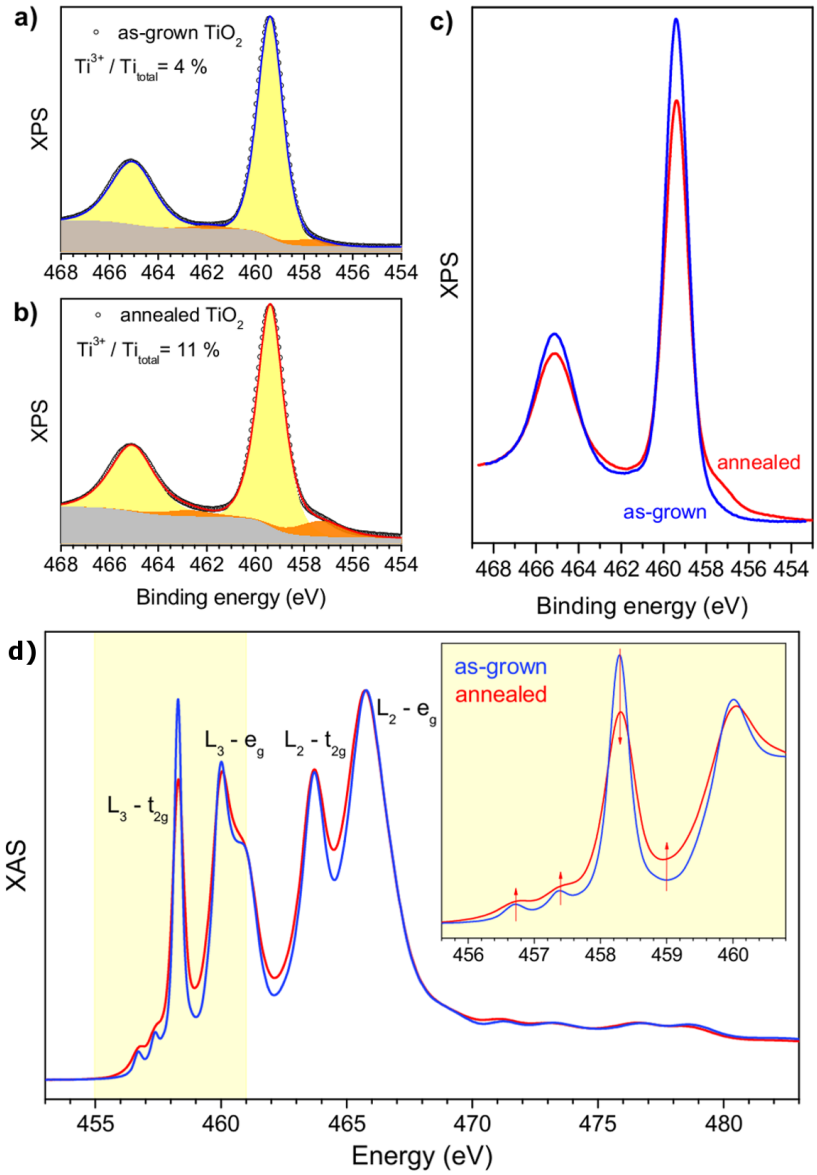

Figure 5.8: *In-situ* spectroscopic investigation of the role of mild annealing. XPS measured at hν= 900 eV(*top panels*) of Ti 2p core levels for (a) as-grown (blue) and (b) annealed samples show an increment of Ti^{3+} concentration (from 4% to 11%) consistent with V_O formation after annealing protocol. (c) reports both XPS spectra for direct comparison. (d) The XAS investigation confirms the trend as the annealed sample (red) show higher contribution in correspondence of Ti^{3+} absorption energies.

left panel reports the momentum distribution curves (MDCs) as extracted at the Fermi level for the two samples. The *right panel* of Figure 5.9 shows the energy distribution curves (EDCs) extracted from the ARPES data at the different k_F momenta of the two thin films. The non-dispersive IG is located at ~1.3 eV binding energies in the as-grown samples, but its spectral weight is shifted towards the Fermi level after the annealing. The IG evolution upon oxygen depletion (arising either from annealing or from beam irradiation effects) has been reported before in the literature of transition metal oxide systems [178, 179, 213]. In particular, the asymmetric shape of the peak is consistent with the presence of a second in-gap state at lower BE (~1 eV). This suggests that the two localised IG states are related either to different types of defects or to different oxygen vacancy sites and that the formation of the shallower defects is favoured by UHV annealing. These results may indicate that the metallic state is strictly related to the formation of oxygen vacancies too, as proposed by Mattioli et al. [182]. In their work, they claim the metallic state is a delocalised impurity level throughout the bulk, which mimics the conduction band. On the other hand, the model by Lazzeri and Selloni, linking the metallic state to the anatase surface reconstruction [190], has provided excellent agreement with experimental data, as recently reported [180]. Moreover, experiments studying the effect of electron doping through alkaline adsorption or the influence of beam irradiation at anatase surface suggest the metallic state is a two-dimensional electron system confined in few nanometres from the surface.[178, 192]

5.2.3. Effects of oxygen dosing

The relation between the oxygen vacancies creation and the evolution of both 2DEG and IG states has been further investigated under conditions where the V_O are compensated in a controlled way. The thin films grown at the APE-NFFA laboratory were transferred to the Soft X-Ray branch of I09 beamline at DIAMOND Light Source (UK) by means of a UHV suitcase, thus preserving the surface from exposure to gases throughout the whole experiment. Molecular oxygen was fluxed during spectra acquisition through a metallic capillary placed at short distance from the sample as schematised in first panel of Figure 5.10. As a matter of fact, adsorbed O_2 on oxides is known to remove the excess electrons from the sample and to transfer them to the molecule [172, 214, 215]. The anatase thin films have been measured without oxygen dosing (base pressure in the

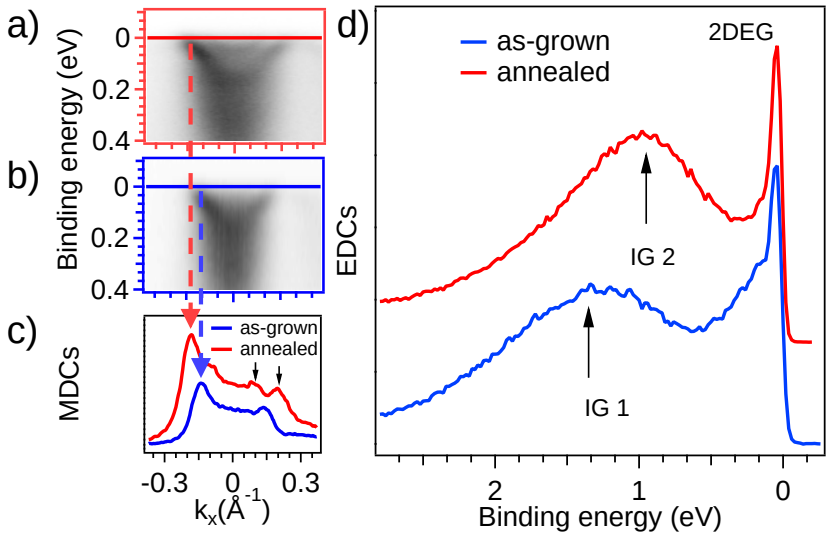

Figure 5.9: ARPES spectra of the 2DEG measured with hν= 46 eV photon energy around the Γof the second Brillouin zone (Γ_1) for two samples with different V_O abundance. (a) Anatase film after the UHV-annealing. (b) Thin film measured as-grown (i.e. with less amount of oxygen vacancies) showing less number of free carriers (the 2DEG state is rigidly shifted upwards of ~135 meV). (c) MDCs extracted at the Fermi level (straight line in panels (a) and (b)) for the annealed (red) and as-grown (blue) samples respectively, the dashed arrows indicate the position of the Fermi momenta k_F, while the black arrows marks the position of the outer and the inner parabola.

experimental chamber 10^{-10} mbar up to a maximum O_2 partial pressure of 4×10^{-9} mbar (monitored by means of a Residual Gas Analyser). Due to the intense photon flux of DIAMOND synchrotron, oxygen depletion under beam irradiation noticeably occurred. However, the general trend of time evolution under beam irradiation observed at I09 beamline agrees reasonably well to those reported in the literature [178, 179], although the complete disappearance of the 2DEG under photon flux was not detected during this experiment. The O_2 was dosed once the intensity of the metallic states stopped increasing and the sample was maintained at 90 K to prevent molecular oxygen icing at the surface.

Figure 5.10 summarises the main effects of O_2 adsorption at the samples' surface and measured with hν= 120 eV linearly horizontal polarised light. *Panel b* reports the integrated DOS across the IG and the 2DEG states for the pristine sample (i.e. at the chamber base pressure) and dosing molecular oxygen. It is readily observable that the intensity of the IGs is strongly suppressed by O_2. In particular, the evolution occurred in few seconds as soon as oxygen is dosed and it was impossible to be time-monitored by means of XPS. Further increase of the oxygen partial pressure only slightly affected the residual IGs intensity, which falls below the background signal as long as O_2 is dosed on the sample and can be detected only at Ti 2p resonance. On the other hand, only minor changes of the 2DEG upon oxygen dosing were detected. The 2DEG intensity is only slightly decreased and the reduction is mainly ascribable to the changes in the background signal. The different response of the IG and 2DEG to O_2 adsorption was not reported before for anatase TiO_2, while similar observations are found for $LaAlO_3/SrTiO_3$ interfaces [213]. Nevertheless, the 2DEG persistence upon oxygen dosing doesn't mean the metallic state is completely uncoupled from the annihilation of the V_O . *Panels (c) - (e)* compare the ARPES spectra measured around Γ_1 for pristine sample (red colour, *panels (c)*) and in the case of the highest molecular oxygen flux used during the experiment (*panels (d), green*). The analyser slit lies in the scattering plane in the I09 geometry, thus symmetry selection rules determine the suppression of the photoemission intensity of the 2DEG centred in the Γ_{10} second BZ. Aside the clear disappearance of the IG spectral intensity (around 1 eV binding energy) the number of free electron carrier in the 2DEG is reduced, as highlighted by the the MDCs at the Fermi level reported in *panels (e)*. The k_F value shrinks from 0.19 $Å^{-1}$ to 0.15 $Å^{-1}$ (i.e. ~20%) when the film is exposed to oxygen, i.e. it shows the opposite trend to that detected after annelaing treatment. This behaviour

is consistent with partial oxygen vacancies healing and the consequent reduction of the n-type carriers at the sample surface is consistent with previous studies [177]. In particular, the free carrier density is reduced of ~60 %, which may suggest that only one electron per V_O is removed from the conduction state.

These findings strongly indicate that the in-gap and the metallic states have a different interplay with the oxygen vacancies inside the material, although they are both linked to the presence of the V_O . In particular, the different response of IG and 2DEG to adsorbed O_2 hints that these two states could be linked to distinct V_O sites. Moreover, since the dosing of molecular oxygen in our setup occurs at the surface, the compensation of the V_O must rely on their capability to migrate inside the material. The very little residual intensity of the IGs suggests that the relative oxygen vacancies are formed either at the surface either at buried sites that can easily move to the surface and recombine with the adsorbed molecules. This has been observed for V_O in anatase (101) and for Ti interstitials at the rutile (110) surface [215, 216]. On the other hand, the here reported 2DEG insensitivity against O_2 exposure, testifies that the migration of the related vacancies to the surface is unlikely, at least in the examined pressure range.

Figure 5.11 and Figure 5.12 report the resonant angular resolved photoemission spectroscopy investigation (RESARPES) performed at the Ti $L_{2,3}$ absorption edges. *Panel a* of Figure 5.11 compares the X-Ray absorption spectra for the pristine and the oxygen-fluxed samples discussed above. The opposite behaviour with respect to the one detected after the annealing treatment (Figure 5.8) is readily observed. The XAS spectra of the O_2 dosed sample shows a strongly reduction in the intensity of the pre-edge as well as in the valleys and at 459 eV and 462 eV, accompanied by a sharpening of the L_3-t_{2g} peak. The observed evolution is consistent with V_O recombination upon adsorbed oxygen molecules' dissociation at the surface and the consequent reduction of Ti^{3+} concentration in the sample just discussed in Figure 5.10. *Panel b* reports the angle-integrated resonant photoemission across the Ti L_3-e_g absorption peak and indicates the IG and 2DEG states resonate at different photon energies. The in-gap spectral intensity is strongly suppressed by oxygen adsorption, nevertheless its resonating behaviour is unaffected as well as its binding energy. In particular, it is peaked in correspondence of the trivalent titanium resonance i.e. its electronic distribution is localised very close to the V_O sites, which is consistent to the flat dispersion reported in ARPES studies and already

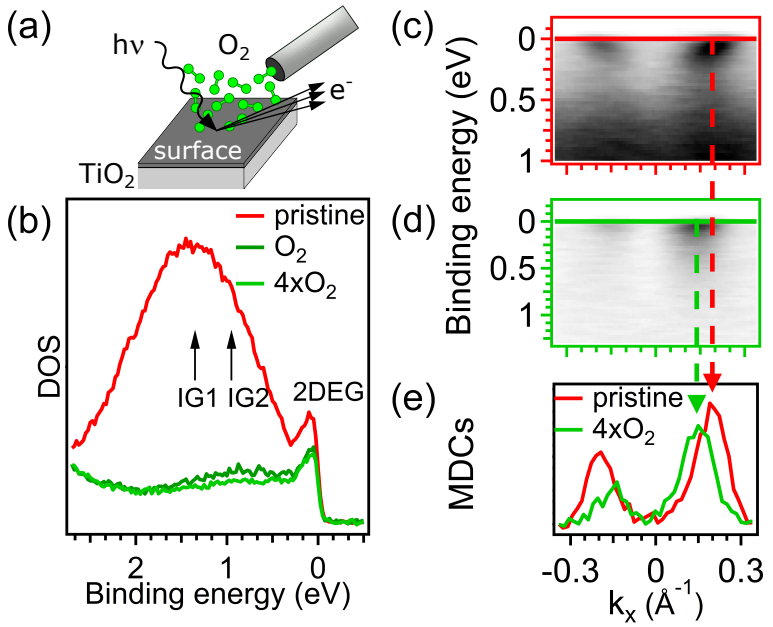

Figure 5.10: (a) Sketch of the experimental setup at I09-2 bemaline. (b) Integrated DOS shows the different response of IGs and 2DEG upon oxygen dosing, with IG spectral intensity strongly quenched by O_2 (c) ARPES at hν= 120 eV aroundΓ_1 of the pristine sample (measured with base pressure 10^{-10} mbar) and (d) with the highest molecular oxygen dose used in the experiment (4×10^{-9} mbar). (e) MDCs extracted at E_F (red and light blue straight lines in panels (a) and (b) respectively) show a significant reduction of the Fermi momenta position, dashed arrows highlight the k_F location. a dramatic reduction of the IG states is observed with only minor changes of the 2DEG.

reported both for anatase and $SrTiO_3$ perovskite [181, 213]. Conversely, the 2DEG follows the same intensity distribution of the XAS signal, being peaked at the L_3-e_g transition. Further proofs of the different nature of these electronic states are provided by the RESARPES data summarised in Figure 5.12. The in-gap state is well visible as flat broad line at lowest

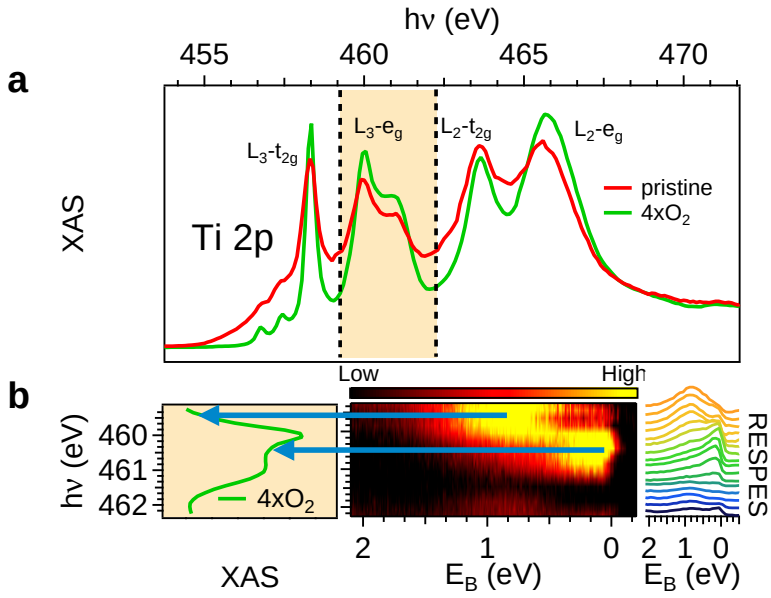

Figure 5.11: (a) XAS of the Ti L_2, L_3 edges of TiO_2 sample, acquired in total yield at 90 K. Red curve refers to the pristine sample measured with chamber base pressure (10^{-10} mbar), while the green curve corresponds to background oxygen pressure $P_{O_2} = 4 \times 10^{-9}$ mbar, i.e. the highest investigated. The shaded area highlights the photon energy range selected for Resonant-ARPES. (b) Resonant-ARPES measured scanning circularly polarised photons across the L_3-e_g absorption energies (*left panel*) in the second BZ of a $TiO_2/LaAlO_3$ sample upon oxygen dosing (4×10^{-9} mbar) to better decouple the IGs and the 2DEG signals. *Central panel* Colour map shows the momentum-integrated photoemitted intensity of the IGs and the 2DEG versus the photon energy. *Right panel* The resonant DOS curves emphasise the different resonating energies for the two shallow states (also highlighted by blue arrows).

photon energies, while the electron pocket located at Γ_{10} appears more clearly at ~460.5 eV. In order to follow quantitatively the trend of both in-gap and EG state as a function of the photon energy, the spectral intensity of both the IG and the 2DEG has been integrated for each photon energy used in the RESARPES scan. Coloured rectangles in the top left graph of *panel a* of Figure 5.12 mark the the binding energy/momentum areas where the integration has been performed (blue/light blue for the 2DEG and red/yellow for the IG). The results have been plotted in *panel b* of Figure 5.12 together with the total yield acquired during the same measurement. As in the case of angle integrated spectra, the 2DEG resonates with the L_3-e_g doublet, whereas the in-gap shows a Ti^{3+} character.

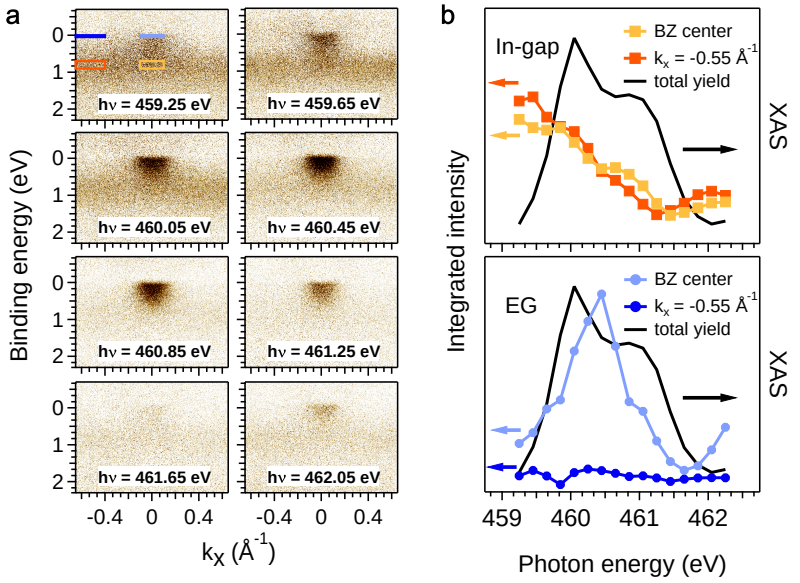

Figure 5.12: (a) selection of ARPES spectra measured in the 2BZ with circular polarised photons across the Ti L_3-e_g absorption edge, $P_{O_2} = 4 \times 10^{-9}$ mbar. The non-dispersive IG state resonates at the lowest photon energy (i.e. at ~458.5 eV) and is visible in the four top frames. Conversely, the 2DEG electron pocket at Fermi in the 2BZ centre (Γ_1) peaks its intensity in the middle of the photon energy scan (459.7eV). (b) Intensities in the investigated photon energy range for the delocalised (*top*) and metallic (*bottom*) states respectively. TEY acquired during the measurement is also shown to highlight the resonant position. Each square (dot) in *top panel* (*bottom panel*) corresponds to ARPES frame measured at different photon energy. The photoemitted intensity has been integrated over E_B-k regions (marked by coloured rectangles in the top-left frame of panel a).

These results confirm the 2DEG electrons is a delocalised over many Ti sites. It is worth to stress such electrons do not have a unique character, being the higher intensity on Ti^{4+} peak caused by the higher abundance of stoichiometric TiO_2 Ti atoms.

At this point it is worth to summarise the main information acquired from the experimental campaign on the anatase TiO_2 thin films.

- The effects of UHV annealing treatment influence both the IG and the 2DEG spectral features, consistently with the n-doping carriers introduced in the system by oxygen vacancies formation. In particular, the results are consistent with the picture of the two excess electron per vacancy being partitioned 1:1 in the IG and the 2DEG

states early proposed and observed in case of $SrTiO_3$ [177, 213].

- On the other hand, the distinct response of the two electronic states upon O_2 strongly suggest that the IG and the 2DEG arise from different vacancy sites and that their capability of re-oxidate is different in the two cases.

- Finally, the resonant-ARPES investigation identified the electronic character of the IG state, which is localised near to the V_O sites.

In order to confirm the hypothesis listed above, a detailed theoretical insight is needed. This has been achieved thanks to a collaboration with Annabella Selloni's group in Princeton University. Slab DFT calculations in the framework of the model described in Ref. [190] have been performed to model the V_O occurring at surface and subsurface sites at the (4x1)-(1x4) reconstructed anatase (001) surface. Several V_O defect sites have been simulated and the respective formation energies are reported in Table 5.1; two sites have appeared to be the most likely to occur at the TiO_2 (001) surface, namely VO1 and VO7. The energy distribution of the excess electrons is very different for the two vacancies. The two electrons are strongly localised on the Ti^{3+} atom near the oxygen vacancy in case of VO1 and corresponds to flat in-gap states (consistent with previous calculations by Shi et al. [217]). On the other hand, delocalised electrons arise for the subsurface VO7 vacancy (as shown also in [218]). Moreover, an attractive potential well (of ~0.2 eV) is formed in the latter case, which confines the excess electron over few (001) planes in the neighbouring of the vacancy. Finally, the adsorption of an O_2 molecule on the anatase surface with a surface or subsurface V_O was considered to model the effect of oxygen dosing. The excess electrons generated by the VO1 defect are both captured by the adsorbed oxygen molecule and no excess electron remains in TiO_2 sample, consistent with the IG intensity quenching observed in ARPES data when the film is exposed to O_2 gas. A quite different situation happens when a subsurface VO7 is considered. In this case, one of the two doping electrons provided by the V_O is transferred to the O_2 adsorbed molecule. The resulting superoxide is characterised by a negative charge which acts as an attractive potential for the remaining subsurface vacancy (positively charged). Nevertheless, the V_O migration to the surface is hindered by a quite high energy barrier which prevents the the vacancy to move perform the VO4-VO3 migration step (see panels (d) and (e) of Figure 5.13), at least for the O_2 concentration probed

Table 5.1: List of the simulated oxygen vacancies occurring at surface/subsurface sites and the respective formation energies

V_O	VO1	VO2	VO3	VO4	VO5	VO6	VO7	VO8
E_{V_O} (eV)	4.17	5.44	5.11	4.14	4.67	3.98	3.79	4.23
V_O	VO9	VO10	VO11					
E_{V_O} (eV)	4.14	3.92	4					

here. This finding differs from the results of the investigation performed on anatase (101) surface previously reported [215]. For the present study the V_O remains subsurface and one of the two excess electrons remains in TiO_2, while the other one is transferred to the oxygen molecule that turns into a superoxide. This is consistent with the observed persistence of the 2DEG state and with the lowered free carrier concentration measured under oxygen dosing.

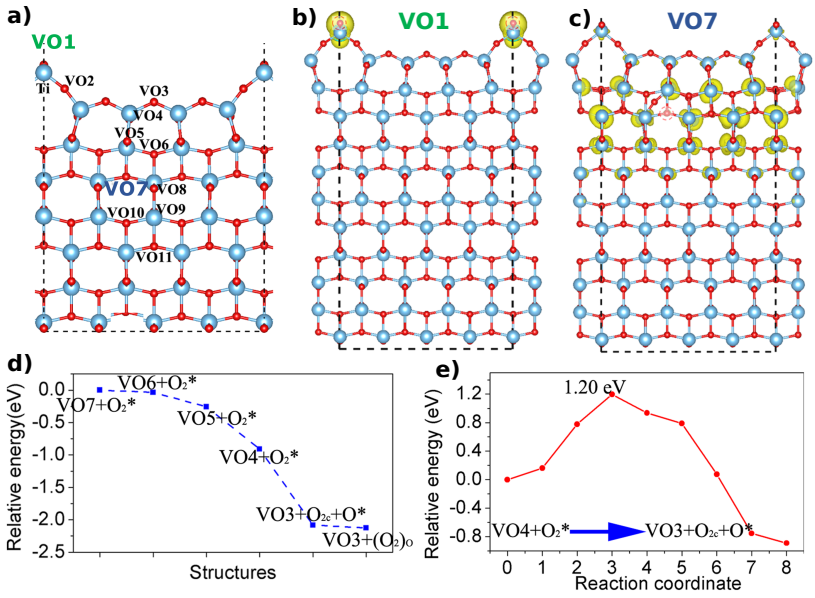

Figure 5.13: *Top panels* Electronic distribution associated to surface and subsurface vacancies. a) Lateral view of the simulated (001) anatase surface showing a (1x4) reconstruction; the sites of all the simulated V_O sites are indicated. b) Electronic distribution (yellow area) associated to VO1 oxygen vacancy, in this case the excess electrons are localised nearby the vacancy site. c) In case of vacancy formed at VO7 site, the electrons are delocalised in subsurface layers parallel to sample surface. *Bottom panels* Effect of O_2 adsorption on a reduced (001)-(1x4) anatase surface. d) Configuration energies for several vacancies in case of adsorbed O_2 at the surface. e) Energy barrier preventing oxygen vacancy migration (and consequent annihilation) from subsurface to surface sites.

5.3. Concluding remarks

In this chapter the evolution of 2DEG and IG states in anatase epitaxial thin film has been investigated. Both *ex-situ* structural characterisation and *in-situ* X-Ray spectroscopies certified the high quality of the PLD grown TiO_2 films and confirmed that mild UHV annealing increase the oxygen vacancies in the samples. ARPES identified delocalised and localised electronic states and provided direct evidence of the n-doping effect induced by the oxygen vacancies. The variations in the spectral shape of the IG are probably related to the formation of more V_O sites characterised by localised electronic distribution, while the enlarged k_F of the 2DEG is consistent with an increased free electron carriers' concentration. RESARPES performed on the Ti 2p absorption edges confirmed the Ti^{3+} character the in-gap state consistent with its localised nature close to the oxygen vacancy site. On the other hand, the 2DEG resonance testified a totally different behaviour of the metallic state, giving evidence of its strong delocalisation over many Ti sites. The most interesting result of the present study was achieved through the investigation of the different response of the IG and 2DEG upon molecular Oxygen dosing at the surface in a wide range of pressures. The delocalised 2DEG is not quenched by the O_2, reporting only a small decrease in the free carriers' concentration. Conversely, the localised IG states switch on-off, suggesting a slightly different depth-dependence of the two electronic states. This result is promising as it might be exploited in applications, e.g. to carefully tailor the charge carriers' concentration in photosensitive devices. However, it may be counterintuitive as the capability to migrate of oxygen vacancies have been reported on other anatase surfaces [215]. Comparison with DFT calculations gave strong evidence of a distinct depth-dependence of the defect states. The 2DEG comes from subsurface V_O s and resides in subsurface layers. In contrast, the localised IG states arise from V_O s at the topmost surface layer. Kinetic studies of the defects diffusion in anatase (001), combined with the different spatial locations, confirmed the 2DEG states are much more robust than the localised in-gap states when exposed to molecular oxygen.

Acknowledgements

This thesis has been performed in the framework of the nanoscience foundry and fine analysis (Progetto Internazionale NFFA MIUR) facility. We acknowledge Prof. A. Selloni for providing the calculation on the reactivity of oxygen vacancies in anatase TiO_2, Dr. T.-L. Lee for support during the experiments at I09 beamline at Diamond and Dr. R.Ciancio for providing the TEM data. We are also grateful to Prof. A. Damascelli, Prof. A. F. Santander-Syro and Prof. K. Sakamoto for carefully read and revise the present manuscript. C. Bigi also wish to thank Dr. P. Orgiani for support in the thin film preparation, Dr. J. Fujii for support during the STM measurements, Dr F. Borgatti and Dr. F. Mazzola for fruitful discussions.

Bibliography

[1] Charles Kittel *et al.*, *Introduction to solid state physics*, Vol. 8 (Wiley New York, 1976).

[2] Neil W Ashcroft and N David Mermin, *Solid state physics* (Cengage Learning, 1976).

[3] Giuseppe Grosso and G Pastori Parravicini, *Solid State Physics (Second edition)* (Elsevier, 2014).

[4] Felix Bloch, "Über die quantenmechanik der elektronen in kristallgittern," Zeitschrift für physik **52**, 555–600 (1929).

[5] John C Slater, "Wave functions in a periodic potential," Physical Review **51**, 846 (1937).

[6] https://trieste.nffa.eu/, "Nffa trieste website," .

[7] Stephan Hüfner, *Photoelectron spectroscopy: principles and applications* (Springer-Verlag, 1995).

[8] Heinrich Hertz, "Ueber einen einfluss des ultravioletten lichtes auf die electrische entladung," Annalen der Physik **267**, 983–1000 (1887).

[9] Albert Einstein, "Über einen die erzeugung und verwandlung des lichtes betreffenden heuristischen gesichtspunkt," Annalen der physik **322**, 132–148 (1905).

[10] Stephan Hüfner, *Very high resolution photoelectron spectroscopy*, Vol. 715 (Springer, 2007).

[11] Ralf Courths and Stefan Hüfner, "Photoemission experiments on copper," Physics Reports **112**, 53–171 (1984).

[12] Andrea Damascelli, Zahid Hussain, and Zhi-Xun Shen, "Angle-resolved photoemission studies of the cuprate superconductors," Reviews of modern physics **75**, 473 (2003).

[13] Andrea Damascelli, "Probing the electronic structure of complex systems by arpes," Physica Scripta **2004**, 61 (2004).

[14] M Pl Seah and WA Dench, "Quantitative electron spectroscopy of surfaces: A standard data base for electron inelastic mean free paths in solids," Surface and interface analysis **1**, 2–11 (1979).

[15] GD Mahan, "Theory of photoemission in simple metals," Physical Review B **2**, 4334 (1970).

[16] Peter J Feibelman and DE Eastman, "Photoemission spectroscopy—correspondence between quantum theory and experimental phenomenology," Physical Review B **10**, 4932 (1974).

[17] J Minár, J Braun, S Mankovsky, and H Ebert, "Calculation of angle-resolved photo emission spectra within the one-step model of photo emission—recent developments," Journal of Electron Spectroscopy and Related Phenomena **184**, 91–99 (2011).

[18] Carl Neil Berglund and William Edward Spicer, "Photoemission studies of copper and silver: theory," Physical Review **136**, A1030 (1964).

[19] Marco Grioni, "Photoelectron spectroscopy," in *Neutron and X-ray Spectroscopy* (Springer, 2006) pp. 189–237.

[20] Eleftherios N Economou, *Green's functions in quantum physics*, Vol. 3 (Springer, 1983).

[21] JB Pendry, "Theory of photoemission," Surface Science **57**, 679–705 (1976).

[22] M Mulazzi, G Rossi, J Braun, J Minár, H Ebert, G Panaccione, I Vobornik, and J Fujii, "Understanding intensities of angle-resolved photoemission with circularly polarized radiation from a cu (111) surface state," Physical Review B **79**, 165421 (2009).

[23] I Vobornik, J Fujii, M Mulazzi, G Panaccione, M Hochstrasser, and G Rossi, "Surface electron bands and fermi surface of be (0001)," Physical Review B **72**, 165424 (2005).

[24] G Panaccione, I Vobornik, J Fujii, D Krizmancic, E Annese, L Giovanelli, F Maccherozzi, F Salvador, A De Luisa, D Benedetti, *et al.*, "Advanced photoelectric effect experiment beamline at elettra: A

surface science laboratory coupled with synchrotron radiation," Review of Scientific Instruments **80**, 043105 (2009).

[25] Shigemi Sasaki, "Analyses for a planar variably-polarizing undulator," Nuclear Instruments and Methods in Physics Research Section A: Accelerators, Spectrometers, Detectors and Associated Equipment **347**, 83–86 (1994).

[26] Shigemi Sasaki, Hideki Kobayashi, Masaru Takao, Yoshikazu Miyahara, and Shinya Hashimoto, "Conceptual design of quasiperiodic undulator," Review of scientific instruments **66**, 1953–1955 (1995).

[27] http://www.trieste.nffa.eu/areas/spectroscopy/arpes-and-spin-arpes/, "Nffa-trieste. angle resolved and spin resolved photoemission spectroscopy with variably polarised light," .

[28] VG Scienta AB, *Instrument Manual - Scienta DA30 analyzer*.

[29] Chiara Bigi, Pranab K Das, Davide Benedetti, Federico Salvador, Damjan Krizmancic, Rudi Sergo, Andrea Martin, Giancarlo Panaccione, Giorgio Rossi, Jun Fujii, *et al.*, "Very efficient spin polarization analysis (vespa): new exchange scattering-based setup for spin-resolved arpes at ape-nffa beamline at elettra," Journal of Synchrotron Radiation **24**, 750–756 (2017).

[30] J. F. Ready, "Effects due to absorption of laser radiation," Journal of Applied Physics **36** (1965).

[31] J George Bednorz and K Alex Müller, "Possible hight c superconductivity in the ba-la-cu-o system," Zeitschrift für Physik B Condensed Matter **64**, 189–193 (1986).

[32] D Dijkkamp, T Venkatesan, XD Wu, SA Shaheen, N Jisrawi, YH Min-Lee, WL McLean, and Mark Croft, "Preparation of y-ba-cu oxide superconductor thin films using pulsed laser evaporation from high t c bulk material," Applied Physics Letters **51**, 619–621 (1987).

[33] Rajiv K Singh and Dhananjay Kumar, "Pulsed laser deposition and characterization of high-tc yba2cu307- x superconducting thin films," Materials Science and Engineering: R: Reports **22**, 113–185 (1998).

[34] D. H. Lowndesand others, "Synthesis of novel thin-film materials by pulsed laser deposition," Science **273** (1996).

[35] P. R. Willmott and J. R. Huber, "Pulsed laser vaporization and deposition," Review of Modern Physics **72** (2000).

[36] P. Orgiani, *Heteroepitaxial nano-engineered structures based on po-*

lifunctional perovskite oxides for the Spintronics., Ph.D. thesis, Universitá di Roma Tor Vergata (2002).

[37] R.K. Singh and J. Narayan, "Pulsed-laser evaporation technique for deposition of thin films: Physics and theoretical model," Physical Review B **41** (1990).

[38] Christof W Schneider and Thomas Lippert, "Laser ablation and thin film deposition," in *Laser Processing of Materials* (Springer, 2010) pp. 89–112.

[39] T. Haguan *et al.*, "Effect of o_2 partial pressure on $yba_2cu_3o_{7-\delta}$ thin film growth by pulsed laser deposition," **397** (2003).

[40] S. Amoruso *et al.*, "Optimization of $la_{0.7}ba_{0.3}mno_{3-\delta}$ complex oxide laser ablation condition by plume imaging and optical emission spectroscopy," **108** (2010).

[41] Tien-Lin Lee and David A Duncan, "A two-color beamline for electron spectroscopies at diamond light source," Synchrotron Radiation News **31**, 16–22 (2018).

[42] https://www.diamond.ac.uk/Instruments/Structures-and-Surfaces/I09/Beamline-layout.html, "I09 beamline webpage," .

[43] Reiner M Dreizler and Eberhard KU Gross, *Density functional theory: an approach to the quantum many-body problem* (Springer Science & Business Media, 2012).

[44] Eberhard Engel and Reiner M Dreizler, *Density functional theory* (Springer, 2013).

[45] Pierre Hohenberg and Walter Kohn, "Inhomogeneous electron gas," Physical review **136**, B864 (1964).

[46] Walter Kohn and Lu Jeu Sham, "Self-consistent equations including exchange and correlation effects," Physical review **140**, A1133 (1965).

[47] Paolo Giannozzi, Stefano Baroni, Nicola Bonini, Matteo Calandra, Roberto Car, Carlo Cavazzoni, Davide Ceresoli, Guido L Chiarotti, Matteo Cococcioni, Ismaila Dabo, *et al.*, "Quantum espresso: a modular and open-source software project for quantum simulations of materials," Journal of physics: Condensed matter **21**, 395502 (2009).

[48] Paul Ziesche, Stefan Kurth, and John P Perdew, "Density functionals from lda to gga," Computational materials science **11**, 122–127 (1998).

[49] John P Perdew, Kieron Burke, and Matthias Ernzerhof, "Generalized gradient approximation made simple," Physical review letters **77**, 3865 (1996).

[50] Kazuyuki Sakamoto, Tae-Hwan Kim, Takuya Kuzumaki, Beate Müller, Yuta Yamamoto, Minoru Ohtaka, Jacek R Osiecki, Koji Miyamoto, Yasuo Takeichi, Ayumi Harasawa, *et al.*, "Valley spin polarization by using the extraordinary rashba effect on silicon," Nature communications **4**, 2073 (2013).

[51] Kazuyuki Sakamoto, Tatsuki Oda, Akio Kimura, Koji Miyamoto, Masahito Tsujikawa, Ayako Imai, Nobuo Ueno, Hirofumi Namatame, Masaki Taniguchi, PEJ Eriksson, *et al.*, "Abrupt rotation of the rashba spin to the direction perpendicular to the surface," Physical review letters **102**, 096805 (2009).

[52] Z-H Zhu, G Levy, B Ludbrook, CN Veenstra, JA Rosen, R Comin, D Wong, P Dosanjh, A Ubaldini, P Syers, *et al.*, "Rashba spin-splitting control at the surface of the topological insulator bi 2 se 3," Physical review letters **107**, 186405 (2011).

[53] Ivana Vobornik, Giancarlo Panaccione, Jun Fujii, Zhi-Huai Zhu, Francesco Offi, Benjamin R Salles, Francesco Borgatti, Piero Torelli, Jean Pascal Rueff, Denis Ceolin, *et al.*, "Observation of distinct bulk and surface chemical environments in a topological insulator under magnetic doping," The Journal of Physical Chemistry C **118**, 12333–12339 (2014).

[54] Haijun Zhang, Chao-Xing Liu, Xiao-Liang Qi, Xi Dai, Zhong Fang, and Shou-Cheng Zhang, "Topological insulators in bi 2 se 3, bi 2 te 3 and sb 2 te 3 with a single dirac cone on the surface," Nature physics **5**, 438 (2009).

[55] Stuart A Wolf, Almadena Yu Chtchelkanova, and Daryl M Treger, "Spintronics—a retrospective and perspective," IBM journal of research and development **50**, 101–110 (2006).

[56] Mark Johnson and Robert H Silsbee, "Interfacial charge-spin coupling: Injection and detection of spin magnetization in metals," Physical Review Letters **55**, 1790 (1985).

[57] NA Cherepkov, "Spin polarisation of photoelectrons ejected from unpolarised atoms," Journal of Physics B: Atomic and Molecular Physics **12**, 1279 (1979).

[58] G Schönhense, "Angular dependence of the polarization of photoelectrons ejected by plane-polarized radiation from argon and xenon

atoms," Physical Review Letters **44**, 640 (1980).

[59] U. Heinzmann, "Spin polarized photoelectrons from atoms and molecules," Applied optics **19**, 4087–4091 (1980).

[60] Cheol-Hwan Park and Steven G Louie, "Spin polarization of photoelectrons from topological insulators," Physical review letters **109**, 097601 (2012).

[61] Z-H Zhu, CN Veenstra, G Levy, A Ubaldini, P Syers, NP Butch, J Paglione, MW Haverkort, IS Elfimov, and A Damascelli, "Layer-by-layer entangled spin-orbital texture of the topological surface state in bi 2 se 3," Physical review letters **110**, 216401 (2013).

[62] Z-H Zhu, CN Veenstra, S Zhdanovich, MP Schneider, T Okuda, K Miyamoto, S-Y Zhu, H Namatame, M Taniguchi, MW Haverkort, *et al.*, "Photoelectron spin-polarization control in the topological insulator bi 2 se 3," Physical review letters **112**, 076802 (2014).

[63] Jonathon Mark Riley, F Mazzola, M Dendzik, M Michiardi, T Takayama, Lewis Bawden, C Granerød, Mats Leandersson, T Balasubramanian, M Hoesch, *et al.*, "Direct observation of spin-polarized bulk bands in an inversion-symmetric semiconductor," Nature Physics **10**, 835 (2014).

[64] Xiuwen Zhang, Qihang Liu, Jun-Wei Luo, Arthur J Freeman, and Alex Zunger, "Hidden spin polarization in inversion-symmetric bulk crystals," Nature Physics **10**, 387 (2014).

[65] B Reihl, M Erbudak, and DM Campbell, "Production of spin-polarized electrons by photoemission from gaas (110)," Physical Review B **19**, 6358 (1979).

[66] Daniel T Pierce, RJ Celotta, G-C Wang, WN Unertl, A Galejs, CE Kuyatt, and SR Mielczarek, "The gaas spin polarized electron source," Review of Scientific Instruments **51**, 478–499 (1980).

[67] Oleg V Yazyev, Joel E Moore, and Steven G Louie, "Spin polarization and transport of surface states in the topological insulators bi 2 se 3 and bi 2 te 3 from first principles," Physical review letters **105**, 266806 (2010).

[68] Gabriel Landolt, Steffen Schreyeck, Sergey V Eremeev, Bartosz Slomski, Stefan Muff, Jürg Osterwalder, Evgueni V Chulkov, Charles Gould, Grzegorz Karczewski, Karl Brunner, *et al.*, "Spin texture of bi 2 se 3 thin films in the quantum tunneling limit," Physical review letters **112**, 057601 (2014).

[69] P Orgiani, C Bigi, P Kumar Das, J Fujii, R Ciancio, B Gobaut,

A Galdi, C Sacco, L Maritato, P Torelli, *et al.*, "Structural and electronic properties of bi2se3 topological insulator thin films grown by pulsed laser deposition," Applied Physics Letters **110**, 171601 (2017).

[70] Chris Jozwiak, Cheol-Hwan Park, Kenneth Gotlieb, Choongyu Hwang, Dung-Hai Lee, Steven G Louie, Jonathan D Denlinger, Costel R Rotundu, Robert J Birgeneau, Zahid Hussain, *et al.*, "Photoelectron spin-flipping and texture manipulation in a topological insulator," Nature Physics **9**, 293 (2013).

[71] Hendrik Bentmann, Henriette Maaß, Eugene E Krasovskii, Thiago RF Peixoto, Christoph Seibel, Mats Leandersson, Thiagarajan Balasubramanian, and Friedrich Reinert, "Strong linear dichroism in spin-polarized photoemission from spin-orbit-coupled surface states," Physical review letters **119**, 106401 (2017).

[72] Elia Razzoli, Thomas Jaouen, M-L Mottas, Baptiste Hildebrand, Gael Monney, Andrea Pisoni, Stefan Muff, Mauro Fanciulli, Nicholas C Plumb, VA Rogalev, *et al.*, "Selective probing of hidden spin-polarized states in inversion-symmetric bulk mos 2," Physical review letters **118**, 086402 (2017).

[73] K Miyamoto, H Wortelen, T Okuda, J Henk, and M Donath, "Circular-polarized-light-induced spin polarization characterized for the dirac-cone surface state at w (110) with c 2v symmetry," Scientific reports **8**, 10440 (2018).

[74] Taichi Okuda and Akio Kimura, "Spin-and angle-resolved photoemission of strongly spin–orbit coupled systems," Journal of the Physical Society of Japan **82**, 021002 (2013).

[75] Elaine A Seddon, "Spin-resolved valence photoemission," Handbook of Spintronics , 1–75 (2014).

[76] Taichi Okuda, "Recent trends in spin-resolved photoelectron spectroscopy," Journal of Physics: Condensed Matter **29**, 483001 (2017).

[77] Giorgio Rossi, Fausto Sirotti, and Giancarlo Panaccione, "Atom specific surface magnetometry with linear magnetic dichroism in directional photoemission," MRS Online Proceedings Library Archive **384** (1995).

[78] Marco Liberati, Giancarlo Panaccione, Fausto Sirotti, Pilar Prieto, and Giorgio Rossi, "Surface magnetometry with photoemission dichroism: Ultrathin epitaxial fe-co bcc alloys on fe (100)," Physical

Review B **59**, 4201 (1999).

[79] Fausto Sirotti, Giancarlo Panaccione, and Giorgio Rossi, "Atom-specific surface magnetometry," Physical Review B **52**, R17063 (1995).

[80] G Panaccione, F Sirotti, and G Rossi, "Lmdad as a surface magnetometry," Journal of electron spectroscopy and related phenomena **76**, 189–194 (1995).

[81] D Venus, "Magnetic circular dichroism in angular distributions of core-level photoelectrons," Physical Review B **48**, 6144 (1993).

[82] YH Wang, D Hsieh, D Pilon, L Fu, DR Gardner, YS Lee, and N Gedik, "Observation of a warped helical spin texture in bi 2 se 3 from circular dichroism angle-resolved photoemission spectroscopy," Physical review letters **107**, 207602 (2011).

[83] Wonsig Jung, Yeongkwan Kim, Beomyoung Kim, Yoonyoung Koh, Chul Kim, Masaharu Matsunami, Shin-ichi Kimura, Masashi Arita, Kenya Shimada, Jung Hoon Han, *et al.*, "Warping effects in the band and angular-momentum structures of the topological insulator bi 2 te 3," Physical Review B **84**, 245435 (2011).

[84] MS Bahramy, PDC King, Alberto De La Torre, J Chang, M Shi, L Patthey, Geetha Balakrishnan, Ph Hofmann, R Arita, N Nagaosa, *et al.*, "Emergent quantum confinement at topological insulator surfaces," Nature communications **3**, 1159 (2012).

[85] Seung Ryong Park, Jinhee Han, Chul Kim, Yoon Young Koh, Changyoung Kim, Hyungjun Lee, Hyoung Joon Choi, Jung Hoon Han, Kyung Dong Lee, Nam Jung Hur, *et al.*, "Chiral orbital-angular momentum in the surface states of Bi_2Se_3," Physical review letters **108**, 046805 (2012).

[86] M Mulazzi, M Hochstrasser, M Corso, I Vobornik, J Fujii, J Osterwalder, J Henk, and G Rossi, "Matrix element effects in angle-resolved valence band photoemission with polarized light from the ni (111) surface," Physical Review B **74**, 035118 (2006).

[87] M Mulazzi, M Hochstasser, J Fujii, I Vobornik, G Rossi, and J Henk, "Magnetization-induced symmetry breaking at the surface of ferromagnetic ni (111)," EPL (Europhysics Letters) **82**, 57001 (2008).

[88] Beomyoung Kim, Choong H Kim, Panjin Kim, Wonsig Jung, Yeongkwan Kim, Yoonyoung Koh, Masashi Arita, Kenya Shimada, Hirofumi Namatame, Masaki Taniguchi, *et al.*, "Spin and orbital angular momentum structure of cu (111) and au (111) surface states,"

Physical Review B **85**, 195402 (2012).

[89] Madhab Neupane, S Basak, N Alidoust, S-Y Xu, Chang Liu, I Belopolski, G Bian, J Xiong, H Ji, S Jia, *et al.*, "Oscillatory surface dichroism of the insulating topological insulator bi 2 te 2 se," Physical Review B **88**, 165129 (2013).

[90] MR Scholz, J Sánchez-Barriga, J Braun, D Marchenko, A Varykhalov, M Lindroos, Yung Jui Wang, Hsin Lin, A Bansil, J Minár, *et al.*, "Reversal of the circular dichroism in angle-resolved photoemission from bi 2 te 3," Physical Review Letters **110**, 216801 (2013).

[91] Franck Vidal, M Eddrief, B Rache Salles, I Vobornik, E Velez-Fort, G Panaccione, and M Marangolo, "Photon energy dependence of circular dichroism in angle-resolved photoemission spectroscopy of bi 2 se 3 dirac states," Physical Review B **88**, 241410 (2013).

[92] A Crepaldi, Federico Cilento, M Zacchigna, M Zonno, JC Johannsen, C Tournier-Colletta, L Moreschini, I Vobornik, F Bondino, E Magnano, *et al.*, "Momentum and photon energy dependence of the circular dichroic photoemission in the bulk rashba semiconductors bite x (x= i, br, cl)," Physical Review B **89**, 125408 (2014).

[93] Lewis Bawden, Jonathan M Riley, Choong H Kim, Raman Sankar, Eric J Monkman, Daniel E Shai, Haofei I Wei, Edward B Lochocki, Justin W Wells, Worawat Meevasana, *et al.*, "Hierarchical spin-orbital polarization of a giant rashba system," Science advances **1**, e1500495 (2015).

[94] J Sánchez-Barriga, A Varykhalov, J Braun, S-Y Xu, N Alidoust, O Kornilov, J Minár, K Hummer, G Springholz, G Bauer, *et al.*, "Photoemission of bi 2 se 3 with circularly polarized light: Probe of spin polarization or means for spin manipulation?" Physical Review X **4**, 011046 (2014).

[95] Nasser Alidoust, Guang Bian, Su-Yang Xu, Raman Sankar, Madhab Neupane, Chang Liu, Ilya Belopolski, Dong-Xia Qu, Jonathan D Denlinger, Fang-Cheng Chou, *et al.*, "Observation of monolayer valence band spin-orbit effect and induced quantum well states in mox 2," Nature communications **5**, 4673 (2014).

[96] Harsh Bana, Elisabetta Travaglia, Luca Bignardi, Paolo Lacovig, Charlotte E Sanders, Maciej Dendzik, Matteo Michiardi, Marco Bianchi, Daniel Lizzit, Francesco Presel, *et al.*, "Epitaxial growth of single-orientation high-quality mos2 monolayers," 2D Materials

5, 035012 (2018).

[97] R Suzuki, M Sakano, YJ Zhang, R Akashi, D Morikawa, A Harasawa, K Yaji, K Kuroda, K Miyamoto, T Okuda, *et al.*, "Valley-dependent spin polarization in bulk mos 2 with broken inversion symmetry," Nature nanotechnology **9**, 611 (2014).

[98] Prasenjit Dey, Luyi Yang, Cedric Robert, Gang Wang, Bernhard Urbaszek, Xavier Marie, and SA Crooker, "Gate-controlled spin-valley locking of resident carriers in wse 2 monolayers," Physical review letters **119**, 137401 (2017).

[99] Hualing Zeng, Junfeng Dai, Wang Yao, Di Xiao, and Xiaodong Cui, "Valley polarization in mos 2 monolayers by optical pumping," Nature nanotechnology **7**, 490 (2012).

[100] Ting Cao, Gang Wang, Wenpeng Han, Huiqi Ye, Chuanrui Zhu, Junren Shi, Qian Niu, Pingheng Tan, Enge Wang, Baoli Liu, *et al.*, "Valley-selective circular dichroism of monolayer molybdenum disulphide," Nature communications **3**, 887 (2012).

[101] Roman Bertoni, Christopher W Nicholson, Lutz Waldecker, Hannes Hübener, Claude Monney, Umberto De Giovannini, Michele Puppin, Moritz Hoesch, Emma Springate, Richard T Chapman, *et al.*, "Generation and evolution of spin-, valley-, and layer-polarized excited carriers in inversion-symmetric wse 2," Physical review letters **117**, 277201 (2016).

[102] Lewis Bawden, SP Cooil, F Mazzola, JM Riley, LJ Collins-McIntyre, V Sunko, KWB Hunvik, Mats Leandersson, CM Polley, T Balasubramanian, *et al.*, "Spin–valley locking in the normal state of a transition-metal dichalcogenide superconductor," Nature communications **7**, 11711 (2016).

[103] Miguel M Ugeda, Aaron J Bradley, Yi Zhang, Seita Onishi, Yi Chen, Wei Ruan, Claudia Ojeda-Aristizabal, Hyejin Ryu, Mark T Edmonds, Hsin-Zon Tsai, *et al.*, "Characterization of collective ground states in single-layer nbse 2," Nature Physics **12**, 92 (2016).

[104] SV Borisenko, AA Kordyuk, VB Zabolotnyy, DS Inosov, D Evtushinsky, B Büchner, AN Yaresko, A Varykhalov, R Follath, W Eberhardt, *et al.*, "Two energy gaps and fermi-surface "arcs" in nbse 2," Physical review letters **102**, 166402 (2009).

[105] R Corcoran, P Meeson, Y Onuki, P-A Probst, M Springford, K Takita, H Harima, GY Guo, and BL Gyorffy, "Quantum oscillations in the mixed state of the type ii superconductor 2h-nbse2,"

Journal of Physics: Condensed Matter **6**, 4479 (1994).

[106] Takayoshi Yokoya, T Kiss, A Chainani, S Shin, Minoru Nohara, and H Takagi, "Fermi surface sheet-dependent superconductivity in 2h-nbse2," Science **294**, 2518–2520 (2001).

[107] hq graphene, "http://www.hqgraphene.com/," .

[108] K Rossnagel, O Seifarth, L Kipp, M Skibowski, D Voß, P Krüger, A Mazur, and J Pollmann, "Fermi surface of 2 h- nbse 2 and its implications on the charge-density-wave mechanism," Physical Review B **64**, 235119 (2001).

[109] LF Mattheiss, "Band structures of transition-metal-dichalcogenide layer compounds," Physical Review B **8**, 3719 (1973).

[110] NJ Doran, DJ Titterington, B Ricco, and G Wexler, "A tight binding fit to the bandstructure of 2h-nbse2 and nbs2," Journal of Physics C: Solid State Physics **11**, 685 (1978).

[111] Hualing Zeng, Gui-Bin Liu, Junfeng Dai, Yajun Yan, Bairen Zhu, Ruicong He, Lu Xie, Shijie Xu, Xianhui Chen, Wang Yao, *et al.*, "Optical signature of symmetry variations and spin-valley coupling in atomically thin tungsten dichalcogenides," Scientific reports **3**, 1608 (2013).

[112] Yves Noat, JA Silva-Guillén, Tristan Cren, V Cherkez, Christophe Brun, Stéphane Pons, François Debontridder, Dimitri Roditchev, William Sacks, Laurent Cario, *et al.*, "Quasiparticle spectra of 2 h- nbse 2: Two-band superconductivity and the role of tunneling selectivity," Physical Review B **92**, 134510 (2015).

[113] Y Ishida, H Kanto, A Kikkawa, Y Taguchi, Y Ito, Y Ota, K Okazaki, W Malaeb, M Mulazzi, M Okawa, *et al.*, "Common origin of the circular-dichroism pattern in angle-resolved photoemission spectroscopy of srtio 3 and cu x bi 2 se 3," Physical review letters **107**, 077601 (2011).

[114] Michael Schüler, Umberto De Giovannini, Hannes Hübener, Angel Rubio, Michael A Sentef, and Philipp Werner, "Local berry curvature signatures in dichroic angle-resolved photoelectron spectroscopy," arXiv preprint arXiv:1905.09404 (2019).

[115] AS Ketterl, Sebastian Otto, M Bastian, Beatrice Andres, Cornelius Gahl, Jan Minár, Hubert Ebert, Jürgen Braun, Oleg Evgenievich Tereshchenko, Konstantin A Kokh, *et al.*, "Origin of spin-polarized photocurrents in the topological surface states of bi 2 se 3," Physical Review B **98**, 155406 (2018).

[116] G Schönhense, C Westphal, J Bansmann, and M Getzlaff, "Circular dichroism in photoemission from nonmagnetic, low-z solids: a conspicuous effect of the photon spin," EPL (Europhysics Letters) **17**, 727 (1992).

[117] C-Z Xu, Y Liu, R Yukawa, L-X Zhang, I Matsuda, T Miller, and T-C Chiang, "Photoemission circular dichroism and spin polarization of the topological surface states in ultrathin bi 2 te 3 films," Physical review letters **115**, 016801 (2015).

[118] Hanyoung Ryu, Inkyung Song, Beomyoung Kim, Soohyun Cho, Shoresh Soltani, Timur Kim, Moritz Hoesch, Choong H Kim, and Changyoung Kim, "Photon energy dependent circular dichroism in angle-resolved photoemission from au (111) surface states," Physical Review B **95**, 115144 (2017).

[119] Ryan P Day, Berend Zwartsenberg, Ilya S Elfimov, and Andrea Damascelli, "Computational framework chinook for angle-resolved photoemission spectroscopy," npj Quantum Materials **4**, 1–10 (2019).

[120] J. Mannhart and D. G. Schlom, "Oxide interfaces—an opportunity for electronics," Science **327**, 1607–1611 (2010).

[121] Harold Y Hwang, Yoh Iwasa, Masashi Kawasaki, Bernhard Keimer, Naoto Nagaosa, and Yoshinori Tokura, "Emergent phenomena at oxide interfaces," Nature materials **11**, 103 (2012).

[122] Xiaoxiang Xu, Chamnan Randorn, Paraskevi Efstathiou, and John TS Irvine, "A red metallic oxide photocatalyst," Nature materials **11**, 595 (2012).

[123] Han-Jin Noh, BJ Kim, SJ Oh, JH Park, HJ Lin, CT Chen, YS Lee, K Yamaura, and E Takayama-Muromachi, "Comparative study of the electronic structures of srmo3 (m= ti, v, mn, fe, and co; m= zr, mo, ru, and rh) by o 1s x-ray absorption spectroscopy," Journal of Physics: Condensed Matter **20**, 485208 (2008).

[124] Loig Vaugier, Hong Jiang, and Silke Biermann, "Hubbard u and hund exchange j in transition metal oxides: Screening versus localization trends from constrained random phase approximation," Physical Review B **86**, 165105 (2012).

[125] JM Longo, PM Raccah, and JB Goodenough, "Magnetic properties of srruo3 and caruo3," Journal of Applied Physics **39**, 1327–1328 (1968).

[126] H Hannerz, Gunnar Svensson, S Ya Istomin, and OG D'yachenko,

"Transmission electron microscopy and neutron powder diffraction studies of gdfeo3 type srnbo3," Journal of Solid State Chemistry **147**, 421–428 (1999).

[127] Yingtao Zhu, Ying Dai, Kangrong Lai, Zhujie Li, and Baibiao Huang, "Optical transition and photocatalytic performance of d1 metallic perovskites," The Journal of Physical Chemistry C **117**, 5593–5598 (2013).

[128] Yong-Qiang Xu, Shao-Yi Wu, Jia-Xing Guo, Li-Na Wu, and Li Peng, "First-principles investigation on the structural, elastic and electronic properties and mechanism on the photocatalytic properties for srnbo3 and sr0. 97nbo3," Journal of Physics and Chemistry of Solids **111**, 403–409 (2017).

[129] Chenghua Sun and Debra J Searles, "Electronics, vacancies, optical properties, and band engineering of red photocatalyst srnbo3: A computational investigation," The Journal of Physical Chemistry C **118**, 11267–11270 (2014).

[130] Daichi Oka, Yasushi Hirose, Shoichiro Nakao, Tomoteru Fukumura, and Tetsuya Hasegawa, "Intrinsic high electrical conductivity of stoichiometric srnb o 3 epitaxial thin films," Physical Review B **92**, 205102 (2015).

[131] Teguh Citra Asmara, Dongyang Wan, Yongliang Zhao, Muhammad Aziz Majidi, Christopher T Nelson, Mary C Scott, Yao Cai, Bixing Yan, Daniel Schmidt, Ming Yang, *et al.*, "Tunable and low-loss correlated plasmons in mott-like insulating oxides," Nature communications **8**, 15271 (2017).

[132] DY Wan, YL Zhao, Y Cai, TC Asmara, Z Huang, JQ Chen, J Hong, Sheng Ming Yin, CT Nelson, MR Motapothula, *et al.*, "Electron transport and visible light absorption in a plasmonic photocatalyst based on strontium niobate," Nature communications **8**, 15070 (2017).

[133] Tao Zhu, Paolo E Trevisanutto, Teguh Citra Asmara, Lei Xu, Yuan Ping Feng, and Andrivo Rusydi, "Generation of multiple plasmons in strontium niobates mediated by local field effects," Physical Review B **98**, 235115 (2018).

[134] Kazuyuki Isawa, Rittaporn Itti, Jun Sugiyama, Naoki Koshizuka, and H Yamauchi, "Photoelectron spectroscopic study of sr x nbo 3," Physical Review B **49**, 3534 (1994).

[135] Tadeusz Miruszewski, Bartosz Kamecki, Marcin Łapiński, and

Jakub Karczewski, "Fabrication, structural and electrical properties of sr (v, nb) o3-δ perovskite materials," Materials Chemistry and Physics **212**, 446–452 (2018).

[136] Christine A Kuntscher, S Schuppler, P Haas, B Gorshunov, M Dressel, M Grioni, Frank Lichtenberg, Alexander Herrnberger, Franz Mayr, and Jochen Mannhart, "Extremely small energy gap in the quasi-one-dimensional conducting chain compound s r n b o 3.41," Physical review letters **89**, 236403 (2002).

[137] Christine A Kuntscher, S Schuppler, P Haas, B Gorshunov, Martin Dressel, M Grioni, and Frank Lichtenberg, "Electronic and vibrational properties of the low-dimensional perovskites sr 1- y la y nb o 3.5- x," Physical Review B **70**, 245123 (2004).

[138] Gerard Tobias and Enric Canadell, "Nature of the bottom t2g-block bands of layered perovskites. implications for the transport properties of phases where these bands are partially filled," Journal of the American Chemical Society **128**, 4318–4329 (2006).

[139] Chunlin Chen, Deqiang Yin, Kazutoshi Inoue, Frank Lichtenberg, Xiuliang Ma, Yuichi Ikuhara, and Johannes Georg Bednorz, "Atomic-scale origin of the quasi-one-dimensional metallic conductivity in strontium niobates with perovskite-related layered structures," ACS nano **11**, 12519–12525 (2017).

[140] J. G. Chen, "Nexafs investigations of transition metal oxides, nitrides, carbides, sulfides and other interstitial compounds," Surface Science Reports **30**, 1–152 (1997).

[141] FMF De Groot, M Grioni, JC Fuggle, J Ghijsen, GA Sawatzky, and H Petersen, "Oxygen 1s x-ray-absorption edges of transition-metal oxides," Physical Review B **40**, 5715 (1989).

[142] Biqiong Wang, Yang Zhao, Mohammad Norouzi Banis, Qian Sun, Keegan R Adair, Ruying Li, Tsun-Kong Sham, and Xueliang Sun, "Atomic layer deposition of lithium niobium oxides as potential solid-state electrolytes for lithium-ion batteries," ACS applied materials & interfaces **10**, 1654–1661 (2018).

[143] P Orgiani, A Yu Petrov, R Ciancio, A Galdi, L Maritato, and BA Davidson, "Evidence of direct correlation between out-of-plane lattice parameter and metal-insulator transition temperature in oxygen-depleted manganite thin films," Applied Physics Letters **100**, 042404 (2012).

[144] David L Windt, "Imd—software for modeling the optical properties

of multilayer films," Computers in physics **12**, 360–370 (1998).

[145] Manuel Sánchez del Río and Roger J Dejus, "Xop v2. 4: recent developments of the x-ray optics software toolkit," in *Advances in Computational Methods for X-Ray Optics II*, Vol. 8141 (International Society for Optics and Photonics, 2011) p. 814115.

[146] Ignacio Horcas, Rs Fernández, JM Gomez-Rodriguez, JWSX Colchero, JWSXM Gómez-Herrero, and AM Baro, "Wsxm: a software for scanning probe microscopy and a tool for nanotechnology," Review of scientific instruments **78**, 013705 (2007).

[147] Paolo Giannozzi, Oliviero Andreussi, Thomas Brumme, Oana Bunau, M Buongiorno Nardelli, Matteo Calandra, Roberto Car, Carlo Cavazzoni, Davide Ceresoli, Matteo Cococcioni, *et al.*, "Advanced capabilities for materials modelling with quantum espresso," Journal of Physics: Condensed Matter **29**, 465901 (2017).

[148] AA. VV., "Quantumespresso pslibrary," https://www.quantum-espresso.org/pseudopotentials.

[149] Hendrik J Monkhorst and James D Pack, "Special points for brillouin-zone integrations," Physical review B **13**, 5188 (1976).

[150] M Takizawa, M Minohara, H Kumigashira, D Toyota, M Oshima, H Wadati, T Yoshida, A Fujimori, M Lippmaa, M Kawasaki, *et al.*, "Coherent and incoherent d band dispersions in srvo 3," Physical Review B **80**, 235104 (2009).

[151] AF Santander-Syro, O Copie, T Kondo, F Fortuna, S Pailhes, R Weht, XG Qiu, F Bertran, A Nicolaou, A Taleb-Ibrahimi, *et al.*, "Two-dimensional electron gas with universal subbands at the surface of srtio 3," Nature **469**, 189 (2011).

[152] S Backes, TC Rödel, F Fortuna, E Frantzeskakis, P Le Fèvre, F Bertran, M Kobayashi, R Yukawa, T Mitsuhashi, M Kitamura, *et al.*, "Hubbard band versus oxygen vacancy states in the correlated electron metal srvo 3," Physical Review B **94**, 241110 (2016).

[153] Chunlin Chen, Shuhui Lv, Zhongchang Wang, Kazuto Akagi, Frank Lichtenberg, Yuichi Ikuhara, and Johannes Georg Bednorz, "Atomic and electronic structure of the srnbo3/srnbo3. 4 interface," Applied Physics Letters **105**, 221602 (2014).

[154] Teppei Yoshida, Kiyohisa Tanaka, Hajime Yagi, Akihiro Ino, Hiroshi Eisaki, Atsushi Fujimori, and Z-X Shen, "Direct observation of the mass renormalization in srvo 3 by angle resolved photoemission spectroscopy," Physical review letters **95**, 146404 (2005).

[155] D. Bach, H. Störmer, R. Schneider, D. Gerthsen, and J. Verbeeck, "Eels investigations of different niobium oxide phases," Microscopy & Microanalysis **12**, 416–423 (2006).

[156] R. Tao, R. Todorovic, J. Liu, R. J. Meyer, A. Arnold, W. Walkosz, P. Zapol, A. Romanenko, L. D. Cooley, and R. F. Klie, "Electron energy-loss spectroscopy study of metallic nb and nb oxides," Journal of Applied Physics **110** (2011).

[157] Takashi Nakamura, Ryo Oike, Yihan Ling, Yusuke Tamenori, and Koji Amezawa, "The determining factor for interstitial oxygen formation in ruddlesden–popper type la 2 nio 4-based oxides," Physical Chemistry Chemical Physics **18**, 1564–1569 (2016).

[158] KB Garg, NL Saini, BR Sekhar, RK Singhal, B Doyle, S Nannarone, F Bondino, E Magnano, E Carleschi, and T Chatterji, "Doped holes and mn valence in manganites: a polarized soft x-ray absorption study of lamno3 and quasi-2d manganite systems," Journal of Physics: Condensed Matter **20**, 055215 (2008).

[159] Daniel Mierwaldt, Stephanie Mildner, Rosa Arrigo, Axel Knop-Gericke, Emanuel Franke, Andreas Blumenstein, Jörg Hoffmann, and Christian Jooss, "In situ xanes/xps investigation of doped manganese perovskite catalysts," Catalysts **4**, 129–145 (2014).

[160] VV Atuchin, IE Kalabin, VG Kesler, and NV Pervukhina, "Nb 3d and o 1s core levels and chemical bonding in niobates," Journal of electron spectroscopy and related phenomena **142**, 129–134 (2005).

[161] MV Kuznetsov, AS Razinkin, and EV Shalaeva, "Photoelectron spectroscopy and diffraction of surface nanoscale nbo/nb (110) structures," Journal of Structural Chemistry **50**, 514–521 (2009).

[162] Sunjic Doniach and M Sunjic, "Many-electron singularity in x-ray photoemission and x-ray line spectra from metals," Journal of Physics C: Solid State Physics **3**, 285 (1970).

[163] PH Citrin, GK Wertheim, and Y Baer, "Many-body processes in x-ray photoemission line shapes from li, na, mg, and al metals," Physical Review B **16**, 4256 (1977).

[164] LPH Jeurgens, WG Sloof, CG Borsboom, FD Tichelaar, and EJ Mittemeijer, "Determination of total primary zero loss intensities in measured electron emission spectra of bare and oxidised metals: Application to aluminium oxide films on aluminium substrates," Applied surface science **161**, 139–148 (2000).

[165] TC Rödel, C Bareille, F Fortuna, C Baumier, F Bertran, P Le Fèvre,

M Gabay, O Hijano Cubelos, MJ Rozenberg, T Maroutian, *et al.*, "Orientational tuning of the fermi sea of confined electrons at the srtio 3 (110) and (111) surfaces," Physical Review Applied **1**, 051002 (2014).

[166] PDC King, S McKeown Walker, Anna Tamai, Alberto De La Torre, T Eknapakul, P Buaphet, S-K Mo, W Meevasana, MS Bahramy, and Félix Baumberger, "Quasiparticle dynamics and spin–orbital texture of the srtio 3 two-dimensional electron gas," Nature communications **5**, 3414 (2014).

[167] H Wadati, T Yoshida, A Chikamatsu, H Kumigashira, M Oshima, H Eisaki, Z-X Shen, T Mizokawa, and A Fujimori, "Angle-resolved photoemission spectroscopy of perovskite-type transition-metal oxides and their analyses using tight-binding band structure," Phase Transitions **79**, 617–635 (2006).

[168] Koji Horiba, Miho Kitamura, Kohei Yoshimatsu, Makoto Minohara, Enju Sakai, Masaki Kobayashi, Atsushi Fujimori, and Hiroshi Kumigashira, "Isotropic kink and quasiparticle excitations in the three-dimensional perovskite manganite la 0.6 sr 0.4 mno 3," Physical review letters **116**, 076401 (2016).

[169] J Krempaskỳ, VN Strocov, L Patthey, PR Willmott, R Herger, M Falub, P Blaha, M Hoesch, V Petrov, MC Richter, *et al.*, "Effects of three-dimensional band structure in angle-and spin-resolved photoemission from half-metallic la 2/ 3 sr 1/ 3 mn o 3," Physical Review B **77**, 165120 (2008).

[170] JM Lüttinger, "Fermi surface and some simple equilibrium properties of a system of interacting fermions," Physical Review **119**, 1153 (1960).

[171] Xiaobo Chen and Samuel S Mao, "Titanium dioxide nanomaterials: synthesis, properties, modifications, and applications," Chemical reviews **107**, 2891–2959 (2007).

[172] Tracy L Thompson and John T Yates, "Surface science studies of the photoactivation of tio2 new photochemical processes," Chemical Reviews **106**, 4428–4453 (2006).

[173] Akira Fujishima, Xintong Zhang, and Donald A Tryk, "Tio2 photocatalysis and related surface phenomena," Surface science reports **63**, 515–582 (2008).

[174] SX Zhang, DC Kundaliya, W Yu, S Dhar, SY Young, LG Salamanca-Riba, SB Ogale, RD Vispute, and T Venkatesan,

"Niobium doped tio 2: Intrinsic transparent metallic anatase versus highly resistive rutile phase," Journal of Applied Physics **102**, 013701 (2007).

[175] Michael A Henderson, "A surface science perspective on tio2 photocatalysis," Surface Science Reports **66**, 185–297 (2011).

[176] Konrad Schwanitz, Ulrich Weiler, Ralf Hunger, Thomas Mayer, and Wolfram Jaegermann, "Synchrotron-induced photoelectron spectroscopy of the dye-sensitized nanocrystalline tio2/electrolyte interface: band gap states and their interaction with dye and solvent molecules," The Journal of Physical Chemistry C **111**, 849–854 (2007).

[177] S Moser, Luca Moreschini, J Jaćimović, OS Barišić, Helmuth Berger, Arnaud Magrez, YJ Chang, KS Kim, A Bostwick, E Rotenberg, *et al.*, "Tunable polaronic conduction in anatase tio 2," Physical review letters **110**, 196403 (2013).

[178] TC Rödel, F Fortuna, F Bertran, M Gabay, MJ Rozenberg, AF Santander-Syro, and P Le Fevre, "Engineering two-dimensional electron gases at the (001) and (101) surfaces of tio 2 anatase using light," Physical Review B **92**, 041106 (2015).

[179] Yoshihiro Aiura, Kenichi Ozawa, Eike F Schwier, Kenya Shimada, and Kazuhiko Mase, "Competition between itineracy and localization of electrons doped into the near-surface region of anatase tio2," The Journal of Physical Chemistry C **122**, 19661–19669 (2018).

[180] Zhiming Wang, Zhicheng Zhong, Siobhan McKeown Walker, Z Ristic, J-Z Ma, Flavio Y Bruno, Sara Riccò, Giorgio Sangiovanni, Gyula Eres, Nicholas C Plumb, *et al.*, "Atomically precise lateral modulation of a two-dimensional electron liquid in anatase tio2 thin films," Nano letters **17**, 2561–2567 (2017).

[181] Benoit Gobaut, Pasquale Orgiani, Alessia Sambri, Emiliano di Gennaro, Carmela Aruta, Francesco Borgatti, Valerio Lollobrigida, Denis Céolin, Jean-Pascal Rueff, Regina Ciancio, *et al.*, "Role of oxygen deposition pressure in the formation of ti defect states in tio2 (001) anatase thin films," ACS applied materials & interfaces **9**, 23099–23106 (2017).

[182] G Mattioli, F Filippone, P Alippi, and A Amore Bonapasta, "Ab initio study of the electronic states induced by oxygen vacancies in rutile and anatase tio 2," Physical Review B **78**, 241201 (2008).

[183] Cristiana Di Valentin, Gianfranco Pacchioni, and Annabella Sell-

oni, "Reduced and n-type doped tio2: nature of ti3+ species," The Journal of Physical Chemistry C **113**, 20543–20552 (2009).

[184] Carla Verdi, Fabio Caruso, and Feliciano Giustino, "Origin of the crossover from polarons to fermi liquids in transition metal oxides," Nature communications **8**, 15769 (2017).

[185] TC Rödel, M Vivek, F Fortuna, P Le Fèvre, F Bertran, R Weht, J Goniakowski, M Gabay, and AF Santander-Syro, "Two-dimensional electron systems in a tio 3 perovskites (a= ca, ba, sr): Control of orbital hybridization and energy order," Physical Review B **96**, 041121 (2017).

[186] Stefan Muff, Nicolas Pilet, Mauro Fanciulli, Andrew P Weber, Christian Wessler, Zoran Ristić, Zhiming Wang, Nicholas C Plumb, Milan Radović, and J Hugo Dil, "Influence of ferroelectric order on the surface electronic structure of batio 3 films studied by photoemission spectroscopy," Physical Review B **98**, 045132 (2018).

[187] C Bareille, F Fortuna, TC Rödel, F Bertran, M Gabay, O Hijano Cubelos, A Taleb-Ibrahimi, P Le Fèvre, M Bibes, A Barthélémy, *et al.*, "Two-dimensional electron gas with six-fold symmetry at the (111) surface of ktao 3," Scientific reports **4**, 3586 (2014).

[188] PDC King, RH He, T Eknapakul, P Buaphet, S-K Mo, Y Kaneko, S Harashima, Y Hikita, MS Bahramy, C Bell, *et al.*, "Subband structure of a two-dimensional electron gas formed at the polar surface of the strong spin-orbit perovskite ktao 3," Physical review letters **108**, 117602 (2012).

[189] Tobias Rödel, *Two-dimensional electron systems in functional oxides studied by photoemission spectroscopy*, Ph.D. thesis, Université Paris-Saclay (2016).

[190] Michele Lazzeri and Annabella Selloni, "Stress-driven reconstruction of an oxide surface: the anatase tio 2 (001)-(1× 4) surface," Physical review letters **87**, 266105 (2001).

[191] Tobias Chris Rödel, Franck Fortuna, Shamashis Sengupta, Emmanouil Frantzeskakis, Patrick Le Fèvre, François Bertran, Bernard Mercey, Sylvia Matzen, Guillaume Agnus, Thomas Maroutian, *et al.*, "Universal fabrication of 2d electron systems in functional oxides," Advanced Materials **28**, 1976–1980 (2016).

[192] R Yukawa, M Minohara, D Shiga, M Kitamura, T Mitsuhashi, M Kobayashi, K Horiba, and H Kumigashira, "Control of two-dimensional electronic states at anatase ti o 2 (001) surface by k

adsorption," Physical Review B **97**, 165428 (2018).

[193] GS Herman, MR Sievers, and Y Gao, "Structure determination of the two-domain (1× 4) anatase tio 2 (001) surface," Physical review letters **84**, 3354 (2000).

[194] K Krupski, AM Sanchez, A Krupski, and CF McConville, "Optimisation of anatase tio2 thin film growth on laalo3 (0 0 1) using pulsed laser deposition," Applied Surface Science **388**, 684–690 (2016).

[195] Maria S Martín González, Myriam H Aguirre, Emilio Morán, Miquel Á Alario-Franco, Virginia Perez-Dieste, José Avila, and Maria C Asensio, "In situ reduction of (100) srtio3," Solid State Sciences **2**, 519–524 (2000).

[196] Tomáš Duchoň, Filip Dvořák, Marie Aulická, Vitalii Stetsovych, Mykhailo Vorokhta, Daniel Mazur, Kateřina Veltruská, Tomáš Skála, Josef Mysliveček, Iva Matolínová, *et al.*, "Ordered phases of reduced ceria as epitaxial films on cu (111)," The Journal of Physical Chemistry C **118**, 357–365 (2013).

[197] H Tang, H Berger, PE Schmid, F Levy, and G Burri, "Photoluminescence in tio2 anatase single crystals," Solid State Communications **87**, 847–850 (1993).

[198] L Kavan, M Grätzel, SE Gilbert, C Klemenz, and HJ Scheel, "Electrochemical and photoelectrochemical investigation of single-crystal anatase," Journal of the American Chemical Society **118**, 6716–6723 (1996).

[199] R Ciancio, E Carlino, G Rossi, C Aruta, U Scotti Di Uccio, A Vittadini, and Annabella Selloni, "Magnéli-like phases in epitaxial anatase tio 2 thin films," Physical Review B **86**, 104110 (2012).

[200] Regina Ciancio, Elvio Carlino, Carmela Aruta, Davide Maccariello, Fabio Miletto Granozio, and Umberto Scotti di Uccio, "Nanostructure of buried interface layers in tio 2 anatase thin films grown on laalo 3 and srtio 3 substrates," Nanoscale **4**, 91–94 (2012).

[201] Regina Ciancio, Andrea Vittadini, Annabella Selloni, Riccardo Arpaia, Carmela Aruta, Fabio Miletto Granozio, Umberto Scotti Di Uccio, Giorgio Rossi, and Elvio Carlino, "Evolution of nanostructures of anatase tio 2 thin films grown on (001) laalo 3," Journal of nanoparticle research **15**, 1735 (2013).

[202] AM De Leon-Guevara, P Berthet, J Berthon, F Millot, A Revcolevschi, A Anane, C Dupas, K Le Dang, JP Renard, and P Veillet, "Influence of controlled oxygen vacancies on the magne-

totransport and magnetostructural phenomena in la {sub 0.85} sr {sub 0.15} mno {sub 3 {minus}{delta}} single crystals," Physical Review, B: Condensed Matter **56** (1997).

[203] M Kanai, H Tanaka, and T Kawai, "Origin of metal-insulator transition temperature enhancement in la 0.8 ba 0.2 mn o 3 thin films as determined by structural analysis," Physical Review B **70**, 125109 (2004).

[204] R Sanjines, H Tang, H Berger, F Gozzo, G Margaritondo, and F Levy, "Electronic structure of anatase tio2 oxide," Journal of Applied Physics **75**, 2945–2951 (1994).

[205] Mark C Biesinger, Leo WM Lau, Andrea R Gerson, and Roger St C Smart, "Resolving surface chemical states in xps analysis of first row transition metals, oxides and hydroxides: Sc, ti, v, cu and zn," Applied surface science **257**, 887–898 (2010).

[206] P Le Fevre, J Danger, Hélène Magnan, D Chandesris, Jacques Jupille, S Bourgeois, M-A Arrio, R Gotter, A Verdini, and A Morgante, "Stoichiometry-related auger lineshapes in titanium oxides: Influence of valence-band profile and of coster-kronig processes," Physical Review B **69**, 155421 (2004).

[207] Chaoyu Chen, José Avila, Emmanouil Frantzeskakis, Anna Levy, and Maria C Asensio, "Observation of a two-dimensional liquid of fröhlich polarons at the bare srtio 3 surface," Nature communications **6**, 8585 (2015).

[208] DH Kim, HJ Lee, G Kim, YS Koo, JH Jung, HJ Shin, J-Y Kim, and J-S Kang, "Interface electronic structures of batio 3@ x nanoparticles (x= γ-fe 2 o 3, fe 3 o 4, α-fe 2 o 3, and fe) investigated by xas and xmcd," Physical Review B **79**, 033402 (2009).

[209] FMF De Groot, MO Figueiredo, MJ Basto, M Abbate, H Petersen, and JC Fuggle, "2p x-ray absorption of titanium in minerals," Physics and Chemistry of Minerals **19**, 140–147 (1992).

[210] Peter Krüger, "Multichannel multiple scattering calculation of l 2, 3-edge spectra of tio 2 and srtio 3: importance of multiplet coupling and band structure," Physical Review B **81**, 125121 (2010).

[211] J-S Lee, YW Xie, HK Sato, C Bell, Y Hikita, HY Hwang, and C-C Kao, "Titanium d xy ferromagnetism at the laalo 3/srtio 3 interface," Nature materials **12**, 703 (2013).

[212] Siobhan McKeown Walker, Flavio Yair Bruno, Zhiming Wang, Alberto De La Torre, Sara Riccó, Anna Tamai, Timur K Kim, Moritz

Hoesch, Ming Shi, Mohammad Saeed Bahramy, *et al.*, "Carrier-density control of the srtio3 (001) surface 2d electron gas studied by arpes," Advanced Materials **27**, 3894–3899 (2015).

[213] J Gabel, M Zapf, P Scheiderer, P Schütz, L Dudy, M Stübinger, C Schlueter, T-L Lee, M Sing, and R Claessen, "Disentangling specific versus generic doping mechanisms in oxide heterointerfaces," Physical Review B **95**, 195109 (2017).

[214] Ulrike Diebold, "The surface science of titanium dioxide," Surface science reports **48**, 53–229 (2003).

[215] Martin Setvín, Ulrich Aschauer, Philipp Scheiber, Ye-Fei Li, Weiyi Hou, Michael Schmid, Annabella Selloni, and Ulrike Diebold, "Reaction of o2 with subsurface oxygen vacancies on tio2 anatase (101)," Science **341**, 988–991 (2013).

[216] Stefan Wendt, Phillip T Sprunger, Estephania Lira, Georg KH Madsen, Zheshen Li, Jonas Ø Hansen, Jesper Matthiesen, Asger Blekinge-Rasmussen, Erik Lægsgaard, Bjørk Hammer, *et al.*, "The role of interstitial sites in the ti3d defect state in the band gap of titania," Science **320**, 1755–1759 (2008).

[217] Yongliang Shi, Huijuan Sun, Manh Cuong Nguyen, Caizhuang Wang, Kaiming Ho, Wissam A Saidi, and Jin Zhao, "Structures of defects on anatase tio 2 (001) surfaces," Nanoscale **9**, 11553–11565 (2017).

[218] Sencer Selcuk and Annabella Selloni, "Facet-dependent trapping and dynamics of excess electrons at anatase tio 2 surfaces and aqueous interfaces," Nature materials **15**, 1107 (2016).

List of publications

1. **C. Bigi**, Z. Tang, G. M. Pierantozzi, P. Orgiani, P. K. Das, J. Fujii, I. Vobornik, T. Pincelli, A. Troglia, T.-L. Lee, R. Ciancio, G. Dražic, A. Verdini, A. Regoutz, P. D. C. King, D. Biswas, G. Rossi, G. Panaccione & A. Selloni *Selective control of localised vs. delocalised carriers in anatase TiO_2 through reaction with O_2*, arXiv preprint
arXiv: 1910.03501.

2. **C. Bigi**, P. Orgiani, J. Slawínska, J. Fujii, J. T. Irvine, S. Picozzi, G. Panaccione, I. Vobornik, G. Rossi, D. Payne, & Francesco Borgatti *Direct insight into the band structure of $SrNbO_3$*, submitted

3. G. Vinai, **C. Bigi**, A. Rajan, D. Watson, F. Mazzola, S. Modesti, S. Barua, M. C. Hatnean, G. Balakrishnan, P. D. C. King, P. Torelli & G Rossi *Proximity-induced ferromagnetism and chemical reactivity in few layers VSe_2 heterostructures* arXiv preprint
arXiv: 1909.01713

4. **C. Bigi**, P. Orgiani, A. Nardi, A. Troglia, J. Fujii, G. Panaccione, I. Vobornik & G Rossi *Robustness of topological states in Bi_2Se_3 thin film grown by Pulsed Laser Deposition on (0 0 1)-oriented $SrTiO_3$ perovskite* Applied Surface Science, 473, 190-193 (2019)
Doi: 10.1016/j.apsusc.2018.12.119

5. N. K. Lewis, Y. Lassailly, L. Martinelli, I. Vobornik, J. Fujii, **C. Bigi**, E. Brunkow, N. B. Clayburn, T. J. Gay, W. R. Flavell & E. A. Seddon*Spin-and angle-resolved photoemission studies of the electronic structure of Si (110)"16x2" surfaces*, Physical Reviev B 100, 075302 (2019).
Doi: 10.1103/PhysRevB.100.075302.

6. P. K. Das, D. Di Sante, F. Cilento, **C. Bigi**, D. Kopic, D. Soranzio, A. Sterzi, J. A. Krieger, I. Vobornik, J. Fujii, T. Okuda, V. N. Strocov, M. B. H. Breese, F. Parmigiani, G. Rossi, S. Picozzi, R. Thomale, G. Sangiovanni, R. J. Cava & G. Panaccione *Electronic properties of candidate type-II Weyl semimetal WTe_2. A review perspective*, Electronic Structure, 1, 1, 014003 (2019). Doi: 10.1088/2516-1075/ab0835.

7. **C. Bigi**, P. K. Das, D. Benedetti, F. Salvador, D. Krizmancic, R. Sergo, A. Martin, G. Panaccione, G. Rossi, J. Fujii & I. Vobornik *Very efficient spin polarization analysis (VESPA): new exchange scattering-based setup for spin-resolved ARPES at APE-NFFA beamline at Elettra*, Journal of Synchrotron Radiation, 24, 4, 750-756 (2017).
Doi: 10.1107/S1600577517006907.

8. B. Gobaut, P. Orgiani, A. Sambri, E. di Gennaro, C. Aruta, F. Borgatti, V. Lollobrigida, D. Céolin, J.-P. Rueff, R. Ciancio, **C. Bigi**, P. K. Das, J. Fujii, D. Krizmancic, P. Torelli, I. Vobornik, G. Rossi, F. M. Granozio, U. Scotti di Uccio & G. Panaccione *Role of Oxygen Deposition Pressure in the Formation of Ti Defect States in TiO_2(001) Anatase Thin Films*, ACS applied materials & interfaces, 9, 27, 23099-23106 (2017).
Doi: 10.1021/acsami.7b03181.

9. P. Orgiani, **C. Bigi**, P. K. Das, J. Fujii, R. Ciancio, B. Gobaut, A. Galdi, C. Sacco, L. Maritato, P. Torelli, G. Panaccione, I. Vobornik & G. Rossi *Structural and electronic properties of Bi2Se3 topological insulator thin films grown by pulsed laser deposition*, Applied Physics Letters, 110, 17, 171601 (2017).
Doi: 10.1063/1.4982207.

10. D. Di Sante, P. K. Das, **C. Bigi**, Z. Ergönenc, N. Gürtler, J. A. Krieger, T. Schmitt, M. N. Ali, G. Rossi, R. Thomale, C. Franchini,

S. Picozzi, J. Fujii, V. N. Strocov, G. Sangiovanni, I. Vobornik, R. J. Cava & G. Panaccione *Three-Dimensional Electronic Structure of the Type-II Weyl Semimetal WTe_2*, Physical Review Letters, 119, 2, 026403 (2017).
Doi: 10.1103/PhysRevLett.119.026403.

Ringraziamenti

> For the Quest is achieved, and now all is over. I am glad you are here with me. Here at the end of all things.
>
> John Ronald Reuel Tolkien - The Lord of The Rings

Bene, eccoci qua alla conclusione di un'esperienza impegnativa e magnifica iniziata in un giorno di giugno di ben quattro anni fa grazie a una proposta di tesi magistrale. Guardandomi indietro provo un immenso senso di gratitudine. Non solo per la possibilità di cimentarmi in tanti progetti scientifici di altissimo livello e di corroborare la mia passione per la ricerca, ma anche per il "lato umano" che ho incontrato a Trieste. Le persone conosciute, le nuove amicizie nate (dentro e fuori l'ambito scientifico) sono state per me occasione di crescita professionale e personale insieme.

Innanzitutto, devo e voglio sinceramente ringraziare il Prof. Giorgio Rossi, perché senza la sua proposta questa avventura non sarebbe mai incominciata. Grazie Giorgio per come mi hai seguito in tutti questi anni, per tutto il tempo che hai sempre trovato per discutere dei progetti e per ascoltare le mie domande. Sono molto grata di tutto il supporto che mi hai

sempre offerto, per la prontezza con cui hai corretto queste pagine, persino negli orari improponibili che il tour-de-force finale ha imposto. Il tuo entusiasmo e tensione a capire e imparare da ogni singolo spettro io ti abbia mostrato, anche davanti a quello più scarno e deludente, mi ha trasmesso una serietà e un gusto verso questo lavoro che spero di portare sempre nel mio bagaglio personale. Non avrò mai abbastanza parole per ringraziare Ivana. Grazie per come mi hai accompagnato e guidato in questi miei "primi passi" nel mondo scientifico. Grazie per il tuo "sguardo da Marte" con cui mi hai spesso scosso e rialzato di fronte alle difficoltà, ma anche per come mi hai sempre spronato a implicarmi al massimo con le quotidiane sfide della vita di una beamline, dall'analisi dati ai bake-out. Sono grata per il profondo affetto e stima reciproca nati in questi anni, dentro ai quali si è sviluppato un clima di lavoro ordinato, sereno e informale. Mi mancheranno le nostre discussioni davanti a una tazza di cioccolata calda (...e Jane Fonda ovviamente)! Grazie Jun! La tua immensa gentilezza è eguagliata soltanto dalla tua profondissima conoscenza. Grazie per tutte le volte in cui con pazienza hai ascoltato e risposto alle mie domande, fornendomi sempre aiuto prezioso. Grazie per la tua battuta tagliente, sempre capace di strapparmi una sonora risata anche dopo il beamtime più massacrante. Pasquale, che dire? Grazie per la disponibilità che ti contraddistingue! Non hai mai mancato di darmi consiglio o di condividere la tua immensa conoscenza sugli ossidi, il tutto condito da chicche di saggezza napoletana. Grazie per avermi mostrato che la curiosità è la prima e più efficace arma in mano a uno scienziato. A Giancarlo va il mio grazie, in particolare per le telefonate motivazionali durante i beamtime della morte (soprattutto quelle durante i weekend per sincerarti che fossi ancora viva!). Grazie per tutte le cene al Tiglio e per come mi hai spesso spronato a non arrendermi alla prima difficoltà. Thank you Debashis for the tea and the spinning walks, flavoured with the perfect amount of humour and thanks Sandeep for your patience in waiting for our last-minute lunches at the canteen. A Federico va il mio grazie per la condivisione delle sfide quotidiane della vita da dottorandi. Thank you, Vincent, for being my personal "you should be writing" reminder. Grazie agli sprinters per aver condiviso pranzi lampo in Basovizza durante i beamtime domenicali. Grazie a Gian per aver educato una lombarda al corretto uso di "sticazzi/mecojoni" e grazie Alessandro per avermi mostrato quanto importante può essere un martello. Grazie Ric per le serate a teatro, De Andrè e per le chiacchierate mai banali. Grazie a Giovanni, Sasha, Luca e a tutta l'APE gang per essere sempre stata pronta a offrire parimenti

esperienza, supporto e amicizia. Un grazie speciale a Federico Salvador (nomen omen) per il soccorso sempre pronto, la tua vasta conoscenza e la passione nell'illustrarmi i segreti delle camere e delle migliori Osmize. Le riparazioni dei danni in tua compagnia si sono sempre trasformate in occasioni preziose per me di imparare cose nuove, con la fatica del lavoro intenso sempre alleggerita da "ciacole" di primo ordine. Grazie Tom che anche da Berlino hai sempre trovato il tempo per darmi preziosi consigli, dalla scienza alle scelte per il futuro. Grazie alla mia post-doc per corrispondenza Giulia, grazie per un'amicizia nata da un paio di sorrisi cercati e scambiati davanti alle macchinette del sincro e approfonditasi sempre di più...al punto da arrivare a condividere preziose riserve di cioccolato! Marco, grazie per l'amico sincero che ti sei rivelato... dopo un inizio mooolto traumatico! Fede, sei tra le persone con il più alto tasso di parole al secondo che conosco! Grazie per le innumerevoli chiacchierate di fisica da cui ho sempre imparato qualcosa di nuovo e per la tua amicizia schietta e verace, con la giusta dose di romanaccio, nonché per le dimostrazioni di Lindy Hop.

Ci sono poi gli incontri e le amicizie della quotidianità della vita a Trieste, che negli anni si è fatta sempre più ricca. Con voi Trieste si è trasformata nella mia casa. Un grande grazie è per Virgi, compagna di appartamento e di studi storica. Grazie per la tua prorompente energia e per le cene che hai organizzato in appartamento. Grazie alla tua santa (e inopportuna) intraprendenza ho conosciuto tante splendide persone: Paolet, Welli e Livia, Benedetta, Denny, la crew dei Severi...guardandomi indietro non trovo uno solo di questi incontri che non mi abbia arricchito. Grazie Virgi F., altra coinquilina di lungo corso. Non avrei immaginato due temperamenti più diversi dei nostri...eppure la voglia di condividere le fatiche, le gioie e le sfide delle rispettive strade (con il loro carico di grandi decisioni per il futuro) ha caratterizzato il tempo trascorso insieme e per questo ti ringrazio. Grazie Domenico per la tua semplicità e per la gratuità con cui ti sei affezionato a questa fisica pazza di "Arnate di Gallarate". A Marco e Francesca e alle splendide Aleksandra e Eleonora: grazie per questa amicizia sbocciata inaspettatamente e già così importante per me. Grazie Maria per l'opera pomeridiana, per i vocalizzi imbarazzanti e le proposte ardite con cui mi hai sempre spinto oltre i miei limiti canori. Le prove di canto con te sono state le più divertenti e stimolanti che abbia mai fatto. Grazie a Giulia, all'appa Ginnastica, Marina e Andrea, Franci e Ago, Albi e Giulia con Agnesina e il piccolo Nicolò. Grazie agli amici del pacco, in particolare a Mattia e Carlo per le chiacchierate con in mano

un buon bicèrin d'amaro, a tutti gli amici del coro e alle suorine. Grazie Stefano, Angela e Seba per la gratuità con cui ogni volta mi accogliete.

Grazie Don Andrea, fraterno amico, guida paziente e sempre disponibile nei sempre più risicati ritagli di tempo in Lombardia. La certezza della tua amicizia è una roccia importante per la mia vita. Grazie Richi per l'amicizia schietta e talvolta ruvida, che spesso ci ha portati allo scontro e alla polemica, ma sempre profondamente leale e ricca di stima reciproca e che adesso chiede di assumere una nuova forma. Ti auguro ogni bene per la tua nuova strada, il cui pensiero mi è stato di grande compagnia in questi ultimi mesi. Grazie a Giossi, Gloria, Emma, Frabbo & Coto, Emer & Sissi (con i vostri splendidi bimbi-tornado) per l'amicizia che resiste alla distanza e ai mille impegni che la vita sta riservando a ciascuno. Grazie Emi per le chiacchierate di fisica immancabili davanti a birre e gelati e grazie Greta perché ogni volta ci sopporti paziente!

Grazie alla mia famiglia tutta, in particolare ai miei genitori per come mi avete accompagnato in questi anni e per il sostegno che mi avete sempre offerto con affetto infinito e ognuno a vostro modo. Mamma con i tuoi messaggi intrisi di satira brianzola e papà per tutte le volte che: "Ma l'hai sentita? E il lavoro come va?", che mi danno la certezza di essere sempre nei vostri pensieri. Grazie ai miei fratelli Andrea ed Anna. Ad Anna per i consigli culinari e le ricette di biscotti, sempre apprezzati alle pause caffè. Ad Andrea per le passioni da nerd, le serate al cinema e le chiacchierate su dove ci porterà il futuro nei rispettivi campi.

Potrei riempire un volume di pagine pari a una seconda tesi, ma tranquilli non lo farò. Vorrei solo aggiungere che è incredibile (al limite del miracoloso) constatare quante amicizie inaspettate mi son state donate, la maggior parte delle quali con persone la cui esistenza mi era ignota fino a una manciata di anni fa. E se questo renderà molto più difficile l'arrivederci ad APE e a Trieste, dall'altro lato mi regala anche la grande speranza che la Grazia che mi ha raggiunto qui mi accompagnerà dovunque io vada. Sono consapevole che questo è un elenco paurosamente incompleto e me ne scuso. Non arrabbiatevi troppo per questa mia mancanza perché, parafrasando il Manzoni, "credete che non s'è fatto apposta".